Instituto Tecnológico y de Estudios Superiores de Monterrey

Campus Monterrey

School of Engineering and Sciences

Experimental and computational study of GelMA microgel generation and deformation using a microfluidic device

A thesis presented by

Zahra Taravatfard

Submitted to the
School of Engineering and Sciences
in partial fulfillment of the requirements for the degree of

Master of Science

In

Nanotechnology

Monterrey Nuevo León, December 1st, 2020

Acknowledgements

I would like to express my deepest gratitude to my thesis advisors and committee members, Dr. Sergio Omar Martínez Chapa, Dr. Masoud Madadelahi and Dr. Mallar Ray. I could not imagine better advisors, it was a privilege working under their guidance, their supports, trust and advice was always present throughout my studies. Moreover I am grateful of meeting and collaborating with excellent faculty members, researchers and friends, whose lessons and example helped me experience a rich professional growth and become a better person:

M.Sc.Eng. Fernando Delgado Licona, Dr. Saeed Beigiboroujeni, M.Sc.Eng. Chinmay P. Tiwary, Dr. Zeinab Jafari, Dr. MohammadMahdi Aeinehvand, Dr. Samira Hosseini, M.Sc.Eng Fahimeh Nezhad Moghaddam, BEE. Niousha Musavi, BEE. Amir Hosseini, M.Sc.Eng. Valeria Martinez Villarreal.

Without financial support of Tecnologico de Monterrey and CONACYT this work would have never been possible. I acknowledge the financial support for consumables provided by the Federico Baur Endowed Chair in Nanotechnology.

Finally I would to give my biggest thanks to my wonderful family. My dear parents, Mohsen Taravatfard, and Shahnaz Ghavidel Rostami, and my dear brother, Aria Taravatfard for their unconditional support.

Experimental and computational study of GelMA microgel generation and deformation using a microfluidic device

By
Zahra Taravatfard

Abstract

Gene editing is a technique through which DNA segments can be modified within the genome of a living organism. Despite the many potential applications, current gene editing techniques are still low-throughput and have several limitations. On one side, the conventional 2D cell culturing techniques suffer from low cell viability and proliferation. On the other side, transfection techniques commonly using exogenous materials lead to off-target effects in cells. Droplet-based microfluidic devices (DBMD) show great potential for gene editing. They allow precise single-cell manipulation, encapsulation and might eventually achieve high throughput. As an example, using a DBMD, cells encapsulated in GelMA microgels have kept viability and shown proliferation. Moreover, DBMD might play a key role in cell transfection. Particularly, mechanical squeeze of cells encapsulated in droplets and moving through a narrow channel favors the entrance of foreign materials into the cells.

This thesis presents the design and implementation of droplet-based microfluidic systems for fabrication of monodisperse GelMA microgels. First, a DBMD was developed using three techniques of soft lithography, stereolithography, and cutter plotting and the comparison between the devices was conducted. Second, fabrication of both, solid-like as well as core-shell microgels with average size of 133.43±5 µm was demonstrated. It was shown the generated microgels have spherical morphology with pore size area of 23.28±6 um^2. Finally, computer simulation was used to emulate microgel indentation (solid-like and core-shell) with or without cells; as well as the throughput of the designed confinement channel. From the indentation of particles, it was concluded that lower stiffnesses was obtained for core-shells in comparison to solid-like microgels. It is also shown that a 21% and 24 % deformation in microgels containing cells causes 30% and 40% deformation of encapsulated cells, respectively, vital in cells transfection-based confinement channel application. From computational fluid dynamics (CFD) model, we observed the enhancement of the throughput of the device by selecting a longer confinement length. It is expected these preliminary results presented in this thesis will motivate other works that eventually lead to the development of efficient droplet-based microfluidic devices for cell transfection.

Contents

List of Figures

List of Tables

Chapter 1 Introduction

1.1 Genome Modification and Cell Transfection

Genome modification is a technique through which genes can be modified, deleted, or added within a cell, typically to alleviate medical conditions which arise because of cellular disfunctions [1]. Similarly, cell transfection is defined as a procedure of artificially introducing genetic material/nucleic acids into cells for genome modification [2]. The main parameters in cell transfection and genome modification are delivery efficiency, cell functionality [3]. Delivery efficiency is defined as successful delivery of genome vectors in targeted cells, cell transfection is a successful delivery of foreign nucleic acids into cells [2], and finally, maintenance of cellular functionality is related to attempts in minimizing the mutations caused by introducing foreign materials into cells. Enhancing cell transfection and delivery efficiency next to alleviating the probable cells' mutations have recently attracted a lot of research attention [4-6].

Genome modification and cell transfection are challenges in research and therapeutic applications. There are different delivery systems defined for genome editing including, viral vectors [7, 8], mechanical methods (electrophoresis, microinjection, mechanical deformation) [9, 10], and chemical methods [11]. Current physical and vector-based methods are hindered by their low-throughput, low functionality in colony formation, and their reliance on exogenous materials and electrical fields [10]. These drawbacks lead to perturbation in cell functionality caused by toxicity and off-target effects [12, 13]. The eventual increase in automation and throughput of current genome editing/cell transfection systems will allow transfection of millions of cells in a fast and efficient way, and make this technology offer solutions to today's therapeutic challenges [6].

1.2 Droplet-Based Microfluidic System

Microfluidics has emerged in the early 1980s as a promising technology that combines different areas of chemistry, biology, and material science [14]. Microfluidic devices allow the control of small volumes of fluids to enable biological assays with enhancement of the automation.

A droplet-based microfluidic system is a sub-category of microfluidic systems that enables miniaturization of biological experiments by carrying out manipulations at the single-cell level [15]. These devices are dispersed multi-phase systems, which often consist of a continuous carrier phase and a dispersed sample phase to generate monodisperse water in oil (w/o) microdroplets. Each microdroplet acts as an ultra-small assay volume (from a few picolitres to nanoliters) that can be generated at high rates [16]. The size and generation speed of droplets are adjustable and can be easily controlled through the size of the microchannels or the fluid flow rates [17]. The functionality of droplet-based microfluidic systems varies from basic concepts of mixing, merging and splitting of droplets [18] to more complex concepts of encapsulation [19] and sorting [20]. Droplet-based microfluidic systems have been widely used for many applications such as imaging drug delivery [21], tissue engineering [22], chemical reactions [23], and particle synthesis [24]. However, the most significant application has been explored in single-cell manipulation and analysis, and most recently in genome editing and cell transfection platforms[15].

1.3 Cell Transfection by Single-cell Mechanical Deformation Using Microfluidic Systems

One of the potential applications of microfluidic systems is cells transfection based on confinement channels. This method reduces the drawbacks of viral vectors, like off-target effects and low-throughput as it mechanically penetrates cells by deforming them. These systems work based on the temporary disruption of cells membrane through several confinement channels or posts with different geometries. In detail, cell deformation causes the formation of transient holes in cells membrane that makes possible the delivery of foreign materials into cells [25]. This feature leads to higher cell functionality compared to other delivery methods. Using these techniques researchers have been able to successfully deliver DNA, RNAs, carbon nanotubes, proteins [26]. A microfluidic-based confinement channel benefits from the high controllability, good monodispersity [27], and higher throughput [28]. The performance of cell transfection based microfluidic penetration is directly related to delivery efficiency, colony formation, and cell response to the applied force. These factors are also dependent on cell speed, microfluidic channel geometry, and dimensions [29].

Additional work still is needed in, (i) fabrication of low-cost microfluidic chips with varying channels' heights. The current fabricated microfluidic chips for this application are based on soft lithography which is a time consuming and an expensive technique, (ii) formulating and better understanding the effect of parameters, including microfluidic channel geometry, cell deformation, and cell speed, on delivery efficiency and cell functionality. Due to our knowledge in the current design of the fabrication of microfluid-based constriction chip, the common concerning parameters for cell transfection are confinement channel's dimension and flow velocity. In the previous studies in the literature, these parameters are usually optimized experimentally and not computationally, and (iii) development of a high-throughput technique for cells transfection application. The additional use of on-chip chemical and physical techniques for accelerating cells colony formation remains a topic that requires more exploration. In cell modification purposes through introducing genetic materials into cells, usually hundreds to thousands of genetic materials are needed to be delivered. On-chip colony formation gives rise to the fabrication of a high-throughput device that can generate a large number of colonies of transfected cells rather than hundreds of transfected single cells. Formation of a colony of transfected cells is an important part of the functionality of microfluidic-based transfection devices [30].

1.4 Thesis Overview

This thesis has demonstrated the design and fabrication of a droplet-based microfluidic device for solid-like and core-shell GelMA microgels generation. Three techniques of soft lithography, stereolithography, and cutter plotting were used for fabrication of a DBMD, and the compression between the fabricated chips was done. GelMA was synthesized as the base material of microgels due to its wide applications in cell culturing and fast crosslinking that is caused by UV photosensitivity. Using the fabricated chip and GelMA pre-polymer, solid-like and core-shell microgels were generated. The size adjustability of microgels were controlled using GelMA flow rate. Bigger size GelMA microgels were generated using a higher GelMA flow rate. The size distribution of the generated particles was also extracted and depicted the success of the low-cost fabricated microfluidic system in the generation of monodispersed micron sized GelMA microgels. Characterization of the fabricated microgels by FTIR (Fourier Transform Infrared Spectroscopy) and SEM (Scanning Electron Microscope) was also conducted to evaluate the

synthesized GelMA composition and crosslinking, porosity, and morphology. Finite element analysis (FEM) was used to emulate the indentation of the microgels and their movement in a constrained channel. Targeted specimens in the indentation model include microgels (solid-like and core-shell) with and without single-cells. In this model, force-indentation, contact area- time, von Mises stress, and the stiffness of particles were extracted as the results. Additionally, the effect of different indentation depths and velocities on particle mechanical properties were investigated by the indentation model. The CFD model was used for evaluating the throughput of the two confinement channels with different confinement lengths. Finally, the mesh convergence and program validation were also explored.

The rest of the document is organized as follows:

Chapter 2 Presents the state of the art and theory. Begins by presenting the basics of GelMA synthesis, the influence of microgels structure using DBMS in cellular applications, and the importance of mechanical characterization of them would be outlined.

Chapter 3 Explains our approach to (i) Fabrication of the droplet-based microfluidic chip for microgels generation, (ii) GelMA synthesis and pre-polymer solution preparation as the base material, (iii) GelMA microgels generation, and (iv) GelMA and microgels characterization.

Chapter 4 Presents the model design and results of the perception computational analysis of particles passing through confinement channels. This analysis encompasses two models of particles indentation, and CFD analysis.

Chapter 5 A summary of key findings of the thesis is presented and some apparent directions are envisioned.

Chapter 2 Theory and State of Art

This chapter starts by introducing the materials and synthesis process of GelMA hydrogel. Next, it shows the state of the art in droplet-based microfluidic systems for microgels generation. The importance of experimental and computational characterization of soft particles is depicted next. At the end, the technique for cell transfection based on cell deformation is presented.

2.1 GelMA: Material Properties and Synthesis Parameters

Gelatin-methacrylate commonly referred to as GelMA has grown in popularity in applications, such as tissue engineering [31], drug delivery [32], 3D cell culturing [33], and electrochemical sensors [34]. GelMA is considered as a photo-crosslinked hydrogel, which consists of gelatin, modified by methacrylic anhydride (MA). When gelatin is added to methacryloyl side groups of methacrylic anhydride, a large number of amino groups presenting on gelatin side chains are replaced by these groups, resulting in the formation of GelMA. This modification causes GelMA molecules to undergo the polymerization process in the presence of a photoinitiator (PI) and a UV light source through which the covalent crosslinking would be emerged [35]. These features endow GelMA with suitable biological properties, tunable physical characteristics, excellent biocompatibility, degradability, and low-cost. Because of these properties, GelMA is being used excessively in 3D cell culturing, drug delivery, and tissue engineering. Furthermore, controlling the porosity is the other important feature of this material since a specific porosity is desirable for each application.

Since the mechanical properties of GelMA can be tuned based on the desired application, there are no specific fixed values for GelMA's mechanical properties, i.e. Young's modulus (YM) and plasticity. The mechanical properties of GelMA is related to its synthesis parameters, and they would be modified by altering any of those. For instance, Nichol et al. [36] reported the variation of GelMA's Young's modulus by alteration of degree of methacrylation. As is shown in Figure 2.1A, an increase in the degree of methacrylation (from low-GelMA to high-GelMA) would increase the stiffness and the Young's modulus of GelMA. Besides, in the same study, the direct

relation of mass/volume fraction with Young's modulus is shown in Figure 2.1B. It was clear that for the higher GelMA concentration of higher degree of methacrylation (Medium-GelMA and high-GelMA), the compressive modulus (CM) increased significantly. Furthermore, Bertassoni et al. [37] depicted the dependency of Young's modulus of GelMA with different concentrations on UV exposure time. As is illustrated in Figure 2.2, the Young's modulus increased by an increase in UV light exposure time, and this increment is more significant for 15% compared to 7% and 10% GelMA concentration [37]. Some previously reported data for mechanical properties of medium and high-GelMA is given in Table 2.1.

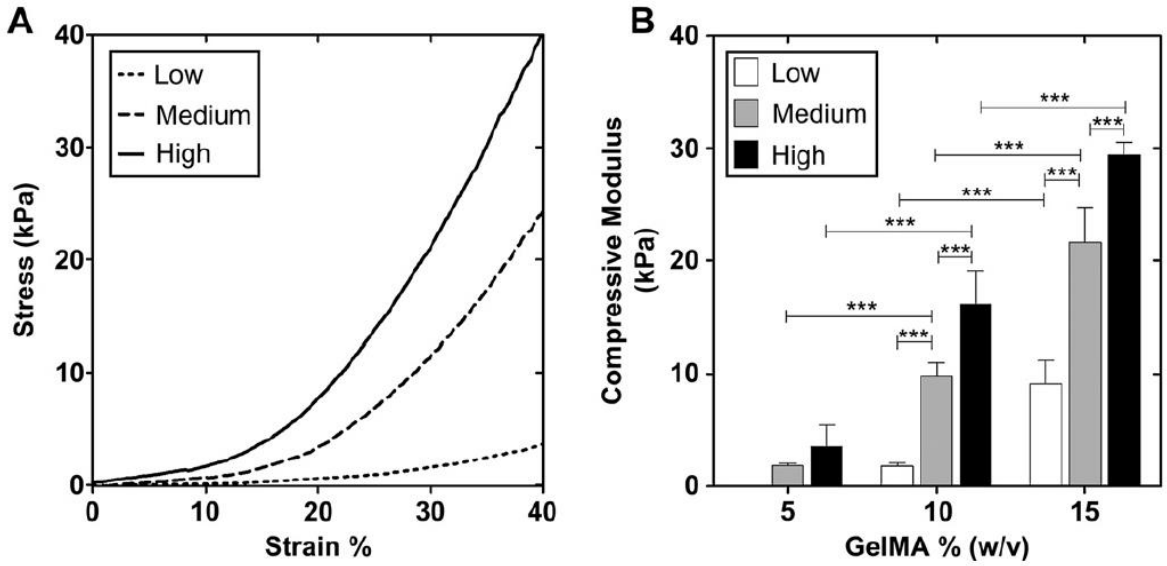

Figure 2.1: Mechanical properties of low, medium and high bulk GelMA hydrogel. A) Stress-strain curve of GelMA with different mathacrylation degree of low, medium and high. The high GelMA has the highest stiffness among all. B) Compressive modulus (kPa) at different degree of methacrylation degree in three different concentrations of 5%, 10%, and 15% (w/v). Adapted from Nichol et al. (2010)

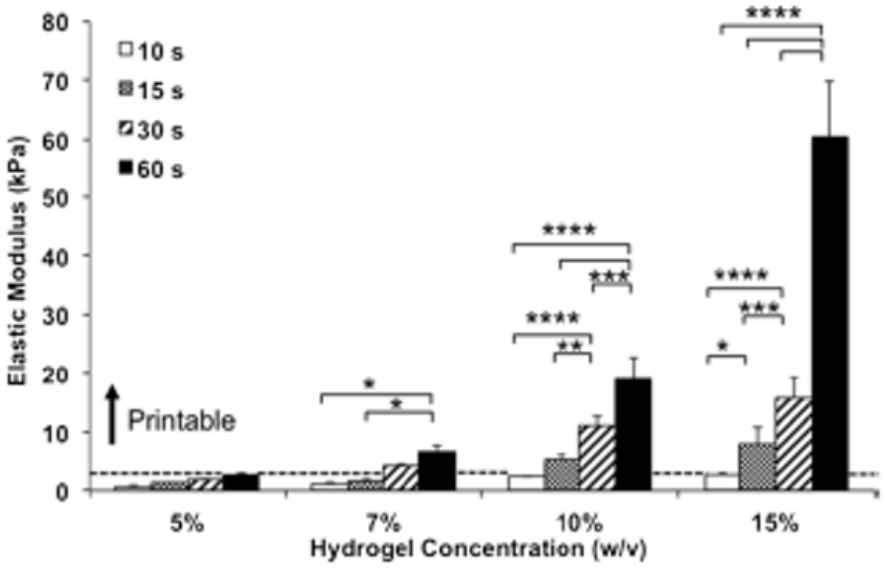

Figure 2.2 Elastic modulus of GelMA with varying hydrogel concentration from 5% to 15% at different UV light exposure times. Adapted from Berassoni et al. (2014)

Table 2.1 Previously reported GelMA mechanical properties and synthesized parameters.*

	Type of GelMA	volume percentage MA added to the synthesis reaction (v/v)	Added Photoinitiator (Mass/volume) (gr/ml)	GelMA Prepolymer (Mass/volume)	UV Exposure time	Degree of methacrylation (For Medium-GelMA)	Compressive Modulus (kPa), Young Modulus (kPa)	References
1	Medium	1.25	0.5% (Irgacure 2959)	5%	60 s (6.9 mW/cm2 UV light)	53.8 ±0.5%	CM ~ 2	[36]
				10%	60 s		CM ~10	
				15	60 s		CM~22	
2	Medium	2.2	0.5% (Irgacure 2959)	10%	2 min (CL-1000, Funakoshi, Tokyo, Japan)	52.5±1.2%	YM 17.1+/-2.4	[38]
3	High	20	0.5% (Irgacure 2959)	5%	60 s (6.9 mW/cm2 UV light)	81.4±0.4	CM ~4	[36]
				10%	60 s		CM ~11	
				15%	60 s		CM ~29.5	
4	High	11.11	0.5%	10%	2 min	91.7±1.4	YM	[38]

			((Irgacure 2959) V		(CL-1000, Funakoshi, Tokyo, Japan)		29.9± 3.4	
5	NR	NR	0.5% (Irgacure 2959)	7%	60 s	NR	YM 19± 3.5	[37]
				10%	60 s		YM 6.5± 0.8	
				15%	60 s		YM 60.3± 9.5	
6	High	NR	0.5% (LAP)	5%	2 min	96%	CM 2.86 ± 0.10 YM 2.08 ± 0.43	[39]
					GelMA Microgels			
7	High	8%	1.0% Wt (2-hydroxy-4'-(2-hydroxyethoxy)-2-methylpropiophenone)	7.5 wt %	20 s (6.9 mW cm −2)	75%	YM 1.5±2	[40]

*In all the above experiments, the mechanical properties were measured at room temperature. Same type of Gelatin was used in all the cases, gelatin from Procine Skin Tape A.

2.2 Droplet-Based Microfluidics and Microgels Generation

GelMA (Gelatin-methacrylate) microgels have great performance in cell colony formation in compression with bulk hydrogel, which suffers from poor nutrient exchange for cells proliferation [41]. Microgels (solid-like and core-shell) such as alginate, agarose, and GelMA have been commonly used for cell encapsulation as it can provide a 3D culture environment [42-44]. Encapsulation of cells in microgels can be leveraged to advance analysis of an individual cell or a limited number of cells within 3D microenvironments, facile manipulation, and characterization [45].

Between core-shell and solid-like microgels, core-shell microgels are more favorable in terms of forming cell aggregates within, providing well-defined spatial structures, and cell protection during a suspension culturing [46].

One method which can give good homogeneity for the fabrication soft particles is using the droplet-based microfluidic systems, which are applicable in both solid-like, and core-shell fabrications. A droplet-based microfluidic system is defined as a microfluidic system that causes the breakup of a continues flow into small droplet volumes [47]. Owing to the operation at small scales and low-waste reagents, this technology has enormous applications in chemistry, biology, i.e. analysis of individual cells within 3D microenvironments [45].

Hydrodynamic flow focusing, as a complementary technique has a trace in droplet-based microfluidic systems. This can be defined as a sample focusing tool that commonly refers to confinement of an inert flow between two sheaths flow [48, 49]. This technology has also been offering potential and practical applications in cytometry [50, 51]**.**

The application of droplet-based microfluidic system is vast, ranging from drug delivery, imaging, and diagnostics to chemical synthesis of nano and microparticles. Herein, the biology applications of droplet-based microfluidic is pointed out. Several articles regarding the application of this system and microgel structures in biology have been reviewed as follows:

Guermani et al. [52], using a 3D printing and microfluididc system could develop a tissue-like microgel array comprised of human mesenchymal stem cells. This was done by microprinting of

GelMA on a glass-slide, then crosslinking of the fabricated microgel array by UV light with an exposure time of 15 sec. After that, the culturing of the microgel array was done in sealed multiwall culture chambers containing cell media. In comparison to Hyaluronic acid (HA) hydrogel, they outlined that higher cell viability and cell adhesion and proliferation was observed for GelMA hydrogel.

Wang et al. [53] presented a droplet microfluidic system for one-step generation of GelMA core-shell microgels and purported the potential of these microgels in the fabrication of microtissues, and generation of organoids. To target this aim, a droplet-based microfluidic device was fabricated using photolithography. They used a water-in-water-in-oil (w/w/o) system in which the Methylcellulose (MC), GelMA, mineral oil were used as core, shell, and continuous flow, respectively. The effect of flow rates of different inlets on the size of the fabricated core-shell GelMA microgels was studied. They found that as the continuous flow rate (shell and core were fixed in their flow rate), or the core-shell's flow rate (the continuous flow rate is fixed) increases, the overall diameter of the core-shell microgels grows as well. Moreover, an increase in the flow rate of either core or shell leads a significant increase in microgels size., while simultaneously reducing the dimension of its counterpart, i.e. The shell shrinks if the flow rate of the core is augmented and vice-versa. Furthermore, the concentration of GelMA was adjusted to demonstrate its effect on the overall diameter of microgels and it indicated a decrement in size as the concentration increased. To evidence the high biocompatibility of the core-shell microgels, first, hepatocyte cells were encapsulated, and then were centrifuged to remove the undesired mineral oil, and finally, their viability was monitored during a long-term culture. The result depicted the high viability of 15 days for encapsulated hepatocyte cells and further clarification of a raise in the core diameter with the culture time owing to cell proliferation.

The surface of GelMA microgels generated by water-in-oil (w/o) or water-in-water-in-oil (w/w/o) contains undesired mineral oil which prolongs the crosslinking process of UV-photosensitive hydrogels, and consequently, a decrement in cell viability. Mohamed et al. [46] addressed this limitation and proposed an on-chip microgel formation, crosslinking, and oil filtration droplet microfluidic device. In this device, mineral oil and GelMA containing cells were used as a continuous flow, and core flow, respectively, and the filter microposts array was integrated for forcing cross-linked microgels to pass the interface between the oil and the aqueous washing buffer (Tween 80). In this system, the thin oil surface of microgel would be separated by

the oil layer. To assure a reasonable distribution of cells among monodispersed microgels, a magnetic mixer was utilized in GelMA containing cells syringe. Bavin serum albumin (BSA) also was used to treat cells before mixing with GelMA to avoid cellular aggregation. This paper established the maintenance of cell viability (85 % on day 1) for 5 days.

Additional unprecedented advantages and applications of single-cell encapsulation in microgels are in genome editing systems. For instance, Liu et al. [54] presented two droplet microfluidic devices for profiling the gene expression of cultivable cells by the approach of Isogenic Colony Sequencing (ICO-Seq) at high throughput. Two main steps of encapsulation of cells into 90 um agarose microgels and RNA barcoding of cell colonies are conducted using those two different droplet microfluidic devices (Figure 2.3a),b)). As is shown in Figure 2.3c), to facilitate the agarose droplets generation, three droplet splits are used for splitting each melted agarose droplet into two, four, and then eight beads. These splits were employed after the spiral mixing channel to ensure the presence of an equivalent amount of cells and agarose solution. The fabricated molten agarose droplets were then transferred into ice to solidify. After that, they were centrifuged to remove the oil and transferred to cell media for culturing. When the colonies of cells were formed, they were injected into the second microfluidic device for barcoding using RNA in lysis buffer (Figure 2.3d)). Finally, the agarose microgels within barcoded cell colonies were demulsified and proceed to the step of sequencing (reverse transcription, PCR). With this work, they successfully demonstrated the proper application of agarose microgels in accessing gene expression information of a colony of tens to hundreds of cells, rather than of single cells. This illustrates the advantage of reducing the error owing to noisy single-cell gene expression profiles, and amplifying the RNA amount used for RNA barcoded sequencing.

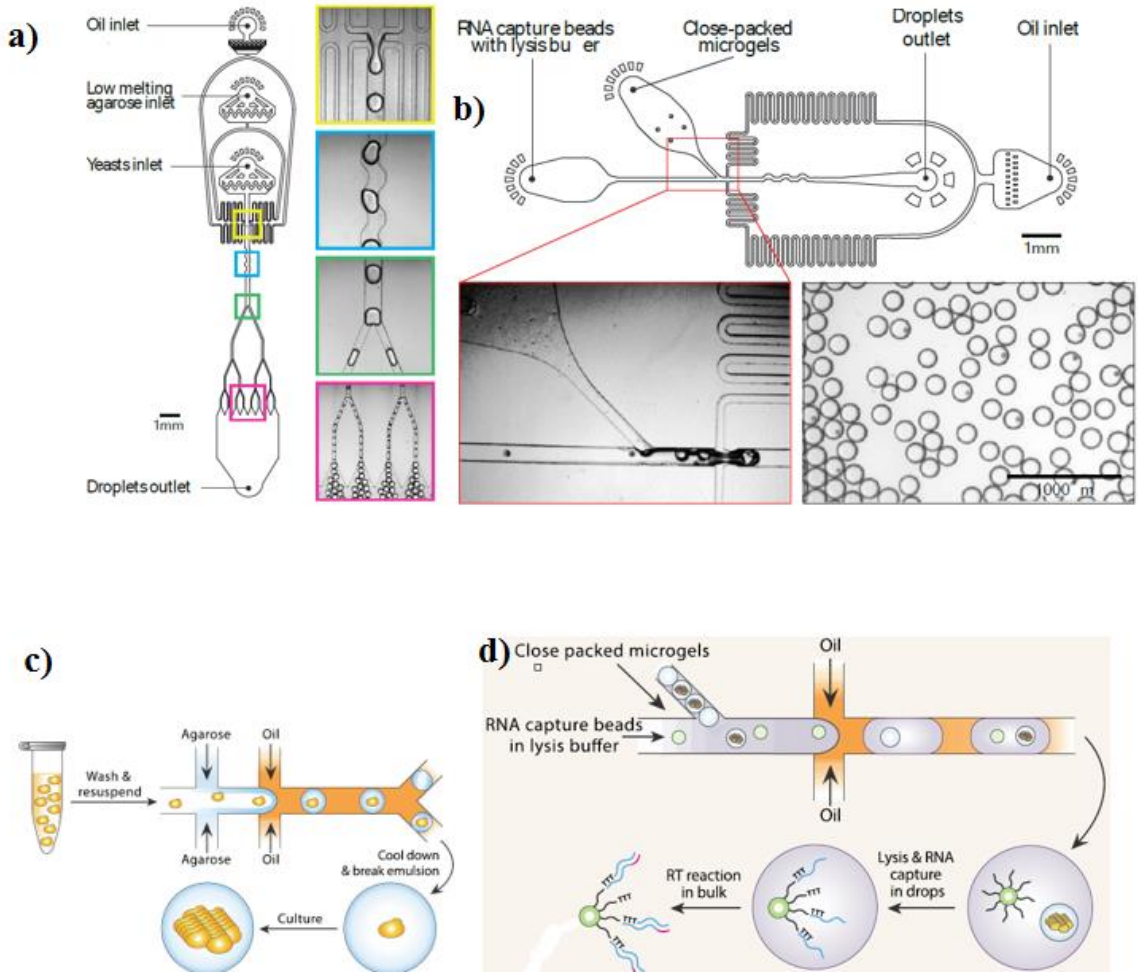

Figure 2.3 a) Microfluidic device design consisting droplet generator junction, mixer, and two droplet splitters. The setup is used for single yeast encapsulation into agarose microgels. b) Microfluidic device for co-encapsulation of agarose microgels and barcoded RNA capture beads. c) Colony formation of yeast cells in agarose microgels during off-chip process. d) Co-encapsulation of yeast colonies and RNA capture beads, and demulsification of droplet contained agarose and agarose itself for a further bulk reverse transcription reaction. Adapted from Liu et al. (2019)

2.3 Characterization of Soft Materials and Microgels

Having discussed the effectiveness of micro/Nano soft particles. i.e. microgels in a variety of applications such as drug delivery, material carriers, tissue engineering, and genome editing makes the characterization of these particles so vital for any desired application. For instance, as the carrier of materials in industry or medicine, these microgels (microcapsules (core-shells) or solid-like) must meet the optimal mechanical properties in the presence of load or pressure which are

used as the most common trigger parameters in carriers activation (in the progress of the self-healing process and delivery of materials) [55].

There are several methods which have been used excessively in the characterization of micro/Nanoparticles, such as Atomic Force Microscope (AFM) [56], nanoindentation [57, 58], optical/magnetic/acoustic tweezers [59-61], microfluidic deformation based on shear flow or confinement channel [62], and micropipette aspiration [63, 64]. Among these techniques, indentation and AFM are the most common, and microfluidic deformation-based techniques are the highest throughputs methods to apply on micro/nanoparticles.

Nano-indentation or depth-sensing indentation is a method for the measuring of mechanical properties of small volumes samples. This technique enables small loads and penetration depths (displacements) to be simultaneously recorded and controlled with sub-nanometer accuracy and precision over a predefined load cycle (a load, hold and unload period) [65]. This method can be used to determine the modulus of elasticity, hardness, yield strength, fracture toughness, creep, and plastic depth/contact depth [66]. A nanoindenter has several tips with different geometries, like spherical, cylindrical, and flat that are made commonly out of hard metals or ceramic materials, like steel or diamond [67]. Based on the geometry of specimens, the proper tips will be selected [68]. Nanoindenter dimensions are very small, some less than 50 microns. A schematic of a simple nanoindenter is shown in Figure 2.4 [69].

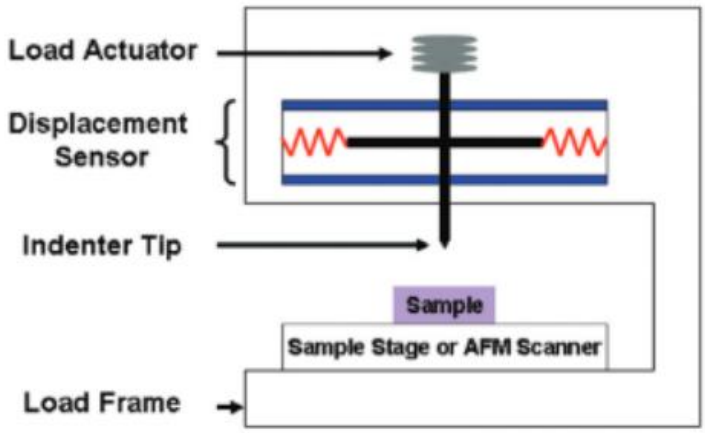

Figure 2.4 Schematic of a nanoindenter system. Adapted from Ebenstein et al. (2006)

To illustrate more, using the Nanoindentation technique, Cha et al. [70] evaluated the elasticity of GelMA microgels. The test was performed using AFM-assisted indentation and the force vs. displacement curve was obtained. Applying the Hertz equation in the linear region of the achieved curve, Young's modulus was computed 1.872 kPa approximately. Among articles related to the indentation and AFM methods in characterization of soft particles, some combined the experimental data with FEM analysis and optimization methods [71, 72]. This can enable the identification of particles' parameters model (Viscoelastic, elastic, poroelastic, etc.) easily and fast. Additionally, in the case of cells, this method makes it possible to extract parameters related to the subcellular structure of living cells. Moreover, solving a complex equation and high computation speed next to the possibility of considering irregularity of particles' geometry, like when we are dealing with a spread cell (with non-uniform thickness), can be considered as another advantage of FEM analysis.

When it comes to Hydrogels, tissues, and living cells, the vital parameters which have an impact on the mechanical characterization of soft particles in the experimental and numerical tests can be categorized as; (i) The constitutive models such as poroelastic, hyperplastic, viscoelastic, and viscohyperplastic materials during mechanical penetration in defining materials [73-76], (ii) Indentation parameters which have an influence on mechanical properties, including indentation depth, load and indentation rate, indentation tips [77], and (iii) Materials geometry and concentration.

To emphasis the application of FEM simulations in extracting mechanical properties of a material, like GelMA hydrogel and the need in determining the proper material model, Castilho et al. [78] addressed the difficulties associated with the characterization of micro-fiber reinforced hydrogels, and explored the possibility of considering FEM models to observe the reinforcement mechanism of the fabricated composite. The FEM modeling parameters extracted experimentally. Two FEM simulations of continuum and micro-model were used to represent the load-carrying capacity of hydrogel (GelMA) and scaffold geometry, and the actual deformation of the scaffold during the compression, respectively. GelMA was modeled as Neo-Hookean hyperplastic in the continuum model, and linear elastic in micro-model. The fiber scaffold (PCL) was modeled as a linear elastic in both models, while its designed geometry was different. It had a thin laminas geometry in the continuum model, and direct 3D micro-CT (computed tomography) reconstructed

geometry in the micro-model (micro-CT images of the constructs were converted to micro-FEM model using voxel conversion). What have been accomplished with this model were; (i) considering scaffold alone, interconnections, which were formed by multiple intersecting fibers would be more resistant compared to the fiber walls, whereas in composited constructs, the surrounding hydrogel would disperse the compressive load alongside the gel. This caused less stress on the junctions. (ii) the compressive modulus of PLC scaffold increased as it combined with GelMA hydrogel. This implied the reinforcement mechanism of scaffolds. Also, the deformed composite has the highest stiffness among deformed and non-deformed scaffolds and non-deformed composite.

In particular, for microcapsule and polymeric micro particles, Wang, XF et al. [79] outlined an optimization and computational analysis based on MATLAB software to adjust the constitutive parameters of a FEM of indentation of urea-formaldehyde (UF) microcapsules. They tried to minimize the difference between the experimental and numerical data. The investigated mechanical properties of UF microcapsules with an average diameter of 195.4 um were Young's modulus, yield stress, and hardening modulus. The experimental data was obtained from a nanoindentation method. To fix the individual UF microcapsule during the indentation, a thin layer of epoxy resin was spin-coated on a 1cm×1cm glass slide, then several equally sized microcapsules were placed on that and left for 24 hours to get dried. To prevent structural deformation owing to the Bercovich indenter, a low level of loading was considered. Upon the indentation, the active load was increasing by the contact area between the indenter and the microcapsule till it reached the pre-selected deformation (5 um), then the load was maintained for 10s to minimize the time-dependence plastic effect, and finally, the unloading step proceeded. ABAQUS software was used to extract the numerical data from the indentation simulation. According to the different consecutive models, like elastic-plastic with power-law hardening, elastic-perfectly plastic, and elastic-perfectly plastic with linear hardening, the initial parameters would be different. Hence, for each model a trial-and-error was performed. This way, a proper vector of initial points was given to the ‘Fminsearch’ optimization tool of MATLAB software and finally, after some iterations, the final parameters were obtained. It showed a perfect match between the computational result and experimental data.

Regarding the importance of indentation parameters, Esteki et al. [80] explored the effect of indentation velocity on the mechanical properties of poroelastic materials with the use of the finite

element simulation. The master curve of force against rising time was obtained as the final framework, which would eliminate the need for simulation and numerical analysis in the estimation of the poroelastic parameters of soft hydrated materials. This was achievable by just using indentation test. To validate the framework, agarose (0.6% and 1%) and polyacrylamide (PAAm) hydrogels were used for a micro and macro scaled indentation run by AFM and uniaxial tensile tester machine. Two approaches of constant and variable velocities were considered for FEM indentation simulation, and the force-indentation and force-relaxation curves were obtained for each case. To further elaborate on the effect of variable velocity, at the first step, the plots of force against time for a set of different maximum indentation depths were extracted numerically and experimentally (micro and macro tests). The microscale test performs relaxation test with a fixed maximum force, at an extremely high sampling rate, and micron-size indenter, to monitor pN to nN forces. However, relaxation test in the macroscale test works with a fixed maximum indentation depth, millimeter size indenter, at a low sampling rate, to monitor mN to N forces. For each maximum indention depth in the case of macroscale test, and maximum force (F_M) in the microscale test, the F_M vs. rise time was plotted. By applying Equation 2.1 and Equation 2.2, on the rise time, and F_M, respectively, all the curves would be collapsed into one single curve called a master curve for each test.

$$\tau_R = \frac{Dt_R}{R\delta_M} \tag{2.1}$$

$$F_M^* = \frac{F_M(\tau_R) - F_M(\tau_R = \infty)}{F_M(\tau_R = 0) - F_M(\tau_R = \infty)} \tag{2.2}$$

, where D is the diffusion coefficient, R is the indenter radius, δ_M is the maximum indentation used to normalize the rise time, and F^*_M is the normalized F_M. By considering the fact that the contact size is enormously smaller than the hydrogel thickness (5mm), even for large deformation with the condition of $\delta/R \sim 0.6$, the Hertz force-indentation relationship (Equation 2.3) is applicable and it can be applied on Equation 2.2.

$$F = \frac{4}{3}\sqrt{R}\,\delta^{3/2}\frac{E}{(1-\upsilon^2)} \tag{2.3}$$

Where E is referred to as elastic modulus. At $\tau_R = 0$, the volumetric changes are negligible, and at $\tau_R = \infty$, the volumetric change is fully observable (equilibrium state), and those would implicate the near-incompressible condition (Poisson ratio=υ=0.5), and compressible condition (Poisson ratio=υ), respectively. Assuming these conditions and using Equation 2.2, Equation 2.3 can be rewritten as:

$$F_M^*(\tau_R) = \frac{\frac{F_M(\tau_R)}{\frac{4}{3}\sqrt{R}\delta_M^{3/2}} - \frac{1}{1-\upsilon^2}}{\frac{1}{0.75} - \frac{1}{1-\upsilon^2}} \tag{2.4}$$

And finally, by applying Equation 2.2 and Equation 2.4 on the experimental data, and then fitting a curve on the obtained data, the empirical Equation 2.5 can be formulated for the master curve.

$$F_{empirical}^*(\tau_R) = 12.5 \exp(-2.63\tau_R^{0.12}) \tag{2.5}$$

Therefore, by combining the experimental data with the obtained equations, the poroelastic parameters of D, E, υ can be derived.

Concerning cells, nanoindentation combined with computational methods have been used widely to study cells' behavior in response to the mechanical penetration. Different articles have investigated the effect of selecting a proper constitutive model, its parameters, and indentation characteristics on a variety of cells [81]. For instance, Wang Lei et al. [82], first, explained the importance of vascular endothelial cells (VECs) characterization and their key roles in understanding variation in blood-brain barrier (specifically for drug delivery). They also studied the treating central nervous system disorders (i.e. Alzheimer), and then investigated an inverse finite element model to determine the bEnd.3 cells' mechanical properties. Single bEnd.3 cells' modeled as viscohyperelastic. Maxwell and Neo-Hookean were used as constitutive models for a viscoelastic, and hyperplastic part, respectively.

Florea et al. [83] employed three constitutive models of viscohyperelastic, porohyperelastic, and poroviscohyperelastic to model chondrocytes cell. Using an AFM nanoindentation test combined with a computational model, the stress-relaxation curve of chondrocytes cells at 5% strain was

extracted and compared for each model. It was concluded that the best model which could explain the stress-relaxation curve is the poroviscohyperelastic.

Next to the indentation method, microfluidic systems have shown promising results in the high-throughput characterization of soft particles. In particular, using microfluidics is the most convenient method in terms of performing single-cell analysis. However, target parameters in the characterization of particles would be defined as pressure, velocity, transit time, and not anymore the indentation depth and rate[84].

Adamo et al. [85] reported a high-throughput microfluidics-based approach to compute the cell stiffness by measuring the travel time of a cell through a narrow slit. As a proof of concept, this system was used for Hela cells. The designed microfluidic device was fabricated using deep reactive ion etching (DRIE) of silicon wafers, insulated with a 0.3 um thick thermally grown silicon oxide, and anodically bonded to a glass wafer with two deposited gold electrodes located before and after constriction channel. The channel diameter (15 um), the narrow slit width (7 um), and the channel length were selected in specific for the manipulation of Hela cells (10-15 um). By applying a low voltage of 1V with a low frequency of 20 kHz, the electrodes would capture a flat signal, which was related to the electrical field, without any cell presence. According to Figure 2.5, after a cell passed the first electrode, since cells act as dielectrics in low frequencies, the peak h1 would be appear in the readout signal which corresponded to cells' size (Foster Shawn theory and by analogy with the Coulter principle [86]). When cells passed through the constriction, the signal would show a peak at h2, and again it would decrease to h1 and then to the flat bias. Cell travel time can be calculated by measuring the width of the bell-shaped part of the signal, which obviously is related to the size of the cells (h1). Moreover it was depicted that the travel time increases by growing the value of h1.

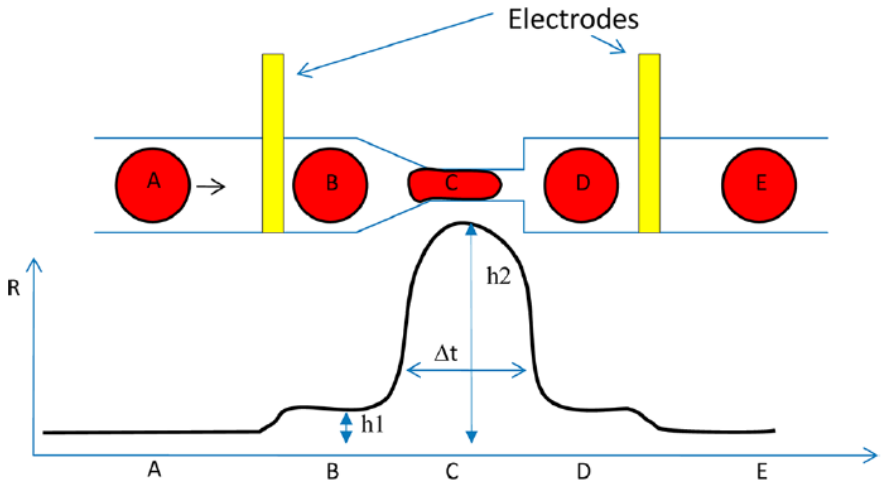

Figure 2.5 Schematic of the microfluidic system used to extract deformability of single cells. The electrical signal recorded by the embedded electrodes was shown against the cell position. The resistance increases as cell passes through the channel and has a pick at position C, then it would reduce as it is exiting the confinement channel. Finally it would go back to baseline at position E. Adapted from Adamo et al. (2012)

2.4 Cell Transfection by Single-Cell Mechanical Deformation Using Microfluidic Systems

Next to the application of microfluidic systems in mechanical penetration of soft particles for characterization, they can be used as a method for intracellular delivery, genome editing, and cell transfection [13, 87, 88].

Delivery of material into a cell has been a long-standing challenge in biology [89]. Figure 2.6 compares the current methods based on transfection efficiency [90]. As it is conspicuous, mechanical-electrical and microinjection methods have the highest transfection rates among the other techniques. Viral vectors are a precise method commonly used to deliver DNA and RNA into cells. The delivery potential of viral vectors is limited by the risk of integrating viral sequences into the genome, and DNA contamination [91].

Chemical methods work based on penetrating peptides or nanoparticles by doing some chemical functionalization. This approach is limited to certain applications [91, 92].

Microinjection method is in the category of mechanical disruption technique, and is based on using a pipette and skilled operator, or recently, an automated arm and setup to inject into the

cells. Being low-throughput, high-cost, and time-consuming are among the drawbacks of this method [93].

Electroporation is another promising technique that shows a high success rate. However, in a recently published paper by DiTommaso et al. [94], this technique was compared with the cell squeezing technique and it was reported that the cell functionality in the case of electroporation would drop significantly. In another word, squeezing techniques have fewer side effects than electroporation. This issue was also addressed by Takahashi et al. [95].

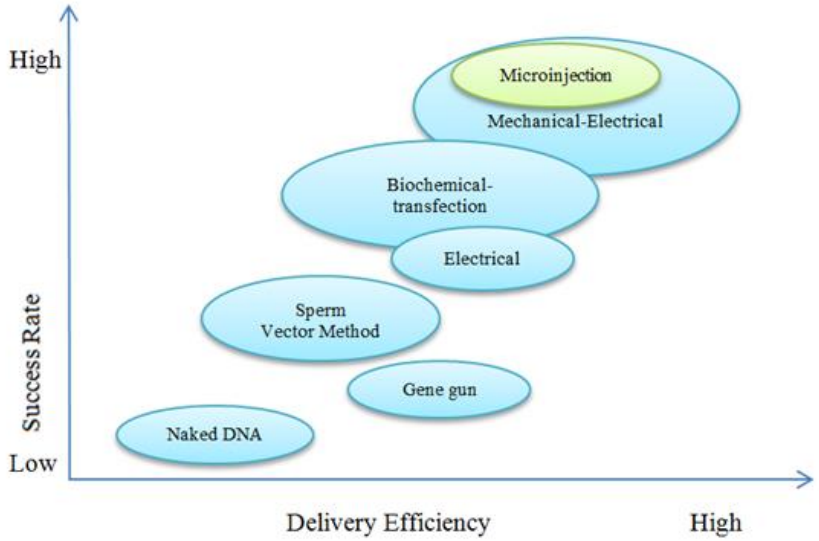

Figure 2.6 A comparison of the efficiency and success of delivering exogenous substances into cells by different methods. Adapted from Zhao et al. (2019)

Rapid mechanical deformation of cells using a constriction microfluidic system, also called cell squeezing, is a method that has been used widely for measuring the mechanical properties of cells [29]. Recently, this method is used for cell transfection and intracellular delivery, which causes the formation of transient holes on the cell membrane and makes it possible to deliver carbon nanotubes, proteins, macromolecules, vectors, DNA, RNA, etc. According to Figure 2.7, these cell squeezing systems mostly have multi parallel narrow channels with a media (buffer) containing gene-altering materials, and when the cells are squeezed, the pores on the cell membrane would open up and result in introducing foreign materials into cells [96].

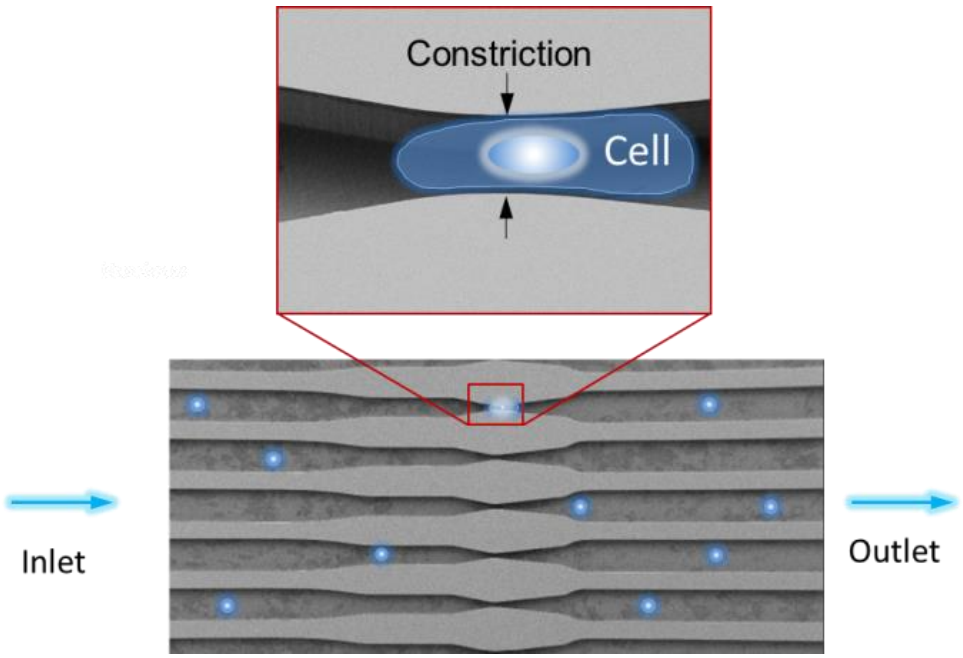

Figure 2.7 Cell deformation when being forced through constriction channels. Parallel confinement channels are considered to increase the throughput of the device. Adapted from Sharei et al. (2013)

The advantages of this method over the other transfection methods, like viral vectors, chemical methods, microinjection, and electroporation are (i) being vector-free, (ii) single-cell manipulation, (iii) high-throughput, and (iv) compatibility with many cell types [97].

In the development of cell transfection-based microfluidic confinement channels, the fabrication of a cost-effective microfluidic device with a high cell functionality, transfection rate, throughput, and delivery efficiency have been the topic of study for researchers. Some studies are related to the chip geometry and the design [98]; some focused on the delivery of different materials and particles to widen its application from cell reprogramming to sensing [25, 99, 100], and finally, some targeted the comparison between cell squeezing systems and electroporation or other techniques in terms of cell functionality and delivery efficiency[25, 101]. However, there still exists a need for fabrication of low-cost microfluidic chips and better formulating and understanding the effect of channel's dimensions, consequent forces, and cell speed, on delivery efficiency and cellular functionality. In the current design of the fabrication of microfluid-based confinement channel, the common concerning parameters for cell transfection are confinement channel's dimension and flow velocity, which is usually optimized experimentally and not computationally.

For instance, Sharei et al. [96] developed a microfluidic-based constriction device for cytosolic delivery through rapid cell membrane disruption and formation of transient holes, which cause the diffusion of surrounding materials present in the buffer into cells. The size of these transient holes would depend on the shear and the compressive force applied on single cells upon being confined by a channel with the diameter of 30-80% of the cells'. With this method, they could successfully demonstrate the delivery of a variety of particles for different purposes of cell reprogramming to carbon nanotube-based sensing i.e. Apolioprotein E, BSA, GFP- plasmids, PEG1000-coated, and 15-nm gold nanoparticles. In another study, Han et al. [26] using a microfluidic membrane deformation, they could successfully deliver CRISPR-Cas9 into the cytoplasm f cells to be the first pioneer group in CRISPR-Cas9 genome editing method using the mechanical deformation of cells. The advantage of their method was to delivery of siRNA and plasmids in hard-to-transfect cells, such as stem cells with high delivery efficiency and cell viability.

It is an open area to improve gene-delivery steps, the most important factors to be considered are delivery efficiency, viability (success rate), and cell functionality. Delivery efficiency is defined as the fraction of alive cells containing delivery materials, and cell functionality is referred to as minimizing nonspecific and unintended changes to cell phenotype, which may adversely impact the functionality potential. These factors vary by different parameters i.e. cell speed, numbers, and the length and diameter of the constriction channel [101]. To study the circulating tumor cells Cognart et al. [98] used a microfluidic-based confinement channel with Metastatic breast cancer cells of epithelial-like and mesenchymal-like phenotypes injected in channels. They conducted a gene expression analysis of key regulators of epithelial-to-mesenchymal transition and showed the significant changes in genome expression, in addition to DNA damage upon circulation. In another study, Liu et al. [101] explored the cells response to mechanical forces in microfluidic-based confinement channel. Their study depicted the transition of cell behavior from elastic to viscoelastic upon rapid compression and acting more like viscose material at faster deformation rate. Also, higher volume loss was observed at higher flow rate.

.

Chapter 3 Microfluidic Device Fabrication

This chapter starts by presenting the design of microfluidic chips using three techniques of soft lithography, stereolithography, and cutter plotting. Next, the fabrication of devices and a comparison between them have been demonstrated.

3.1 Microfluidic Design Method

Microfluidic devices were designed to enable GelMA microgels solid-like and core-shell fabrication in high-throughput. A droplet microfluidic system with two cross-sections (T or Y) was fabricated using three different techniques of cutter plotting, soft lithography, and stereolithography. The disadvantages and advantages of each technique were detected for the application of a droplet-based microfluidic device in microgels fabrication.

Microfluidic devices were first designed using SolidWorks, and the generated files were then used in the proper machines based on the selected technique. In fabrication of the microfluid devices, following materials were used: Pressure Sensitive Adhesive (PSA), Polyvinyl chloride (PVC), 2 mm acrylic sheet, Polydimethylsiloxane (PDMS), SU-8 2025.

3.1.1 Fabrication of the Microfluidic Chip Using Soft Lithography

Using a spin coater, a thin layer (70 um) of SU-8 2025 was spin-coated on a previously washed glass slide, and then soft-baked. The program that was used for spin coating contained four steps, each with unique acceleration, time, and speed values (Figure 3.1). After spin coating, the mask with patterned microfluidic design (including channels and chambers) was fixed on the coated glass using four clippers, and exposed to UV light for a specific amount of time. Next, the post-exposure baking step was applied at two different temperatures, and then the chip was washed in a container filled with SU-8 developer, while continuously shaken manually. After removal of the unreacted photoresist, the device was dried by an air gun. The patterned glass slide was immersed in PDMS with a thickness of 5 mm and degassed using a vacuum desiccator for 30 minutes. After that, it was placed on a hot plate for 10 minutes at a temperature 95^0C to cure the PDMS. Finally,

after peeling the patterned glass slide from the PDMS, the PDMS device was bonded with another clean glass slide via an oxygen plasma treatment machine [102].

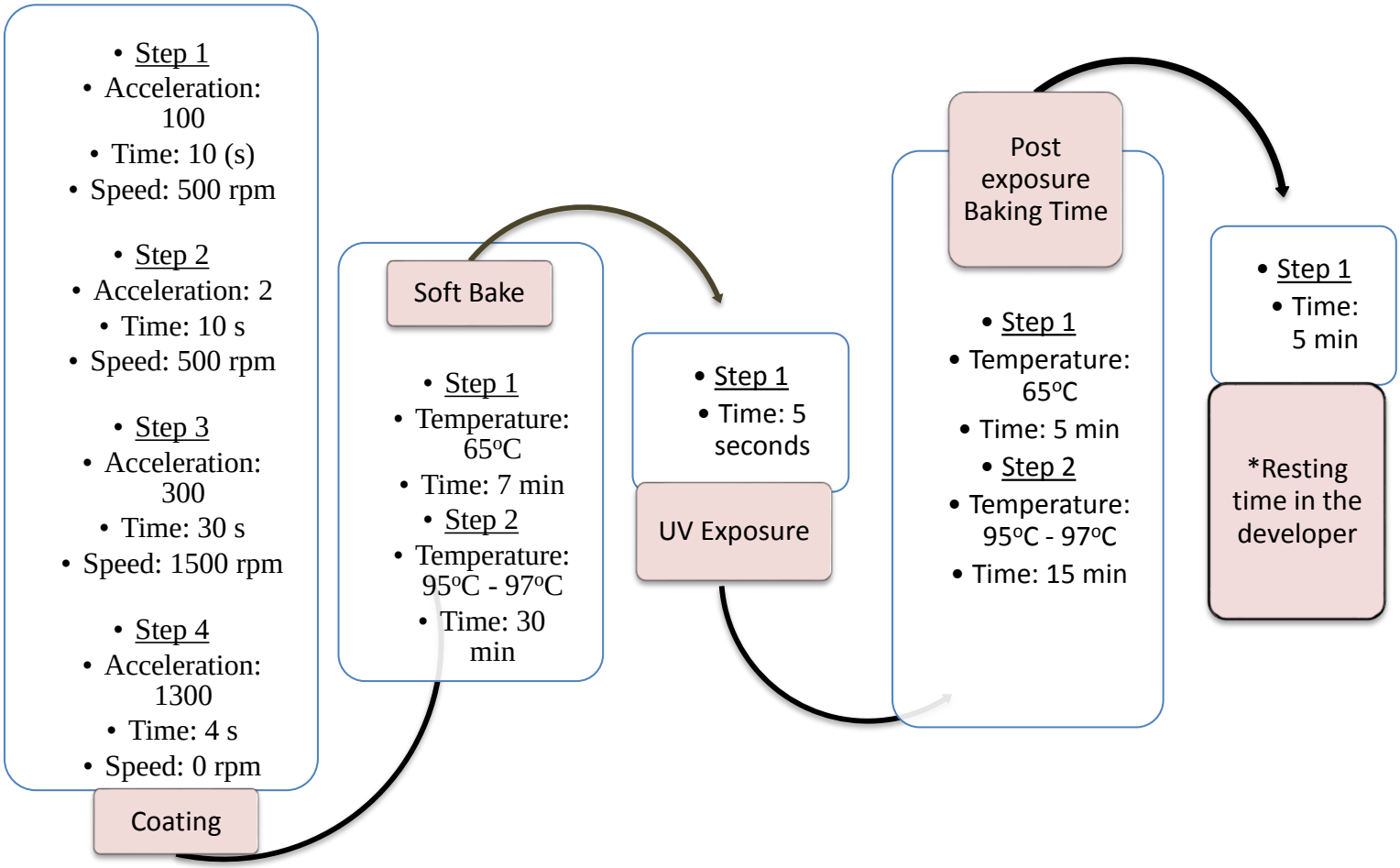

*More than 10 minutes would make the whole mask to be removed from the glass slide.

Figure 3.1 Soft lithography steps used to fabricate the droplet-based microfluidic device

3.1.2 Fabrication of the Microfluidic Chip Using Stereolithography

The FormLabs Form 2 device was used for 3D printing of a droplet-based microfluidic chip. The design was comprised of two coaxial cylindrical channels with two different diameters. The diameter of the inner channel was selected such that no polymerized resin would block the inside

of the channel. In doing so, core-flow channel with different diameter of 0.3, 0.5, 0.6, and 0.7 mm were printed. After trial and error, a minimum diameter of core-flow channel was determined to ensure a free path through all the channel. The Middle Channel's diameter was larger than the inner channel. Figure 3.2 shows the schematic of the deigned device and Formlabs Form 2 3D printer.

After printing the device, it was placed in isopropyl alcohol for 20 minutes to wash the uncrosslinked resin.

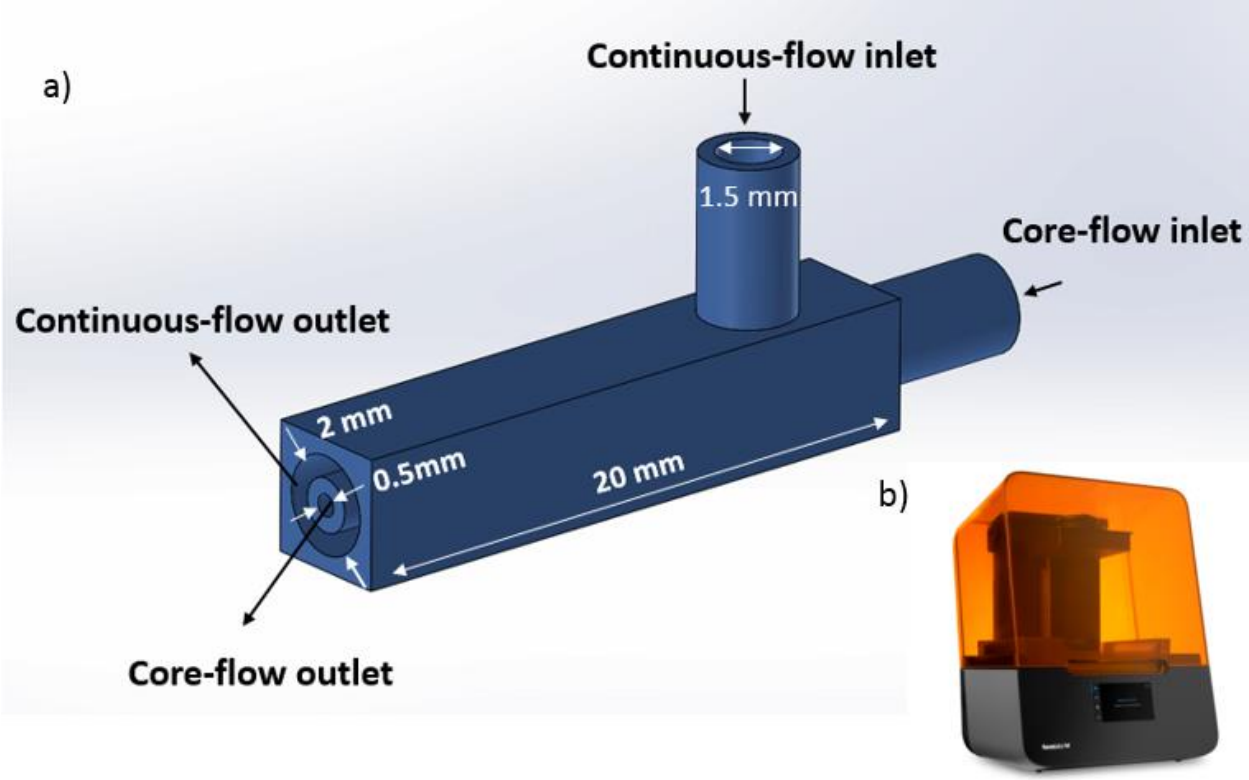

Figure 3.2 Stereolithography technique. a) Schematic showing the microfluidic device 3D model with two coaxial cylindrical channels. b) Formlabs Form 2 3D printer

3.1.3 Fabrication of the Microfluidic Chip Using Cutter Plotter and Laser Cutter

Rectangular-shaped microfluidic platforms are designed either with seven layers , or five. To fabricate the microfluidic channels with varying heights, each layer had its specific size and design,

and was selected from PVC, PSA, or acrylic. Most of these materials are extremely low-cost and widely accessible. A laser cutter was used to cut the acrylic layers and a cutter plotter with a resolution of 0.3 mm was utilized to cut the PSA and PVC layers. The inlets and outlets of microfluidic devices were laser cut on an acrylic sheet. The PSA layers were used either as adhesive layers (secondary layers) or main layers (for the channels). As main layers, the channels that needed a small thickness of 0.08 mm were printed on PSA (using a cutter plotter), and layers with the thickness between 0.1 to 0.2 mm were printed on PVC which its dimension is approximately 0.1 mm. Higher thicknesses are achievable through assembling 2 or more of them. To have a channel with varying height, the desired pattern was cut on one or several layers but not on the rest. To have a 3D structure, ordering of the layers just matters. With this method, channels with a thickness of 0.07mm or more can be printed accurately at exceedingly low-cost.

Figure 3.3 shows a breakdown of the seven-layer chip, composed of two acrylic layers (thickness: 2 mm), three PSA (thickness: 0.08 mm), and two PVC layers (thickness: 0.1 mm). The top acrylic layer only contains inlets and the outlet to be further connected to syringe pumps.

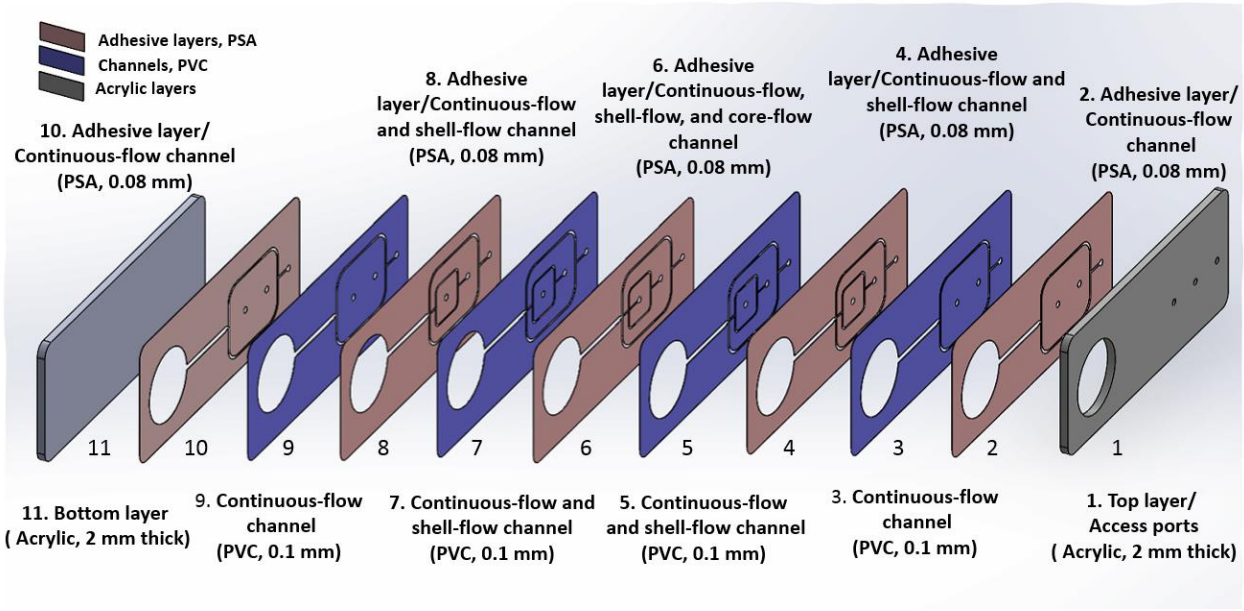

Figure 3.3 Schematic showing the layers of the multi-level 3D droplet microfluidic. The gray color, purple color, and the reddish color are representing acrylic layer, PVC layers, and PSA layers, respectively. Acrylic layers are 2mm thick, and PSA and PVC layers are each 0.08 mm, and 0.1 mm thick, respectively. The core-flow channel is just printed on the layer number six. The top layer encompasses all the access ports. The bottom layer is a featureless acrylic plate and used to cover the bottom side of the chip.

3.2 Results

The fabricated microfluidic device using lithography is shown in Figure 3.4. Using an inverted microscope, the thickness of the chip was measured as 69 um. Although photolithography technique is able to make small channels with high accuracy, this method is costly and time-consuming. Furthermore, advanced fluid routing and functionalities often require multiple lithography steps in the fabrication of channels with varying thicknesses, a manual process which suffers from dependence on individual skill and poor reproducibility. Besides, this increases the complexity of this technique. Nonetheless, this method is recommended for the fabrication of devices or channels with a size of less than 200 microns.

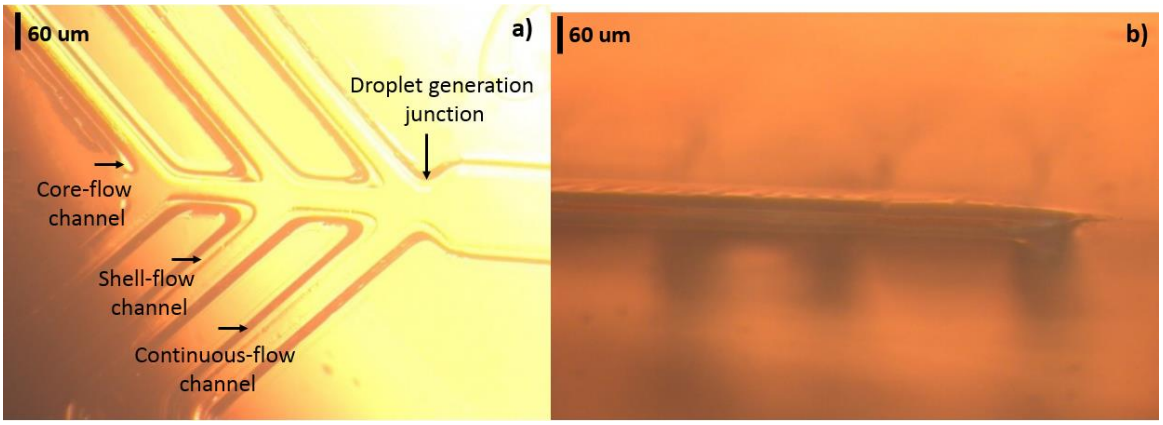

Figure 3.4 Fabricated microfluidic device using soft lithography. a) The flow-focusing junctions. b) The thickness of the channels.

Using 3D stereolithography and the design shown in Figure 3.4, several microfluidic devices with core-flow channel diameter of 0.3, 0.5, 0.6, and 0.7 mm were printed. However, only the core-flow channels with a diameter of more than 0.5 mm were printed successfully without being blocked by the polymerized resin. Figure 3.5, shows the printed droplet-based microfluidic device with two coaxial cylindrical channels with diameters of 0.5 and 2 mm.

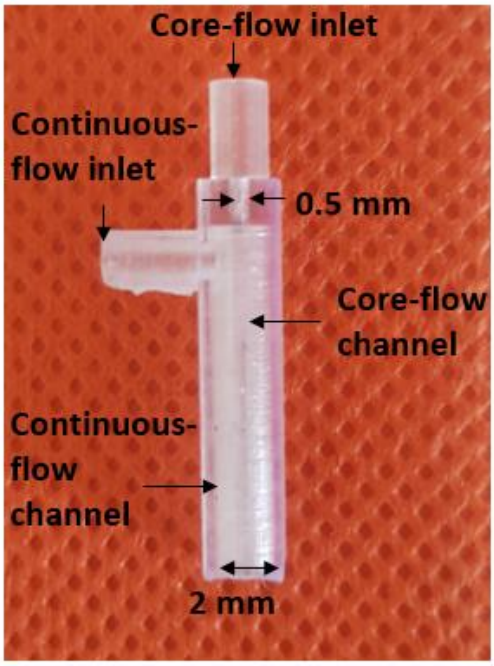

Figure 3.5 The fabricated droplet-based microfluidic device using stereolithography.

Due to the turbidity induced by layer by layer operation of the stereolithography machine, the channels were not transparent. This made it difficult to see the internal parts under a microscope. As shown in Figure 3.6, SEM was used to see the roughness of the channel surface.

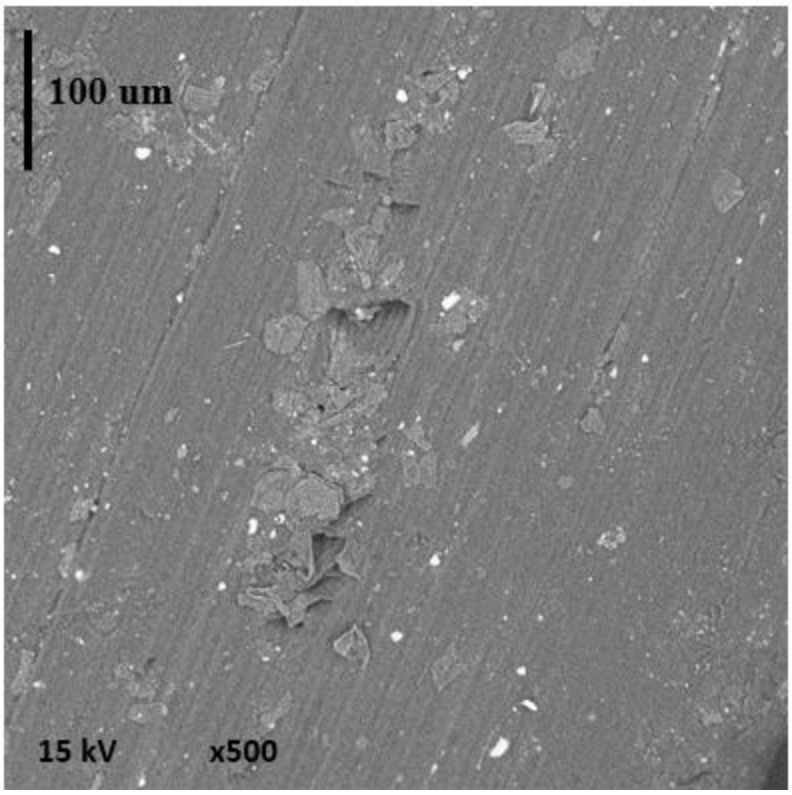

Figure 3.6 The layer by layer structure of printed droplet-based microfluidic device using stereolithography. This caused the turbidity of the printed device.

There have been some recommended methods to eliminate this issue. i.e. sanding the chip, dipping it in another transparent material. However, these are more practical for millimeter or centimeter-sized channels that their internal surfaces can be sanded or would not be blocked by dipping in external chemicals. Furthermore, the fabrication of larger size channels to apply these solutions needs higher material consumption which is not efficient. Stereolithography method despite being a low-cost and simple fabrication method is a relatively time-consuming technique that printing each chip with the highest resolution took us at least 6 hours.

Cutter plotting as the third technique was used for the fabrication of the microfluidic devices. In addition to its accuracy, the advantages of this technique compared to the other two techniques is its low-cost and simple procedure. Furthermore, the fabrication of channels with varying thicknesses in 3D format is not complicated compared to the photolithography technique. Figure 3.7 shows the fabricated chip with the following dimensions: 480 um (Mineral oil channel), 280 um (GelMA channel), and 80um (water channel).

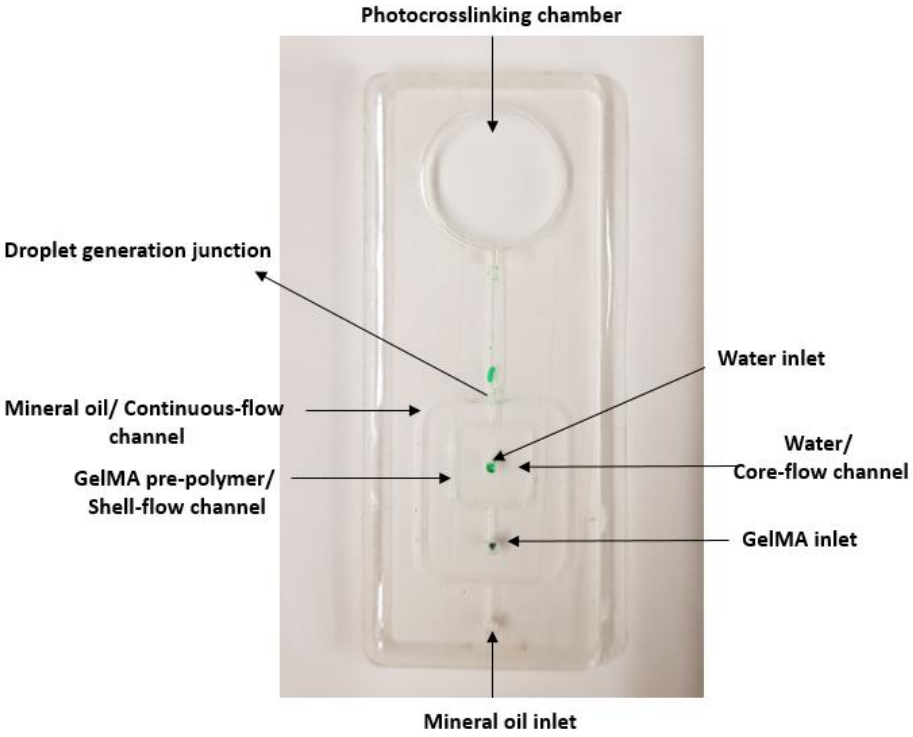

Figure 3.7 Fabricated droplet-based microfluidic using cutter plotting technique.

Table 3.1 summarizes the advantages and disadvantages of the three techniques of photolithography, stereolithography, and cutter plotting.

Table 3.1 Comparison of various microfluidic fabrication techniques.

Techniques	Advantages	Disadvantages
Photolithography	- Proper for channels with small dimensions of less than 300 um - Precise with high resolution	- Expensive - Multi-step procedures - Time-consuming.
Stereolithography	- Simple procedure - 3D structure useful for many application	- Non-transparency (turbidity) - Not suitable for channels with dimensions less than 500 um - Blockage
Cutter plotting	- Simple Procedure - Constructing 3D structure can be possible - Low-cost - Precise for channels with thickness higher than 80 um	- Not suitable for channels with dimensions less than 80 um.

Chapter 4 Microgel Generation and Characterization

This chapter starts by presenting the synthesis of GelMA and the preparation of the pre-polymer solution. After this, the fabrication of solid-like and core-shell microgels is demonstrated. The chapter ends with the characterization of the GelMA hydrogel, and the GelMA particles.

4.1 GelMA Synthesis and Pre-polymer Preparation

4.1.1 Materials

Chemicals used in synthesis of GelMA hydrogel and generation of GelMA microgels are listed as following:

Gelatin from Porcine Skin Type A (G2500), Methacrylic anhydride (MA), Dulbecco's Phosphate Buffered Saline (DPBS) (D5773), Dialysis membrane (D9527-100FT), Lithium phenyl-2,4,6-trimethylbenzoylphosphinate (LAP), Mineral oil (M841) , MC (4000 cp), Span® 80. All materials were purchased from Sigma-Aldrich.

4.1.2 Synthesis of GelMA

GelMA was synthesized in accordance with Sanchez et al. [103] instruction. Briefly, type A porcine skin gelatin was dissolved in DPBS at 10% (w/v) and stirred at 300 rpm for one hour. During the process, the temperature was kept at 50 ℃. Next, 10 % (v/v) of MA was added dropwise at the rate of 0.5 ml/min to the gelatin solution by a syringe pump under a constant stirring and condition at 55 ℃ and allowed to react for three hours. Then, a 5x volume of DPBS was used to finish the reaction. After that, the mixture was dialyzed against distilled water for one week at 37℃ to remove salts and generated methacrylic acid. They were filtered through a 12-14 kDa cutoff dialysis. By the use of a peristaltic pump (Masterflex), the dialysis water was continuously replaced by distilled water at the flow of 5 ml/min. In the end, the solution was lyophilized through a vacuum freeze dryer for five days to generate a white porous foam and stored at -80 ℃ before use. The Lyophilized GelMA is shown in Figure 4.1. The degree of MA substitution of GelMA is reported previously in Sanchez et.al [103]. GelMA synthesis parameters are reported in Table 4.1.

Figure 4.1 Lyophilized GelMA after freeze drying step

Table 4.1 Synthesis parameters of GelMA

Volume percentage MA (v/v)	GelMA Prepolymer (Mass/volume)
1% (Medium-GelMA)	5%

4.1.3 Pre-Polymer GelMA Solution Preparation

To generate hydrogel (GelMA solution), lyophilized GelMA (Freeze-dried GelMA) was mixed at 5% (w/v) into DPBS containing 0.5% (w/v) of previously dissolved LAP. To protect the solution from environment light, the tube containing the solution prepolymer was wrapped in the aluminum foil. Then the wrapped tube was placed in a water bath at $70^{o}C$ to assure the complete dissolution. Finally, the prepared solution was kept in a refrigerator at $4^{o}C$ for further uses (Figure 4.2).

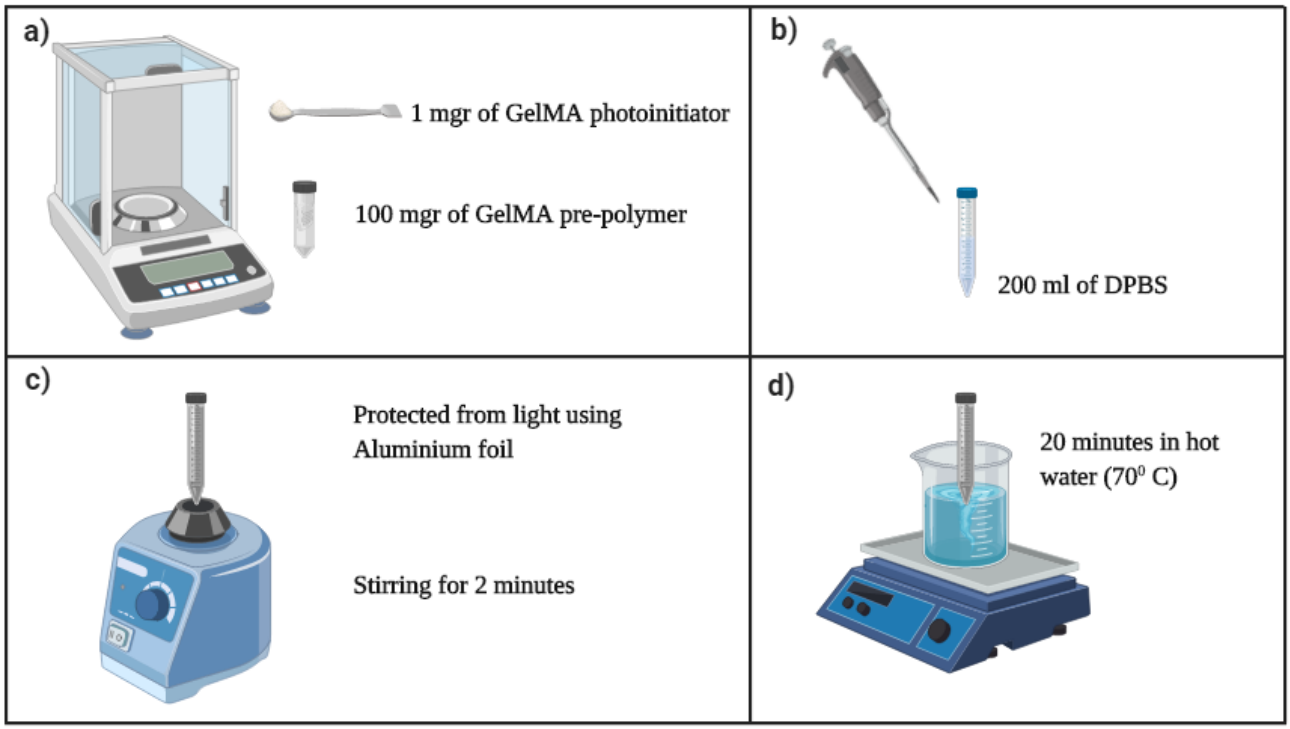

Figure 4.2 GelMA solution preparation. a) The addition of PI to GelMA pre-polymer. b) Addition of DPBS to make the solution. c) Stirring of solution for a better mixture using a stirrer. d) Complete dissolution using a water bath at 70°C.

4.2 Solid-Like and Core-Shell GelMA Microgels Generation

4.2.1 GelMA Microgels Generation Method

The fabricated droplet-based microfluidic device consists of three main functional parts, two flow focusing junctions, and an on-chip photocrosslinking chamber (Figure 4.3). In the case of core-shell GelMA microgels generation, both flow focusing parts were used, while for the solid-like GelMA microgels generation the inner flow focusing was sufficient. For the core-shell generation, it was essential to observe the hydrodynamic flow focusing between GelMA and MC before the droplet generation junction as it prevents the diffusion of MC in GelMA. Therefore, this was the primary step that the fabricated chip had to meet. The sizes of the chip channels were selected in such a way to observe this phenomenon.

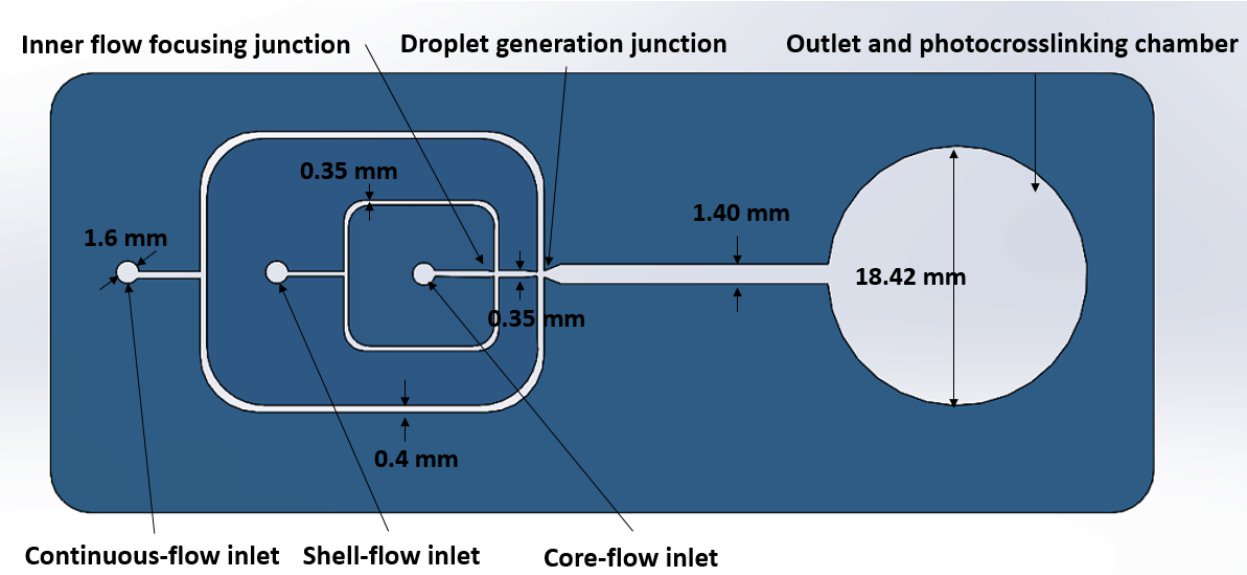

Figure 4.3 Schematic of the droplet-based microfluidic system for core-shell GelMA microgels generation.

UV exposure time is a critical parameter in the fabrication of GelMA microgels, especially for core-shell microgels. In terms of core-shell microgel fabrication, crosslinking should happen immediately to avoid diffusion of core into the shell. Accordingly, either the intensity of the UV light should be increased, or its distance from the crosslinking chamber should be decreased. Additionally, longer exposure time is also a significant parameter to avoid GelMA-water diffusion. Hence, a study on UV light exposure time is required. However, the control and optimization of UV light exposure time was not a purpose of this thesis. In this study, to diminish the crosslinking time the following protocols were conducted: (i) the UV source was attached to the microfluidic device, covering the droplet generation junction, and the whole photocrosslinking chamber. This causes to have the lowest possible distance from the microfluidic device; (ii) a higher UV exposure time was selected.

To generate the solid-like GelMA microgel, the core-flow inlet was closed with sticking a tape and the following solutions were injected by syringe pumps; 1) a GelMA (5% w/v) solution with 0.5% LAP as previously explained in hydrogel preparation was injected into the shell-flow inlet, and 2) mineral oil enriched with 2% span® 80 solution was first placed in desiccator to remove the air bubbles and then injected into the continuous-flow inlet.

To fabricate solid-like microgels with a constant diameter of 130±5 um, the flow rate for each inlet was selected by a trial and error process. After the droplet generation junction, microdroplets

passed through the crosslinking chamber where they were irradiated by a 405 nm wavelength UV flashlight. Two UV exposure time of 6-10 mins and 2-4 mins were considered for two sets of samples and their effect on the crosslinked microgels was investigated.

After UV crosslinking, the generated microgels were collected from the outlet chamber using a micro pipet. The setup was placed on the stage of an inverted optical microscope to monitor the microdroplet generation Figure 4.4. The same procedure was applied for core-shell microgels fabrication except removing the sticked tape of the first inlet. A syringe container was filled with distilled water to be injected into the core-flow inlet.

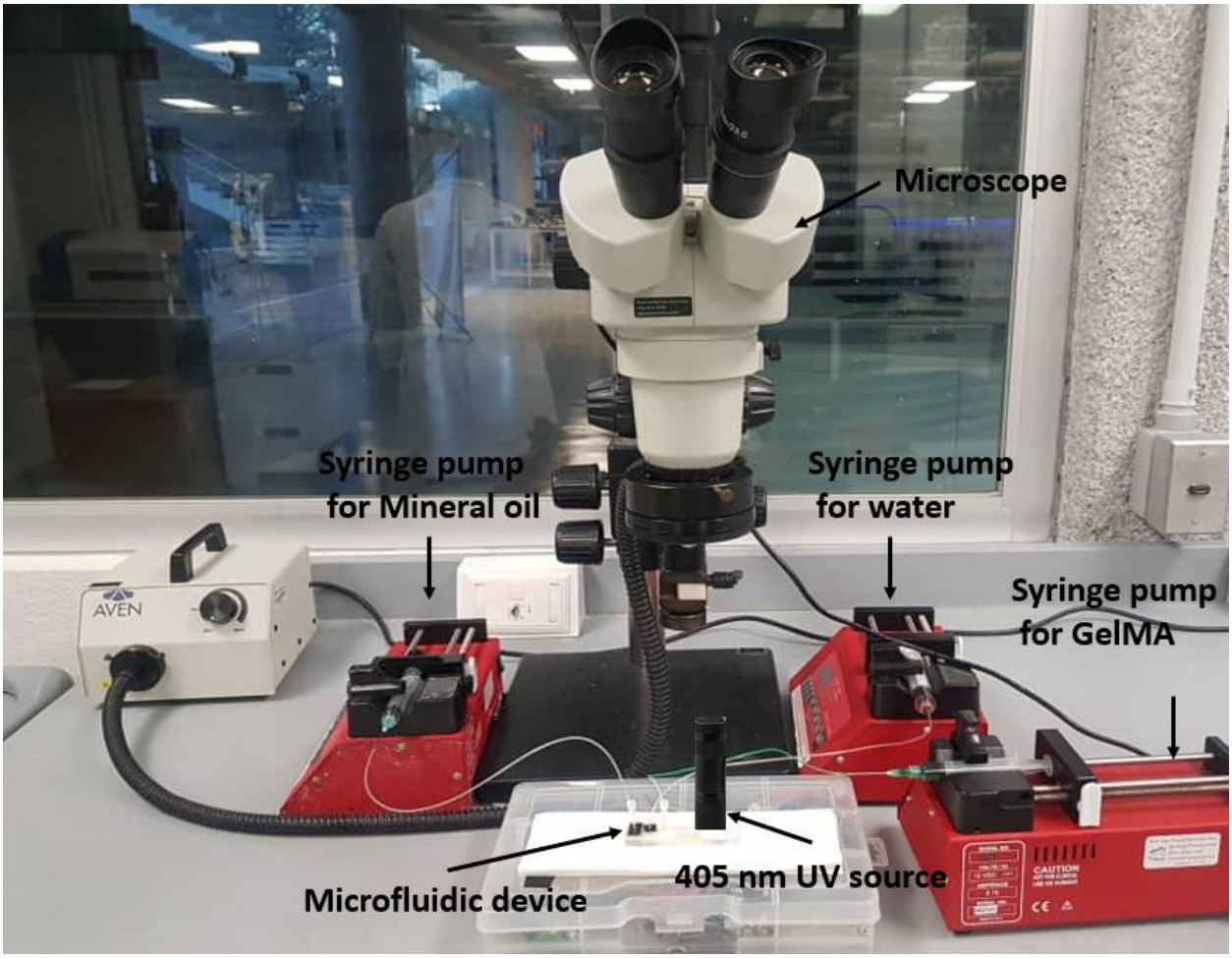

Figure 4.4 Experimental system setup

Using an inverted microscope, the particle size distribution (PSD) of generated GelMA microgels were obtained. The coefficient of variation (CV) was used to measure the dispersion of fabricated

microgels. In detail, the CV (equation 3.1) measures the ratio between the standard deviation (σ) and the average diameter of samples (μ).

$$CV = \frac{\sigma}{\mu} \tag{4.1}$$

4.2.2 Results

The droplet-based microfluidic setup for microgels (solid-like or core-shell) fabrication composed; (i) a microscope to observe the size and the microgels, (ii) the fabricated microfluidic device connected to three syringe pumps, (iii) a UV source which was attached to the device to cover the whole area of the crosslinking chamber. As was explained in the previous part, the fabricated microfluidic chip using the cutter plotting technique was used to generate solid-like and core-shell GelMA microgels. Figure 4.5 represents droplets formation. The Mineral oil as the continuous phase shears the disperse phase (flow focusing of water and GelMA) to break them into core-shell microgels. GelMA is considered to be the shell flow, and water is the core flow.

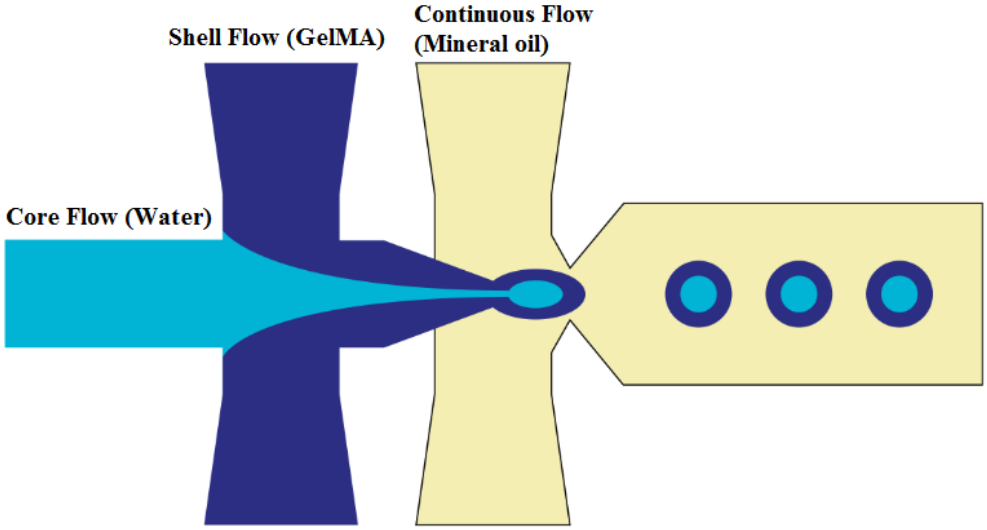

Figure 4.5 Schematic of core-shell GelMA microgels generation. Hydrodynamic flow focusing of GelMA and water occurs in the flow-focusing junction (First junction). The core-shell droplets are fabricated in the second junction.

As it was mentioned in the previous section, the device that was used for GelMA microgels was the same as the one used for core-shell microgels formation, with this difference that the second inlet was being closed with a tape. Figure 4.6 demonstrates the generated GelMA microgels in different sizes, which were varied as the oil's or GelMA flow rate was modifying. Figure 4.7 shows the size adjustability of GelMA microgels by varying GelMA flow rate (error bar: 5% of the microgels' size). In detail, smaller-sized GelMA microgels would be generated by either increasing the oil's or decreasing the GelMA flow rate. For instance, particles with an approximate size of 105±10 um were fabricated when the oil's flow rate and GelMA flow rate were adjusted to 0.001 mL/hr, and 2.009 mL/hr, respectively. Moreover, with the oil's flow rate of 1.28 mL/hr, and the GelMA flow rate of 0.01 mL/hr, GelMA microgels with diameters of 260±10 um were also generated.

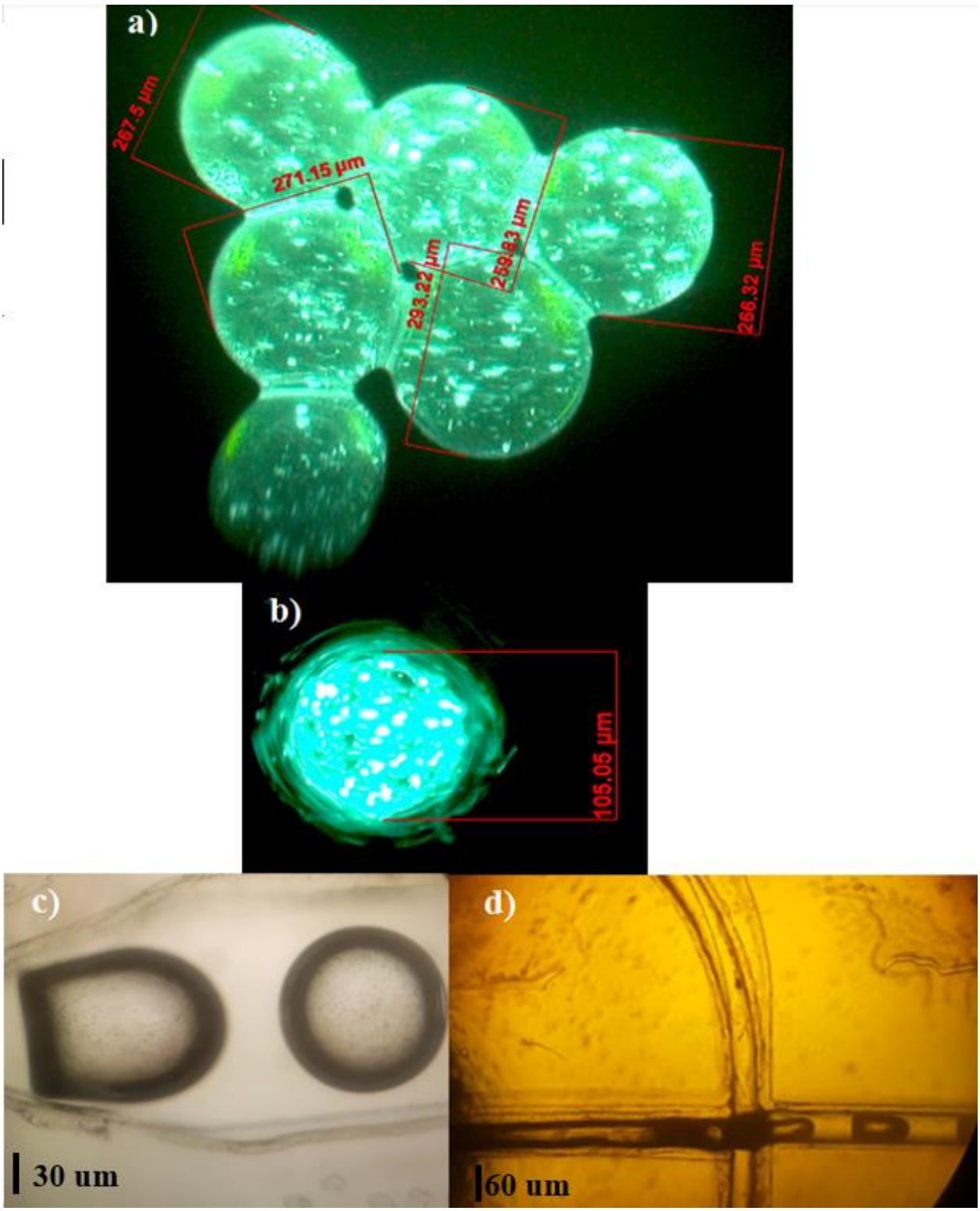

Figure 4.6 The fabricated GelMA microgel. a) GelMA microgels with an average size of 260±10 um. b) The generated GelMA microgel with a size of 105 um. c), and d) GelMA microgels formation in the cross-section micro-channels.

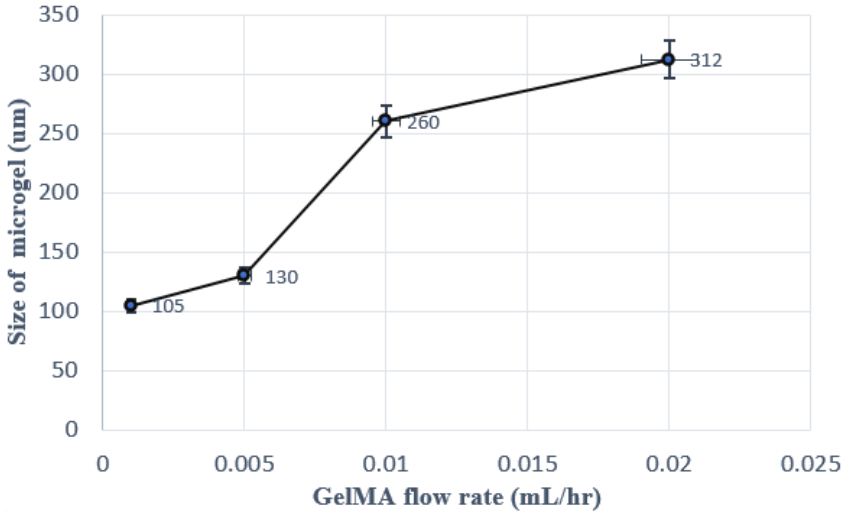

Figure 4.7 Size adjustability of GelMA microgels.

For our experiment, the rates of oil and GelMA flows were assigned to be 1.972 mL/hr, and 0.005 mL/hr, respectively. As the result, microparticles with a diameter of 130±5 um were generated.

As shown in Figure 4.8, the size distribution of the microparticles is homogeneous with an average diameter of 133.43±5 um and a negligible CV of 5.29%.

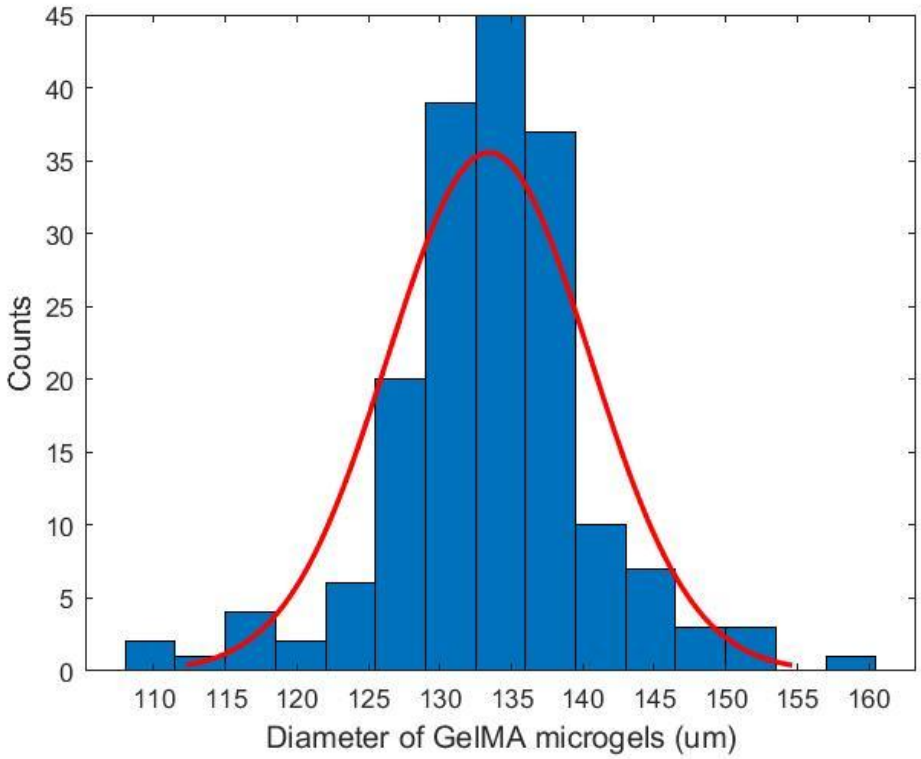

Figure 4.8 Size distribution of GelMA microparticles (average size of133.43 ±5 um for180 samples)

As previously explained, the primary phenomenon that needs to be seen in core-shell GelMA microgels fabrication is the hydrodynamics focusing of GelMA and water before the flows passing through the droplet generation junction.

Hydrodynamic flow focusing happens when several flows are parallel to each other. This phenomenon was observed for GelMA and water using channels with the width and depth of less than 1 mm. Herein, the width and depth of the channels were selected as 300 um and 100 um, respectively. Figure 4.9 shows the hydrodynamic flow focusing of the GelMA-water system with core flow rate (water) of 0.50 mL/hr, and sheath flow rate (GelMA) of 0.05 mL/hr. GelMA was colored by a blue ink and water by a red ink.

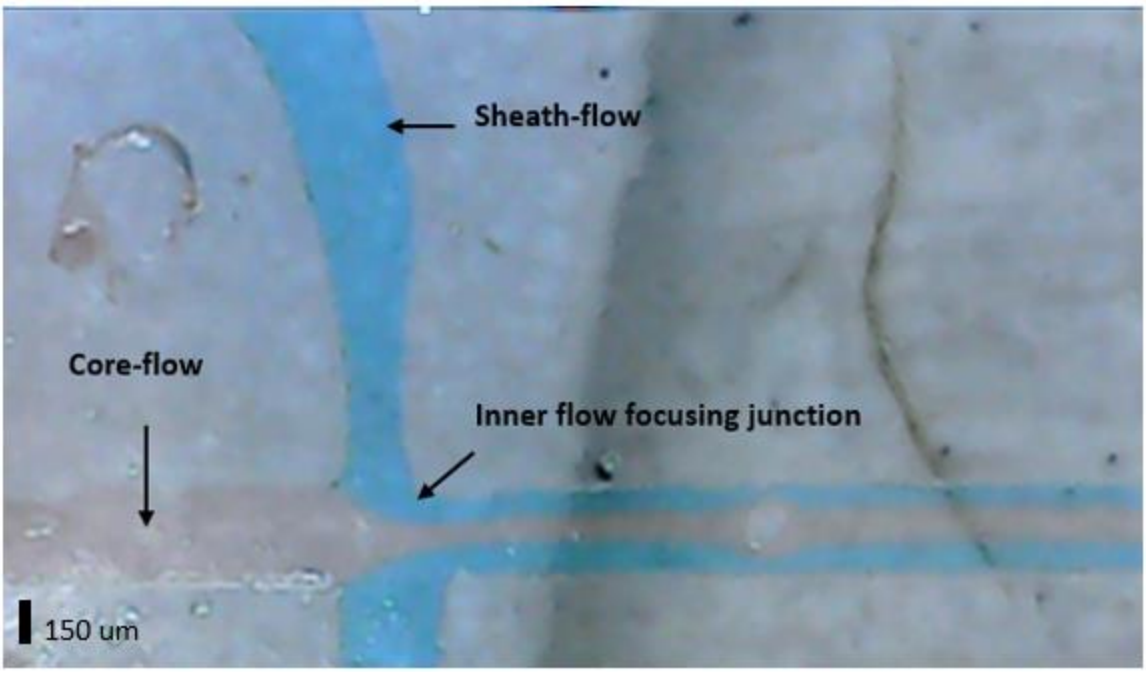

Figure 4.9 Hydrodynamic flow-focusing in the fabricated microfluidic device showing water as the core-flow and GelMA as the sheath-flow.

According to Figure 4.10, after observing the hydrodynamic flow focusing of GelMA and water, at the droplet generation junction, core-shell GelMA microgels were fabricated.

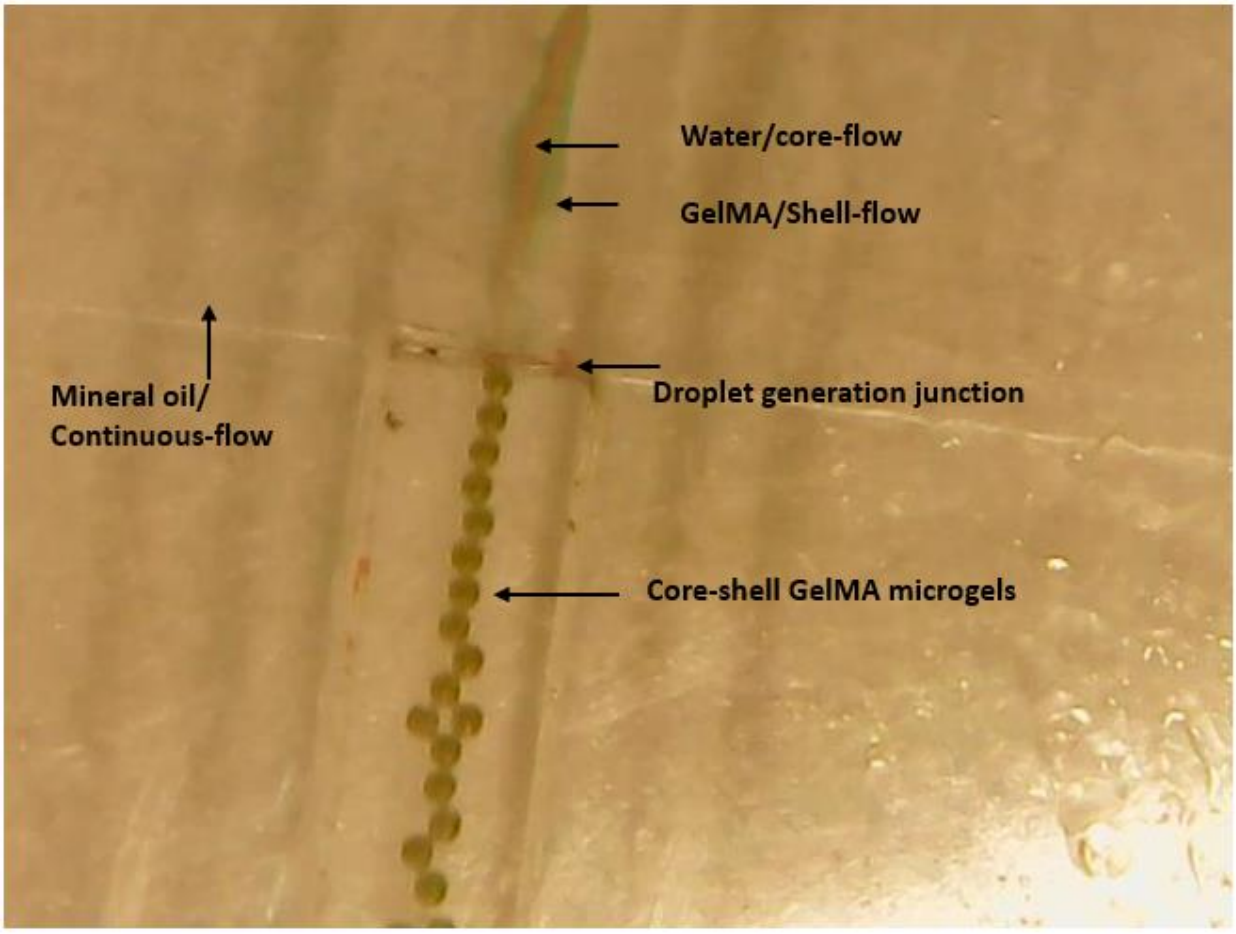

Figure 4.10 Core-shell generation of GelMA microgel in droplet generation junction. The shell is GelMA with a green color, and the core is water with a red color.

Figure 4.11 shows the fabricated core-shell GelMA microgels with 8 minutes and 4 minutes of UV exposure time, respectively. As it is obvious in the figure, the GelMA core-shell microgel, which was exposed to a UV source for a long time of 8 minutes had some fractures. These fractures were not desired for cell culturing application, while the surface of the core-shell microgel with an exposure time of 4 minutes had no cracks (Figure 4.11 b)).

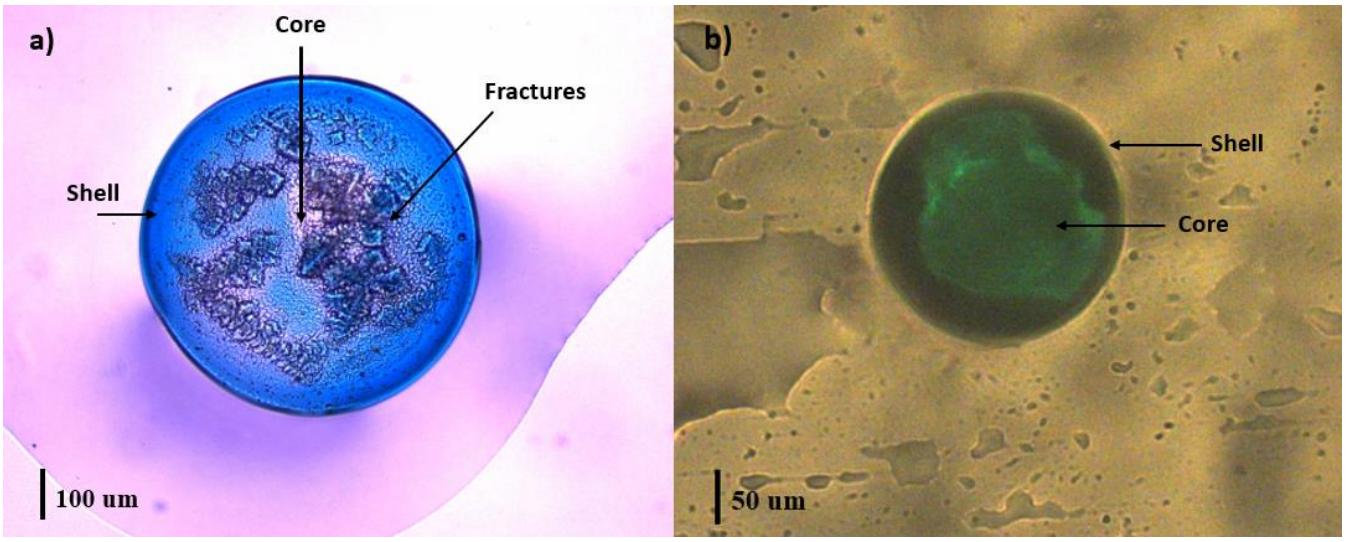

Figure 4.11 The generated core-shell microgels after UV exposure. a) The core-shell GelMA microgel that overexposed to UV (8 mins). Cracks are caused by the overexposure. b) The core-shell microgel with an exposure time of 4 mins.

4.3 GelMA and Microgels Characterization

4.3.1 SEM: Morphology and Porosity

Scanning Electron Microscopy (SEM) implements a focused beam of high-energy electrons to produce a wide range of signals at the surface of solid specimens. The signals acquired from the electron-sample interactions indicate information about the specimen, including the texture (external morphology), crystalline structure, chemical composition, and the orientation of materials composing the sample. Therefore, SEM (ZEISS EVO MA25, Germany) was used to analyze the impacts of the flow rates on the core-shell morphology and structure of GelMA microgels. Additionally, the porosity of GelMA was observed. In doing so, GelMA microgels with a specific shape and volume were soaked in DPBS (pH =7.4) to wash away the un-polymerized components. Next, the fabricated GelMA microgels were centrifuged at 800 rpm for 3 minutes (Centrifuge, TG16-W, Cents) to remove the undesired mineral oil. Finally, the GelMA microgels were freeze dried and coated by gold in a spotter coater. The SEM images of superficial sections were obtained at a 400x magnification. Three images per each sample were analyzed.

Figure 4.12 shows the SEM images of generated microparticles at two different GelMA flow rates of 0.005, and 0.020 mL/hr, while the oil flow rate was kept constant at 1.972 mL/hr. Using ImageJ software, the diameter of the particles with previous flow rates was measured as 134.9, and 312.9 um, respectively. Both samples have the same distinct morphology of spheroid. One more GelMA solid-like microgel with diameter of 189 um is also shown in Figure Appendix D.1. The porosity of the GelMA microgel can be clearly seen in Figure 4.12 a) and Figure Appendix D.1.The average pore size of GelMA microgels prepared using 5% concentration calculated as 23.28±6 um^2 (Using Figure Appendix D.1). The irregularity observed in the shape of Figure 4.12 b) was caused during the centrifugation, detailed in SEM sample preparation Section 3.9.1.

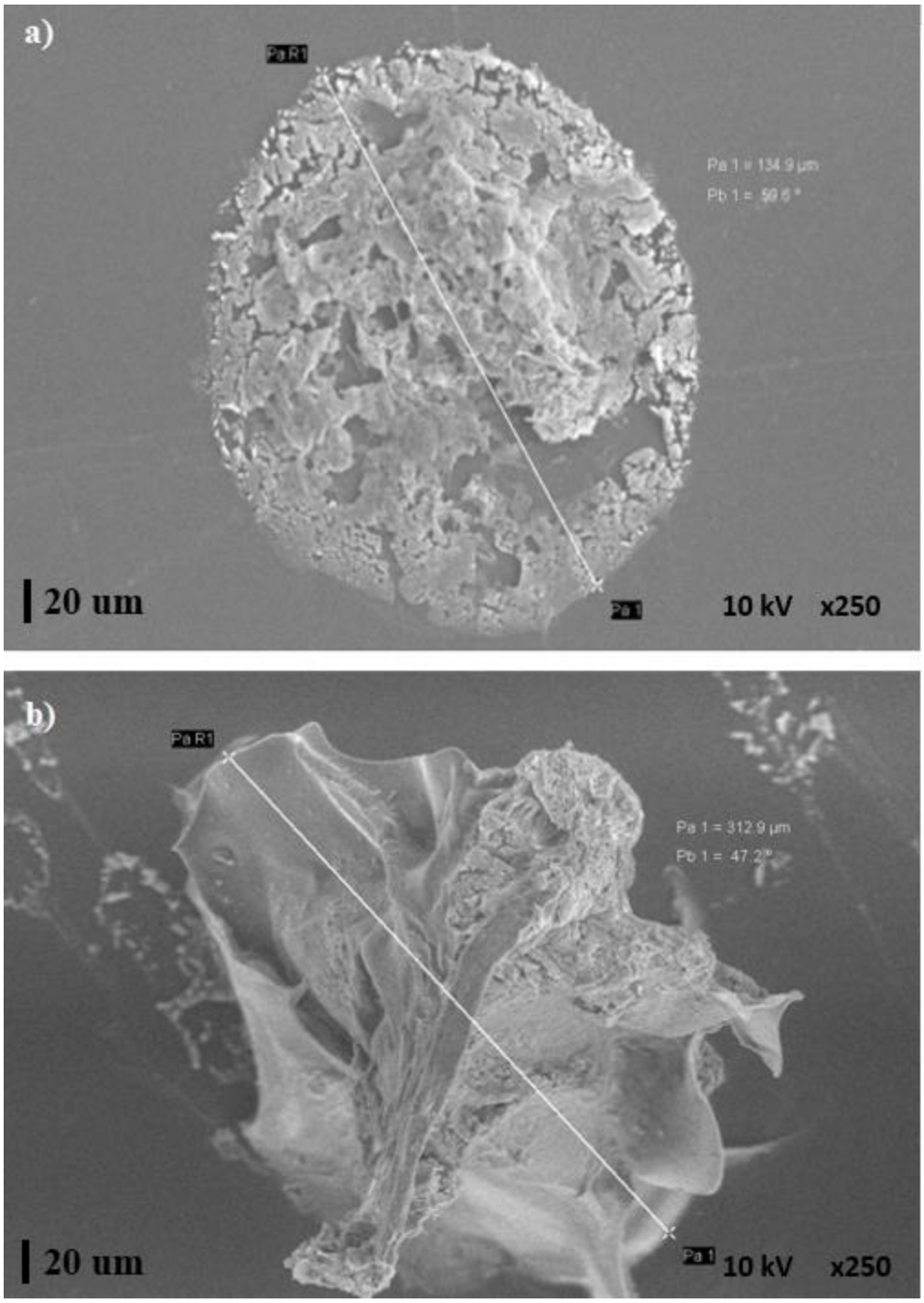

Figure 4.12 Morphological characterization of GelMA microgels using SEM. a) SEM image of GelMA microgel generated at the GelMA flow rate of 0.006 mL/hr with a constant oil flow rate of 2 mm/hr. b) SEM image of the GelMA microgel generated at GelMA flow rate of 0.02 mL/hr. with a constant oil flow rate of 2 mL/hr.

4.3.2 FTIR: Composition

In this study, Fourier Transform Infrared Spectroscopy (FTIR) was performed to evaluate whether the synthesis and crosslinking of GelMA pre-polymer were successful. To this mean, 20 µl of GelMA prepolymer was placed between two thin plastic shields and dispersed to assure the formation of a very thin layer solution, and then exposed to UV for 2-4 minutes. Three samples were prepared with the same protocol. The samples spectra were obtained using FT-IR Nicolet^{TM} iS^{TM} before and after UV exposure. The study was carried out within the wavelength range of 500 to 4000 cm^{-1} with a resolution of 1 cm^{-1}.

FTIR spectrum of crosslinked GelMA and uncrosslinked GelMA is shown in Figure 4.13.
The relevant bands for GelMA hydrogel were identified at 1647, 3402, 2919 cm^{-1} related to C=O stretching of amide I, -OH stretching, and C-H stretching, respectively.
Since the added volume of MA is less than 5% (1% in our synthesis), methacrylate substituent groups incorporated into GelMA were not detectable [104]. Therefore, the difference between crosslinked GelMA and uncrosslinked GelMA could not be identified using FTIR.

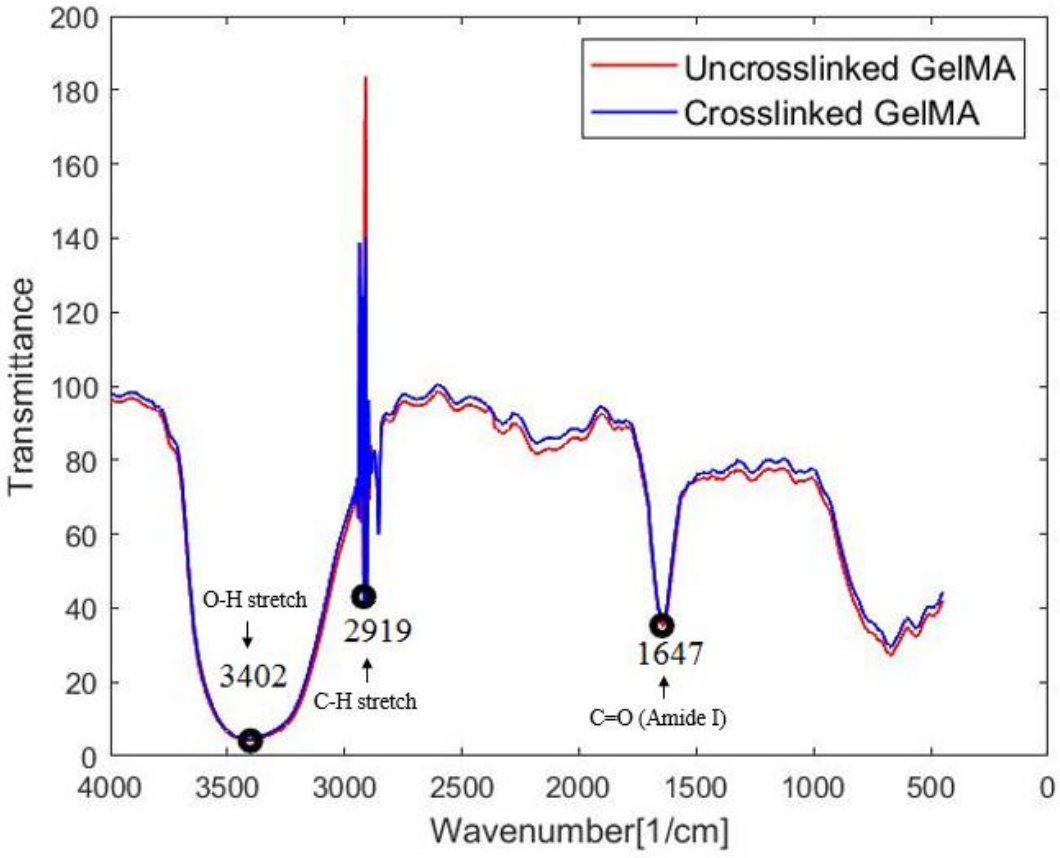

Figure 4.13 FTIR of crosslinked and uncrosslinked GelMA

Chapter 5 Computational Analysis of Microgels Deformation

This chapter starts by a brief description of constitutive material models followed by a presentation of the computational model evaluating particles passing through a confinement channel.
Two models of particle indentation and CFD have been presented. The simulation design and methods are first discussed and the results are explained next.

5.1 Theory of Constitutive Models

A viscoelastic material can be defined as a material with both behaviors of elastic and viscose while withstanding deformation.

The Maxwell model can be used to represent a viscoelastic material [105]. This model consists of a spring and a dashpot, which are connected in series. Table 5.1 shows the equations and the models, in which stress and strain are represented as σ and ε, respectively. It expressed the formulas for a single dashpot and spring, where E1 and η_1 are elastic modulus, and viscoelastic modulus, respectively (equation 5.1 and 5.2). In the Maxwell model, the strain of the total system would be the summation of all component strains. The stress of the total system would be equal to the stress of dashpot, equal to stress of spring.

Table 5.1 Mechanical model of a single dashpot and spring.

Model	Equations
	5.1) $\sigma_s = E_1 \varepsilon$
 Dashpot	5.2) $\sigma_d = \eta_1 \dot{\varepsilon}$

Prony series is the generalized Maxwell model, which is defined to represent the viscoelastic behavior of the materials, i.e. polymers, living tissue, and cells. In the generalized Maxwell model, a parallel series of an arrangement of a spring and a dashpot would be considered. The benefit of this model over than a simple Maxwell model is considering a distribution of relaxation times and not a single value.

In a one-dimensional relaxation curve, the induced stress in the response of the imposed strain would decay over time. It finally reduces to zero for uncrosslinked polymer, or to a constant value for the polymerized one [106].

The shear modulus G(t) is defined by n-term

Prony series expansion as [107]:

$$G(t) = G_0 + \sum_{i=1}^{n} g_i \, e^{\frac{-t}{\tau_i}} \tag{5.3}$$

Where G_0 is the instantaneous shear modulus, g_i is the relaxation modulus, and τ is the relaxation time in each iteration.

Another constitutive model is hyperelastic model, which is used to describe rubber-like materials that respond elastically to large deformations [108]. One theory used widely for explaining the

hyperelasticity is called Neo-Hookean, with the strain energy density function (U) given as follows:

$$U = C_{10}(I_1 - 3) + \frac{1}{D_1}(J^{el} - 1)^2 \tag{5.4}$$

Where I_1 is the first strain invariant, J^{el} is determinant of deformation gradient and C_{10} and D_1 are the material parameters. Both depend on temperature and can be expressed as a function of the shear modulus (G) and bulk modulus (κ) shown in equations below:

$$C_{10} = \frac{G}{2} \tag{5.5}$$

$$D_1 = \frac{2}{\kappa} \tag{5.6}$$

where μ, and κ are the parameters related to Young's modulus (E) and the Poisson ratio (v) for small deformation in accordance with equations below:

$$\mu = \frac{E}{2(1+v)} \tag{5.7}$$

$$\kappa = \frac{E}{3(1-2v)} \tag{5.8}$$

5.2 Simulation Method

5.2.1 Microindentation of the Particles

The two-dimensional axisymmetric FEM analysis of the indentation of the aforementioned specimens was built in ABAQUS. ABAQUS is a finite element analysis simulation product that suits for the modeling and analysis of mechanical components. Considering a symmetrical condition, only half of the whole indentation geometry was modeled. Both the boundary conditions and the designed model of a core-shell are shown in Figure 5.1. The reference point of the bottom plate was selected as Encastre that constrains all the available degree of freedom. The nodes lying on the Y-axis are fixed in Y to represent the symmetry conditions. The top plate is allowed in Y-direction. The reference point of the top plate is assigned for applying the pre-defined

displacements and speeds. The same boundary conditions were assigned for the indentation of other particles.

For the indenter tip, the recommended indenters for a soft and biological particle are dull indenters (such as spherical and flat-ended) rather than sharp indenters (such as Berkovich and Vickers) to avoid penetration the samples [103]. Hence, a flat-ended indenter was selected and modeled as an analytical rigid body. The contact between the samples and the indenter was speculated as tangential frictionless and normal hard contact, and no-slip was set for the bottom surface. Sigle-cell, alginate microgel, the shell of core-shell alginate microgel, and both cell and alginate in alginate containing single-cell were modeled with CAX4RH elements and the core of alginate containing single-cell was modeled with FAX2 elements (2-node linear axisymmetric hydrostatic fluid). The CAX4RH elements are 4-node bilinear axisymmetric quadrilateral, hybrid, constant pressure, reduces integration, hourglass. . For all particles the mesh type was selected as Quad-dominated. The top and bottom plates have 0.02 mm height and 0.08 mm length for the indentation of single cells, and the rest have 0.306, 0.045 mm height, and length, respectively.

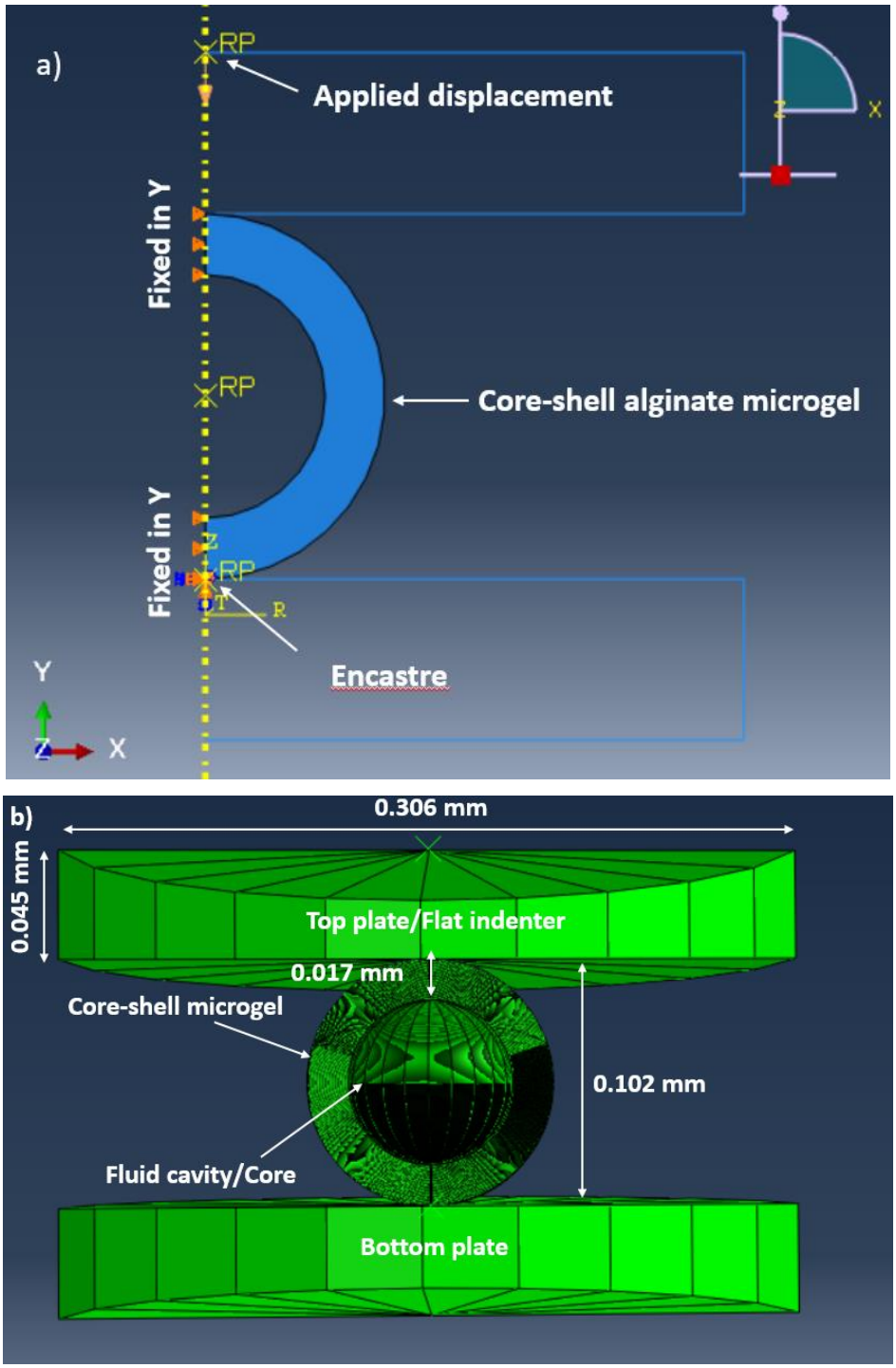

Figure 5.1 Design and Boundary conditions of the core-shell microgel indentation. a) The assigned boundary conditions on the core-shell microgel and the plates. b) The half 3D model of core-shell indentation with its dimensions.

All material parameters for each model were determined from the reported references in Table 5.2.

We could not find the viscoelastic parameters of GelMA microgels in previously reported literature. Hence, we used the available data for alginate hydrogel which is applicable in 3D cell culturing like GelMA. It is worth mentioning that we can change the model inputs once we get the experimental data for GelMA microstructures. In the material step of the first simulation (indentation), the selection of proper constitutive models is a potent factor in the accuracy of simulation results. As been reviewed in Section 2.3, a variety of constitutive models, such as hyperelastic, poroelastic, and viscoelastic have been used in the study of soft particles mechanical properties. Herein, for the characterization of the aforementioned specimens, the viscoelastic model was selected. The viscoelastic model was conducted using Prony series and using the VISCO procedure of ABAQUS.

Table 5.2 Material parameters of the samples

Specimen	**Size (um)**	**Elasticity G-instantaneous (MPa)**	**Viscoelastic Maxwell parameters**			**Poisson's ratio**	**References**
			$G_{Longterm}$ (MPa)	**G1 (MPa)**	**Tau (MPa)**		
Osteocytes cells	10	257e-6	5e-5	207e-6	0.45	0.31	[74], [109]
Alginate microgels and core-shells	Total size: 102 Shell thickness: 0.017	0.49	0.45 MPa		0.013	0.31	[110]
			0.45 MPa	0.27 MPa	0.085		

One possible indentation experimental design can be based on a controlled depth technique (displacement-control) which is more proper for soft particles [66]. This technique encompassed the two steps of the ramp and hold. First, the indentation took place and samples were compressed to a predefined indentation depth by an indenter with a specific velocity. Then samples were held for an exact amount of time to let the specimens relax. Finally, the applied force during these two

steps and the contact area were measured against the deformation rate. From the obtained data, force vs. displacement, stress vs. strain, contact area vs. strain, and stress curves were plotted.
This model was analyzed using different indentation velocity values (load rates) and together with other parameters of controlled depth technique are given in Table 5.3. The core and shell in core-shell alginate microgel were modeled as fluid cavity with a zero pressure, water density of 997 kg/m^3, and viscoelastic material with the same parameters given for alginate in alginate microgels (Table 5.2).
The elastic modulus of particles were extracted from the power-law region of the force-indentation (displacement) or stress/strain plots, and by fitting Hertz contact mechanics theory for spherical elastic solid given in equation (5.9) [111]:

$$F = \frac{4}{3}\left(\frac{E}{1-\upsilon^2}\right) R^{1/2} h^{3/2} \tag{5.9}$$

Where R is the radius of microgel, h is the indentation depth that varies along time, and υ is the Poisson's ratio of alginate microgel which is considered to be 0.3.

Table 5.3 Controlling parameters of indentation simulation

Specimen	Size (mm)	indentation depth (mm)	Load rate (mm/s)
Alginate microgel	0.102	30%×0.102=0.0306	
		40%×0.102=0.0408	
Core-shell alginate microgel	0.102	30%×0.102=0.0306	0.05 0.1 0.5 1 10
		40%×0.102=0.0408	
Osteocytes cell	0.01	30%×0.01=0.003	
		40%×0.01=0.004	
Alginate microgel containing single-cell	0.01	30%×0.01=0.003	
		40%×0.01=0.004	

5.2.2 Computational Fluid Dynamics

Concerning the effect of different constriction channels, a CFD analysis was established using the CFD module of ABAQUS to perform the laminar fluid simulation. This CFD model was created using two different geometries. The geometry and dimensions are represented in Figure 5.2.

The fluid was considered to be mineral oil with the density and dynamic viscosity of 9.59011e-10 tonne/mm^3, and 1.05e-7 MPa.s [112], respectively. The flow enters at the velocity of 0.5 mm/s, and discharges into the atmosphere with a gauge pressure of 0. The no-slip condition was selected on the walls. For all channels the mesh type was selected as Tet (Tetrahedral). Velocity contours would be extracted as a result.

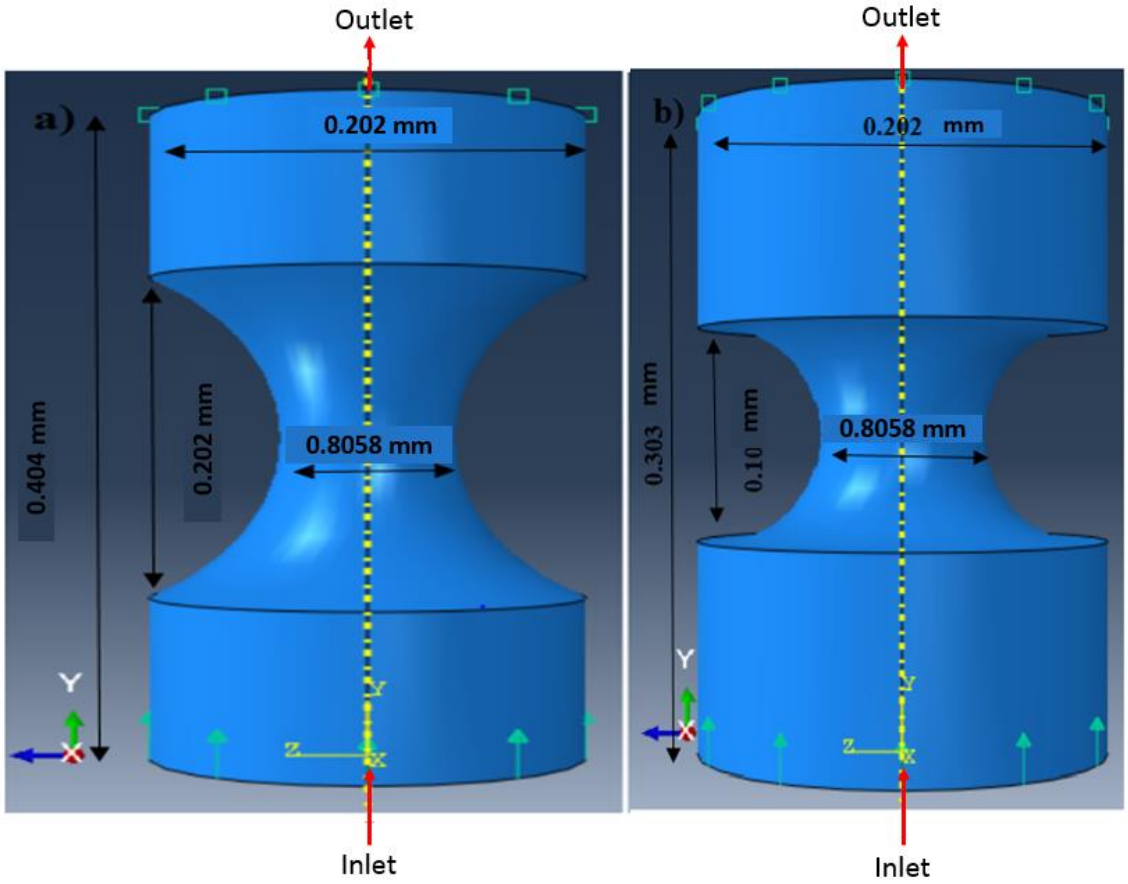

Figure 5.2 Constriction channel geometries designed for 21% deformation of GelMA microgel used in CFD.

The governing equation in this section is Navier Stokes equation for momentum conservation (equation 4.10). It was assumed to have a steady-state process for a homogenous` incompressible (equation 4.9) and Newtonian fluid [113].

$$\frac{\partial \rho}{\partial t} + \nabla.(\rho\, v) = 0 \quad \text{incompresible flows} \tag{5.9}$$

Where ρ is the fluid density, v is the fluid velocity vector, ∇ is the gradient operator

$$\rho\left(\frac{\partial v}{\partial t} + v.\nabla v\right) = -\nabla.P + \mu\nabla^2 v + \rho g \quad (5.10)$$

Where P is the fluid pressure, μ is the kinematic viscosity, g is gravitational constant, and ∇^2 is the Laplacian operator.

5.2.3 Grid Indecency Analysis of FEM Model

Mesh convergence was carried out for each simulation (indentation with different particles, and CFD) to make sure the mesh size would not have an impact on the overall results. To evaluate the convergence-based mesh refinement behavior of the Alginate microgel indentation, different element sizes of 0.0011, 0.009, 0.00055, 0.005 mm were generated. The corresponding elements numbers were 4109, 7795, 16506, 19761, respectively. Similarly, the same study was applied for other simulations with different element sizes indicated in Table 5.2. All the analyses were conducted for the viscoelastic model with the Prony series constitutive model (material and geometrical parameters were reported previously in Table 5.4).

The comparison between force against time of each analysis was conducted to find the optimum accurate mesh refinement.

Table 5.4 Element size analysis

Specimen	Mesh size	Number of generated nodes
Alginate microgel	0.0011	4109
	0.0009	7795
	0.00055	16506
	0.0005	19761
Osteocytes cells	0.00011	3756
	0.000055	15161
	0.00005	18379
	0.00004	28807
	0.00003	50987
	0.0000275	60198
Core-shell microgel	0.0011	1800
	0.00055	7533
	0.0005	9044
	0.0004	13986
	0.0003	25365
	0.00025	36244
Alginate microgel containing single-cell	Cell:0.0005 Alginate: 0.0005	Cell: 175 Alginate: 19761
	Cell:0.00035 Alginate: 0.00035	Cell: 386 Alginate: 40858
	Cell:0.0003 Alginate: 0.0003	Cell: 508 Alginate: 55182

5.2.4 Model Validation

In order to validate the model, this simulation method was applied to the model presented by Nguyen et al. [110] who used the FEM for the indentation of alginate beads. A two-dimensional axisymmetric analysis was performed. An alginate bead with a diameter of 102 um was compressed between two rigid plates with the speed of 500 um/s and then held for 2 secs. The Prony series with the parameters given in Table 3.3 was used. These parameters were also used for the material definition of alginate microgels reported in this thesis. The curve of force-

indentation depth was generated with this thesis simulation program and the result was compared with the ones of the article (Nguyen et al. [110]).

5.3 Results

5.3.1 Microindentation of the Particles

The force-relaxation (force-time) curve generated during the indentation process was obtained for all the particles at different indentation velocities of 0.05, 0.1, 0.5, 1, 10 mm/s. Figure 5.3 illustrates the force against the time plot of the aforementioned particles at both 30% and 40% of strain rates, while maintaining an indentation velocity of 1 mm/s. In both 30% and 40% of indentation depths, the reaction force of the alginate microgel is more than the microgel containing single-cell, and this is more than the core-shell microgel at any time. The least active-force belongs to the single-cell. Similarly, this regulation was also found in the equilibrium force. The equilibrium state of alginate microgel, alginate containing single-cell, core-shell alginate, and cell happened at 1.8e-4, 1e-4, 0.5e-4, and 2.8e-4 N, respectively. A similar trend was also observed for the other indentation speeds at either 30% or 40 % of strain rate, the two force-relaxation curves with the lowest approached velocity equal to 0.05mm/s at each strain rate are shown in Figure Appendix B.1.

It should be noted that for the indentation of alginate containing single-cell, 30%, and 40% of the cell size was the reference, not the total alginate microgel's size (102 um). Therefore, the indentation depth of the alginate containing single-cell selected in such a way to assure the consequent 30% and 40% indentation of the encapsulated cell. By trial and error, the required microgel deformation was obtained around 24% and 20.92% of the alginate microgel's size (102 um) for 40% and 30% cell deformations, respectively.

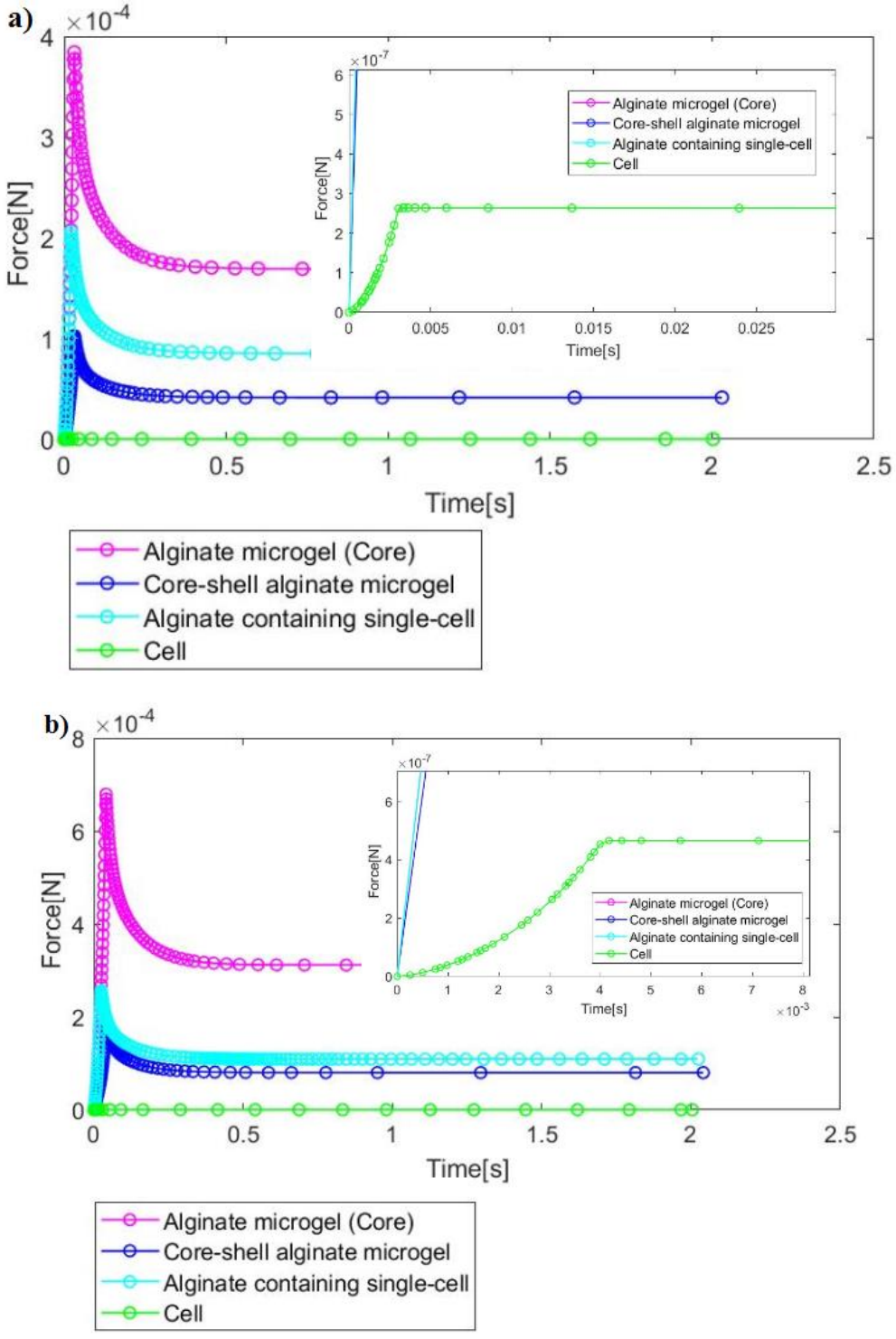

Figure 5.3 Force-relaxation curves generated from FEM deeming the indentation velocity equal to 1 mm/s. a) At 30% strain. A maximum reaction force of approximately 3.84e-4 N was obtained for alginate and a minimum of 2.63e-7 N for single-cell. b) At 40% strain. A maximum reaction force of approximately 6.79e-4 N was obtained for alginate and a minimum of 4.66e-7 N for single-cell.

Figure 5.4 represents the variation of maximum reaction force against the relaxation time of all particles at 30% and 40% of deformation.. The curves demonstrates the following information:

1. A smaller indentation depth induced lower reaction force.
2. Regardless of the particle type, maximum-force decreased as a higher relaxation time (lower indentation velocity) is considered for the indentation test. According to Neumann et al. [114], higher indentation velocities/lower relaxation time results in a higher resistance of the sample material in contact with the indenter which can describe the greater generated force while lowering the relaxation time.
3. At each point, the variation of maximum-force versus relaxation time of the alginate microgel at 30% of strain rate was approximately three times and two times more than the core-shells, and microgel containing single-cell, respectively.
4. The difference between the maximum force in core-shells and microgels containing single-cell is found around 0.1 mN in 30 % at each point, and this value rises to 4 mN for 40% of strain rate.

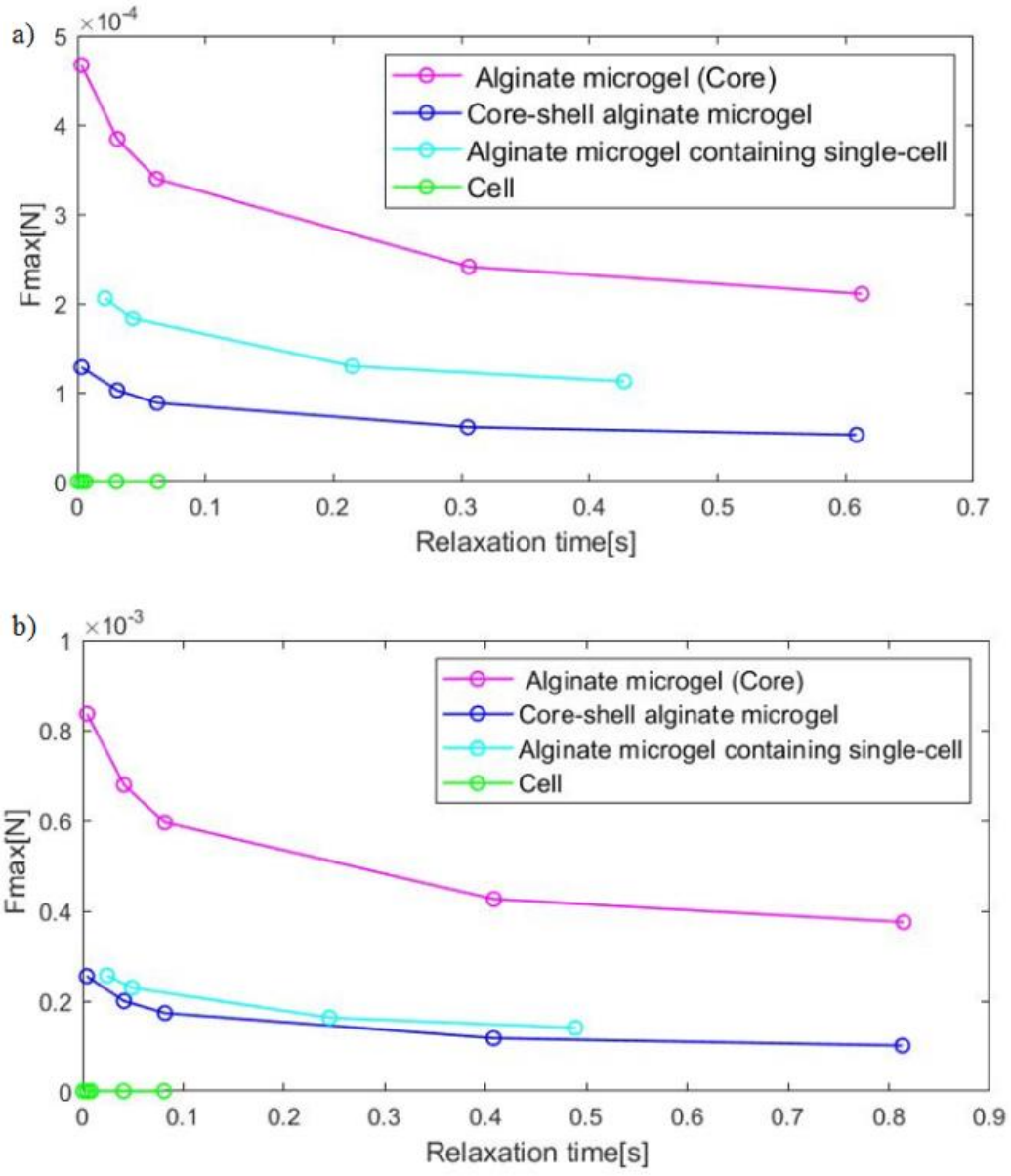

Figure 5.4 Maximum-force vs. Relaxation time for different approached velocities of 0.05, 0.1, 0.5, 1, 10 mm/s. a) At 30% strain. By increasing the relaxation time (decreasing the indentation velocity), Fmax would decrease dramatically, from 4.8e-4 to 2.2e-4 N in the case of alginate. Fmax is higher for alginate microgel at any relaxation time. b) At 40% strain. Fmax would decrease dramatically, from 0.82e-3 to 0.4e-3 N in the case of alginate. Comparing a) and b), Fmax was obtained higher for 40% strain than 30% regardless of particles.

Additionally, the contact area between each particle's surface and the flat-ended indenter was investigated and shown in Figure 5.5. For each particle, at 40% strain, higher contact areas were obtained compared to 30%. Nonetheless, this difference is more noticeable in solid-like and core-shell alginate, around 52% and 65%, respectively. Among all the samples, in both strain rates, the contact area between alginate microgel and indenter is the highest. For instance, at 30% strain, this value is almost 34%, 55%, 99% more than core-shell, alginate- alginate microgel containing single-cell, and single-cell, respectively. It is worth mentioning that there are two contact areas for alginate microgel containing single-cell, one between alginate surface and the top plate, referred to as" alginate-alginate microgel containing single-cell" and one between cell surface an alginate inner surface, " Cell- alginate microgel containing single-cell".

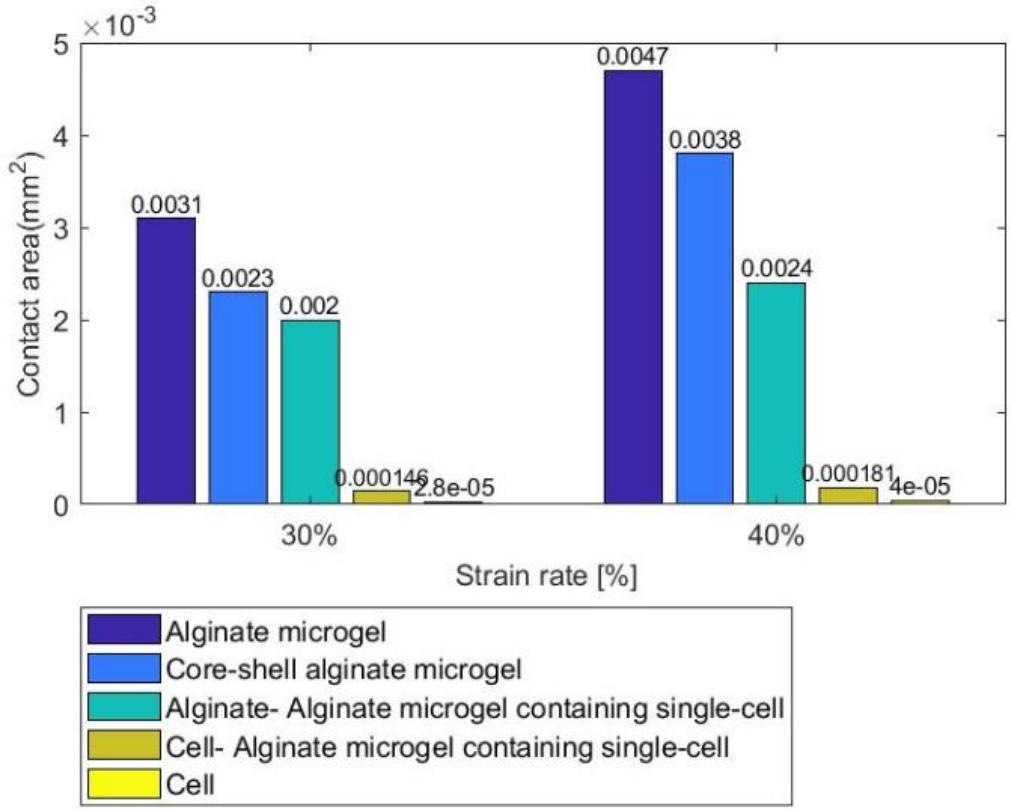

Figure 5.5 Contact area-strain rate bar plot for two indentation depths of 30% and 40%. The contact area of the 40% strain is more than it is in 30% for each particle. The contact area is related to the maximum indentation depth, and the type of the material. This is independent of the velocity rate.

Von Mises stress is a metric to determine whether the structure would yield or fracture. The areas at the risk of yielding can be determined using this method. Figure 5.6 represents the von Mises stress contour of the whole model for each particle at an indentation speed of 0.5 mm/s for 30% strain. The red color represents the high-risk area.

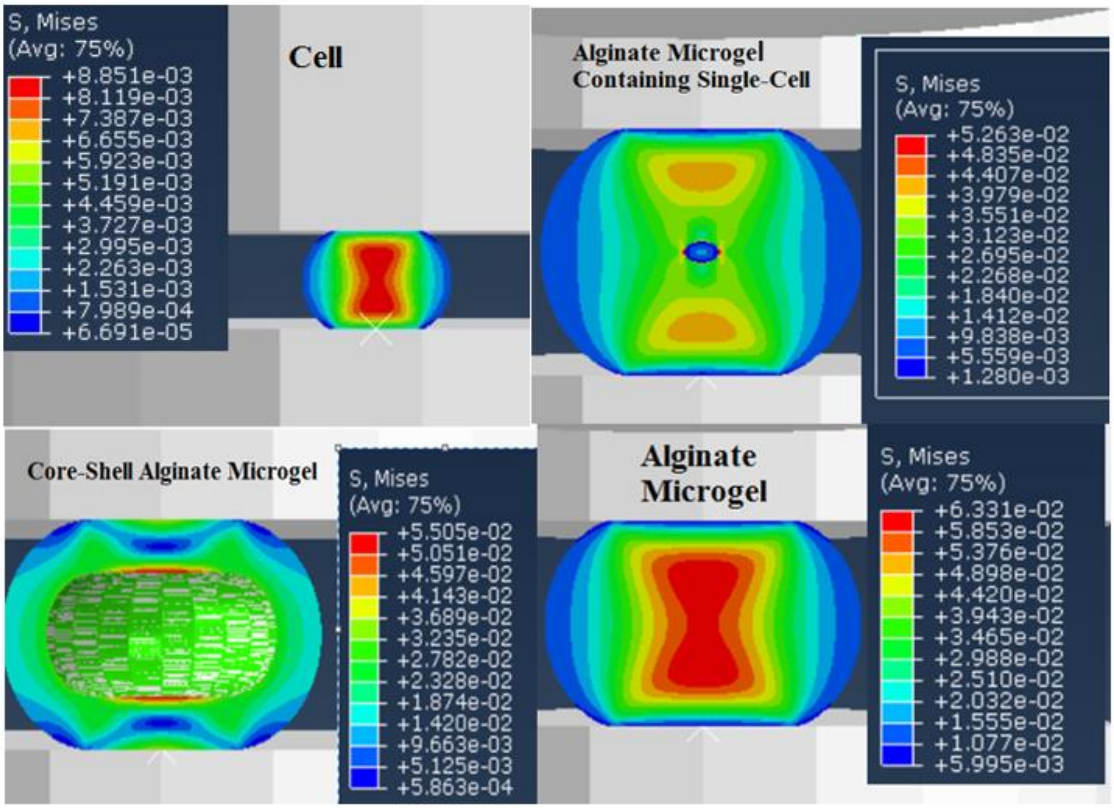

Figure 5.6 Von Mises stress of different microgels. The red color shows relatively higher von Mises stress.

The maximum von Mises stress trended to increase when the particles were indented to their maximum indentation depth. The highest value of maximum von Mises stress on the top node of each particle was found for core-shells shown in Figure 5.7. One possible way to explain the striking maximum von Mises stress of core-shells can be the more rigidification of the material near the contact zone of core-shell model than solid-like microgel. This would prevent the structure to undergo deformation during the applied force [77]. Moreover, the results show the maximum von Mises stress increases while increasing the indentation rate. Herein, this increment was higher for alginate microgel (24%) and core-shell microgel (12%), and slightly lower for alginate

microgel containing single-cell (7%) and single-cell (almost zero) going from 0.05 to 0.1 mm/s. The maximum von Mises stress on the cell inside the alginate microgel is reported here and not the alginate part.

When we use core-shells to encapsulate single cells, a less strain rate should be applied as its von Mises stress for the same deformation and speed is the highest among all the particles. This means that it is more probable for a core-shell to pass its yield and rapture point.

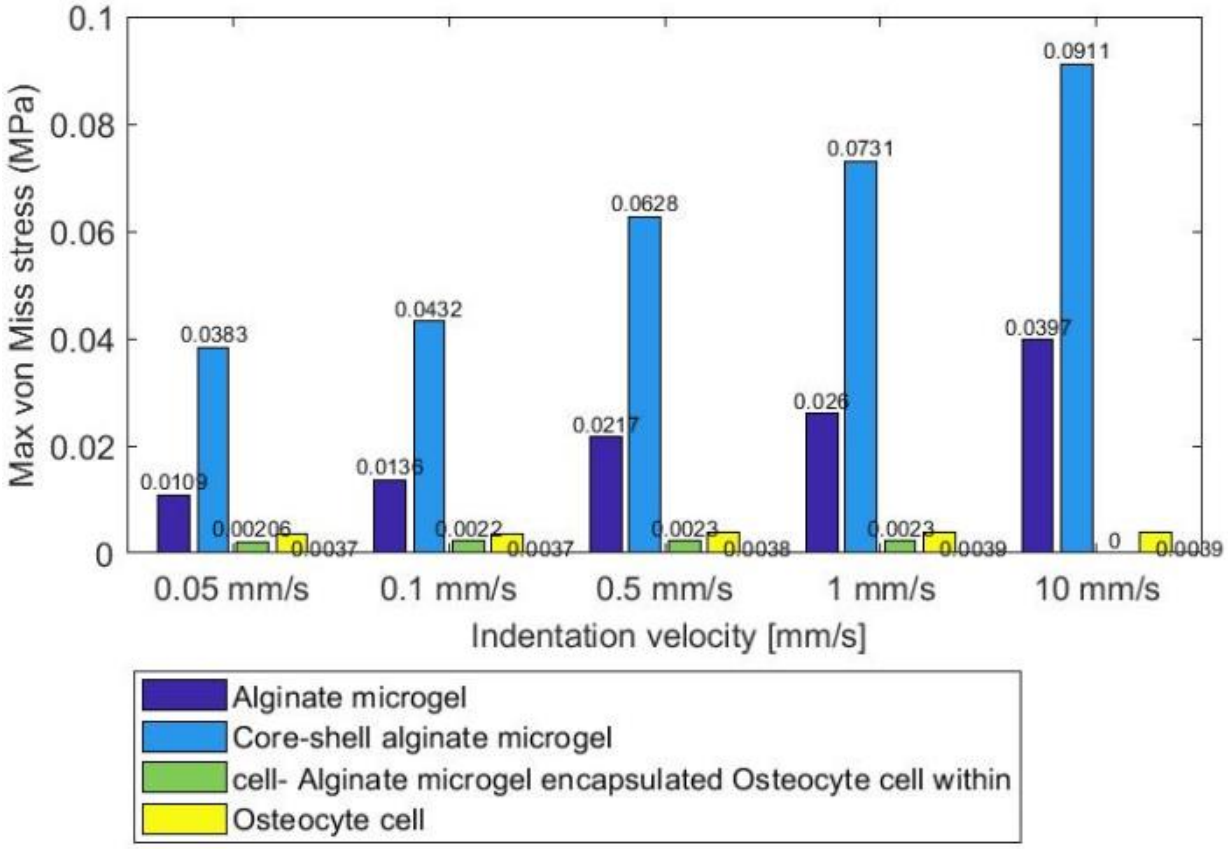

Figure 5.7 Max von Mises stress- indentation velocities at 30% strain. The max von Mises stress increases as higher approached velocity was selected. The highest max von Mises stress in each indentation velocity has happened for core-shell alginate microgel.

Figure 5.8 represents stress-strain curve of alginate containing single-cell and core-shell alginate microgels at different indentation velocities at 30% strain. As it is conspicuous, the reaction stress increases with indentation speed changing from 0.5 to 10 mm/s (0.5 to 1 mm/s for alginate containing single-cell) under the same indentation depth. That equally means a higher

indentation force is required to deform the samples for the same penetration depth. This trend is repeated for single-cell, and alginate microgel at the same strain rate (30%) (Figure Appendix B.2).

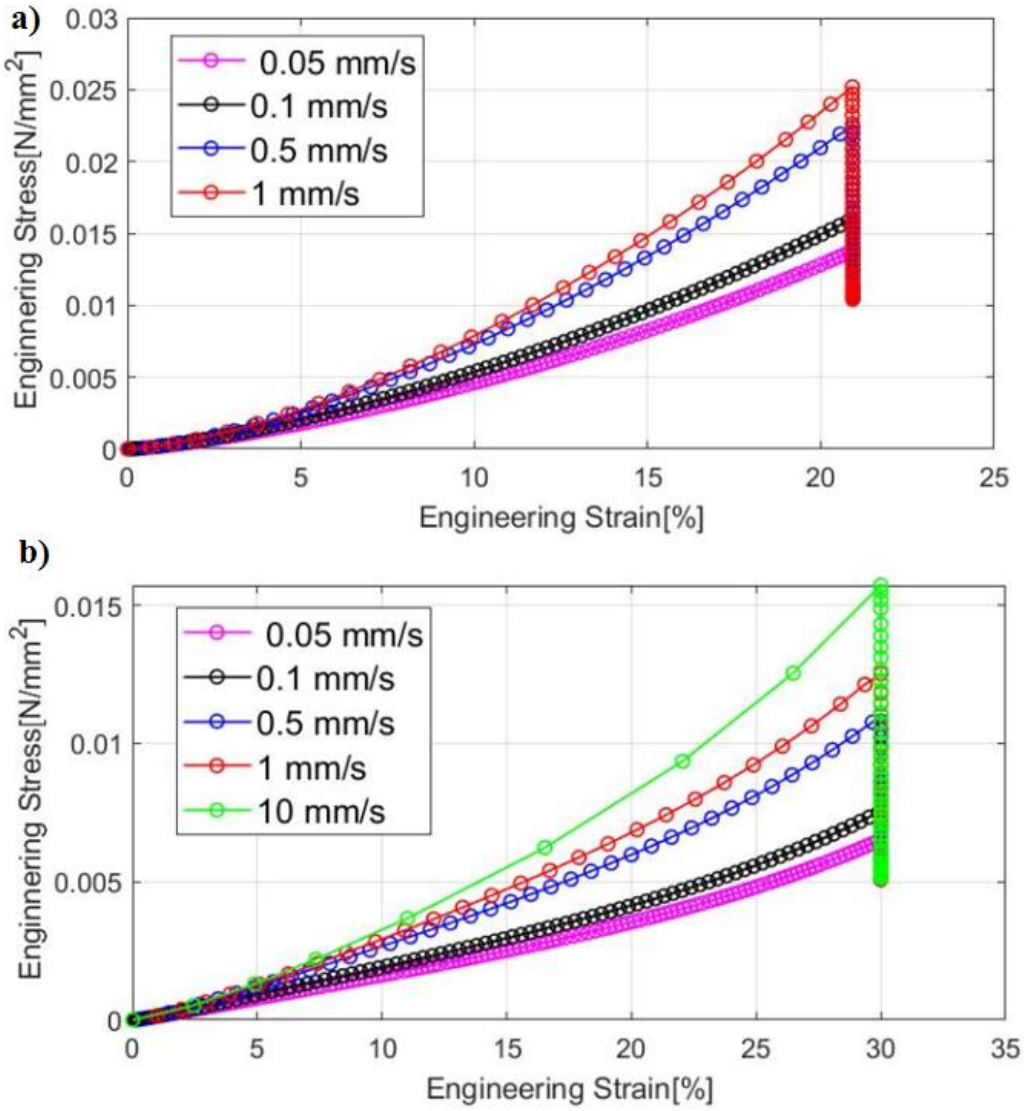

Figure 5.8 Stress-strain curve at different indentation velocities while maintaining an indentation depth of 30%. a) stress vs. strain of alginate containing single-cell. b) Stress vs. strain of Core-shell alginate microgel. In both cases, for the same strain rate, a higher stress would be obtained as the approached velocity increases (lower relaxation time).

The stiffness of materials is defined as their resistance to deformation during an applied force. It is represented by the slop of force-displacement (or stress-strain) plot in the linear region contributed to elastic region or by Hertz contact mechanics theory in the power-law region of

force-displacement/stress-strain curve. Herein, using the Hertz theory, Young's modulus of each particle with indentation velocity of 0.5 mm/s at their 30% strain was calculated (Table 5.5).

The results indicate that single-cell alone has a very low stiffness of 9.774e-05MPa within 30% strain. However, The encapsulation of single-cell in microgel causes the overall stiffness of this particle to be more than single-cell for the same indentation depth (Figure5.9 and Table 5.5).

This result is in good agreement with studies on the effect of cell encapsulation (in different hydrogels) on the mechanical properties [115, 116]. Both Young's modulus and the stiffness of hydrogels would remain almost the same. Furthermore, the obtained stiffness in comparable to reported modulus for cells, 0.1 to 12 kPa [117].

It is essential to point out that at the maximum deformation of 22% and 24% of alginate microgel containing single-cell, the cell would undergo 30% and 40% of deformation, respectively. Hence, the stress- strain curves of alginate containing single-cell at the strains of 22% and 24% were plotted.

The stress-strain curve of all particles at an indentation depth of 40% is shown in Figure Appendix B.3.

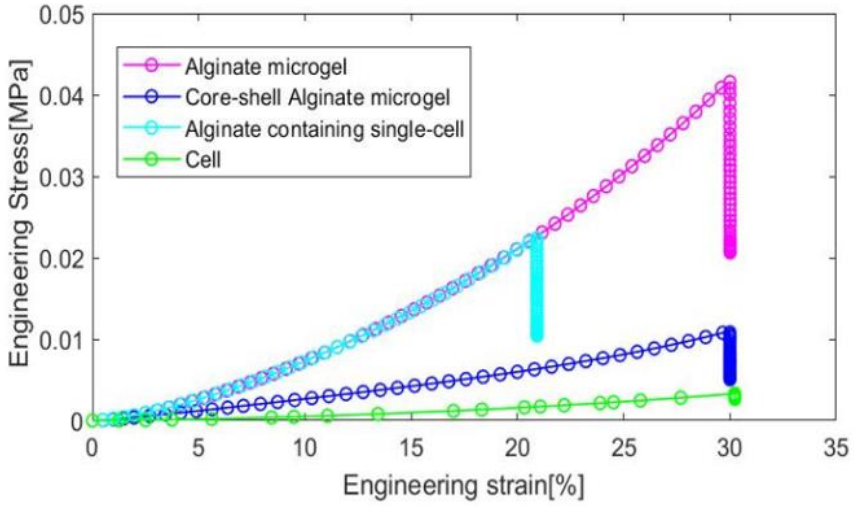

Figure 5.9 Stress-strain curves at constant indentation velocity of 0.5 mm/s, for the indentation depth of 30%. The slope of the curves in their linear region (up to) would represent Young's modulus or the stiffness of each particle. Alginate microgel containing single-cell and alginate microgel has almost similar stiffness, but it is slightly higher for alginate microgel containing single-cell.

Table 5.5 Young's modulus of each particle at 30% strain while maintaining indentation velocity of 0.5 mm/s

Particles	Young's modulus (MPa), 30% strain
Alginate microgel	3.124e-03
Core-shell alginate microgel	7.877e-04
Alginate containing single-cell	2.718e-03
Single-cell	9.774e-05

Even though using core-shell microgels means having less stiffness and a higher risk of rapturing, Wang et al. [53] depicted the protective effect of core-shell structures from shear forces during a suspension culture compared to solid-like microgels. Additionally, encapsulation of a single-cell with cell media containing genome vectors in the core of a core-shell GelMA microgel can increase the possibility of introducing the genome vectors in the encapsulated cell upon squeezing. As the results depicted, solid-like microgels cause a high reactive-force during indentation on the particles, which would decrease cell viability. On the contrary, core-shell microgels generate less reactive-force, which would enhance cell viability.

Successful transfection of single cells in core-shell microgels would cause the formation of a colony of transfected cells as microgels provide a 3D cell culturing environment.

5.3.2 Computational Fluid Dynamics

Following the CFD protocol presented in Sub-Section 5.2.2, the velocity and pressure profiles for two different designs were obtained. Based on the indentation simulation results, it was found that for 30% deformation of a single-cell encapsulated in alginate microgel, the alginate containing cell should be deformed to 21% of its size (102 um). Considering this fact, the two designs have the same confinement diameter of 0.08 um. However, the confinement length of the first design is 202 um that is two times greater than the one in the second design. According to Figure 5.10, the highest velocity magnitude happens in the middle of constriction channels

regardless of the designs, but this value is slightly more for the first design with a larger confinement length than the second design.

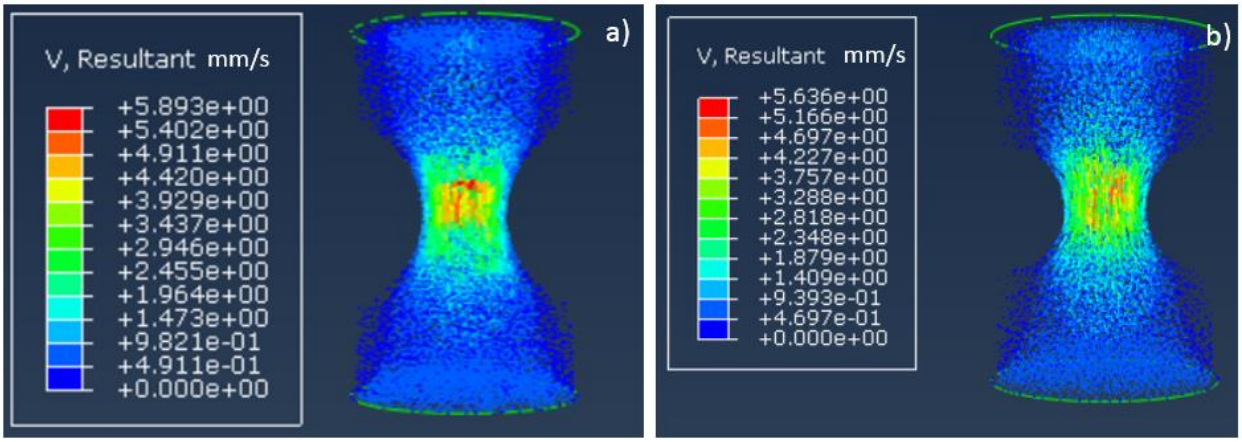

Figure 5.10 Velocity contours (mm/s) of constriction channels for 21% of deformation. a) The velocity contour of the first design with the confinement length of 202 um. b) The velocity contour of the second design with confinement length of 0.101 um. The highest velocity magnitude is slightly greater for the first design than the second design.

The comparison between the pressure contours of two designs declares that the pressure increases as a greater theta angle (shown in Figure 5.11) is selected for the structure. In other words, a larger confinement length causes more pressure, while the confinement diameter is fixed.

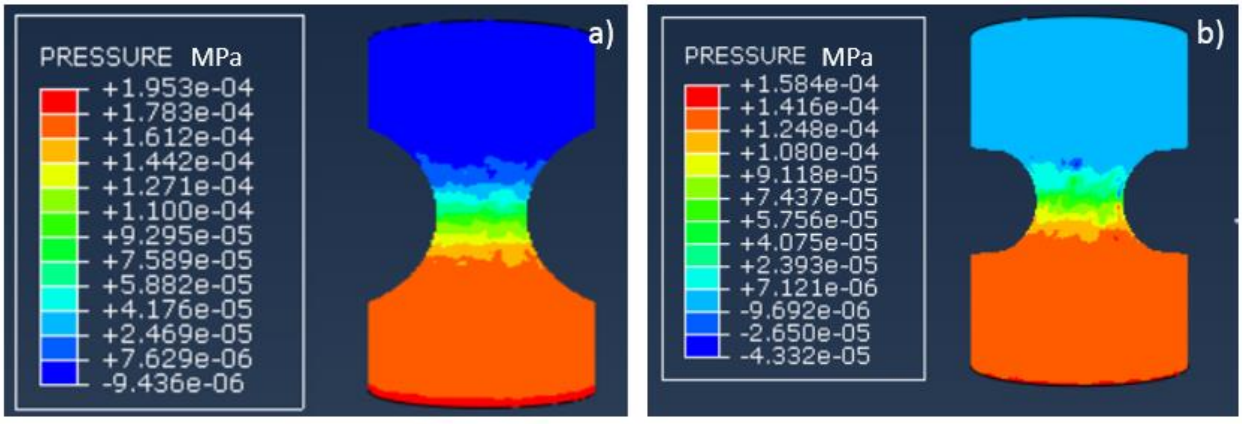

Figure 5.11 The pressure contour (MPa) of confinement channels. a) The pressure contour of the first design with the confinement length of 202 um. b) The pressure contour of the second design with confinement length of 0.101 um. The highest pressure is approximately 2.6 times more for the first design than the second design.

According to the CFD results, a higher flow rate (velocity) has been obtained for a longer confinement channel. Furthermore, it was found that higher flow velocity would increase the transfection rate [118], larger confinement length is deemed in the design of our microfluidic-based confinement channel.

5.3.3 Grid Indecency Analysis of FEM Model

Mesh convergence was used to determine the optimum element size which assures the independence of the results from mesh size. Figure 5.12 shows the mesh convergence analysis results for alginate microgel and cell indentation simulation. The element size study for the two other simulations are shown in Appendix C.1. Mises stress of the top particle node was selected as the studied parameter and was plotted against time for each simulation. The optimum element size for each particle is found and reported in Table 5.6.

In all cases, the increment in the mesh element size causes a greater generated maximum force. First, the slope of the curves in the relaxation part was sharper in regions with the lowest number of elements (smallest element size), and it smoothened as this value grows in number.

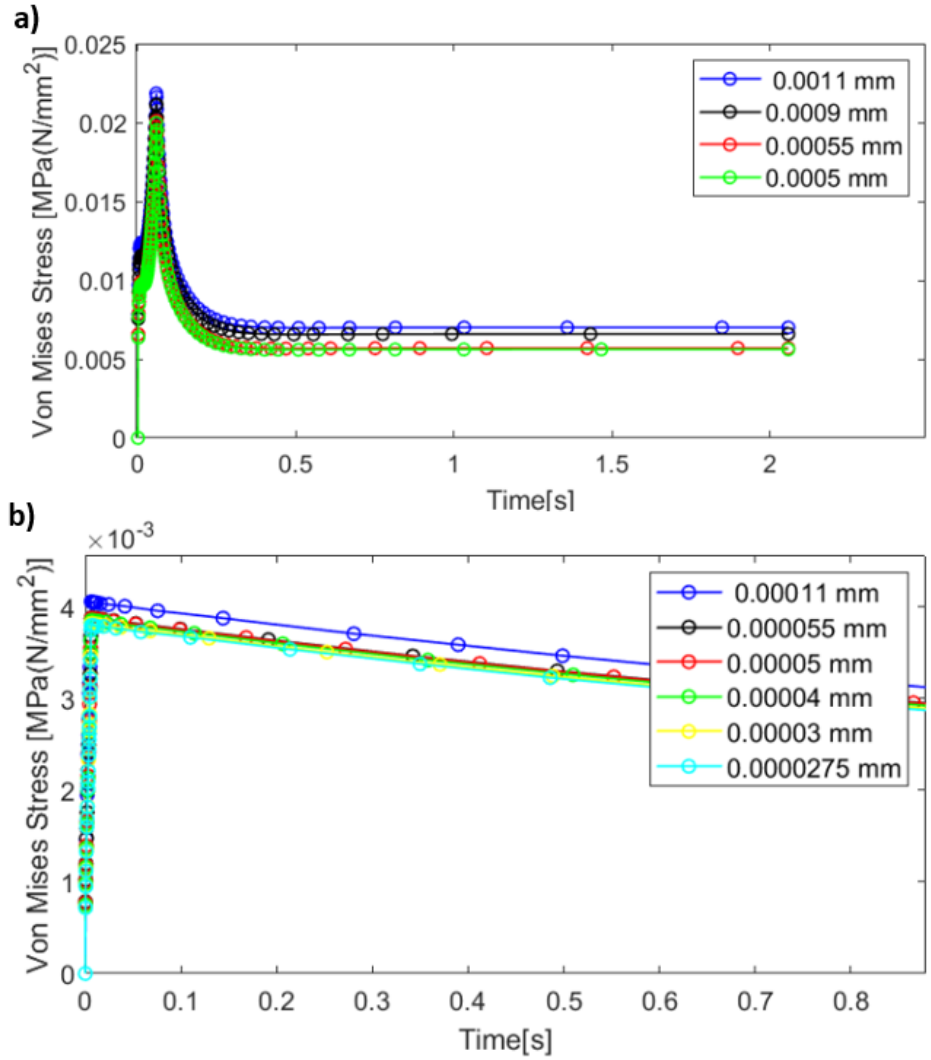

Figure 5.12 Convergence behavior of indentation simulation based on von Mises stress-time plot. a)Von Mises stress-time of alginate microgel. The result would have less than 0.5% difference when the element size was selected less than 0.00055 mm b) Von Mises stress-time of single-cell indentation. The result would converge with an error of less than 0.5% when the element size was selected below 0.00003 mm. All Element sizes are in mm.

Table 5.6 Optimum element size for particles indentation

Particle	Optimum element size (mm)
Alginate microgel	0.0005
Core-shell microgel	0.0004
Microgel containing single-cell	Cell:0.00035 Microgel: 0.00035
Single-cell	0.00003

5.3.4 Model Validation

To validate and evaluate the presented computational model, the work reported by Nguyen et al. [110] was simulated. The force- indentation plot was obtained using current simulation, and then was compared with the reported one in the reference. The modeling procedure and parameters were explained in Section 5.2 and Table 5.2 The experimental data and data from FEM analysis of the reference were extracted using GetData Software.

The force-displacement curves are plotted in Figure 5.13. As it is noticeable, the force increases exponentially by displacement until it reaches its maximum at predefined indentation depth.
The result clearly describes the good alignment of the curve obtained from current simulation and the experimental data given in the literature (RMSE: 6.03).

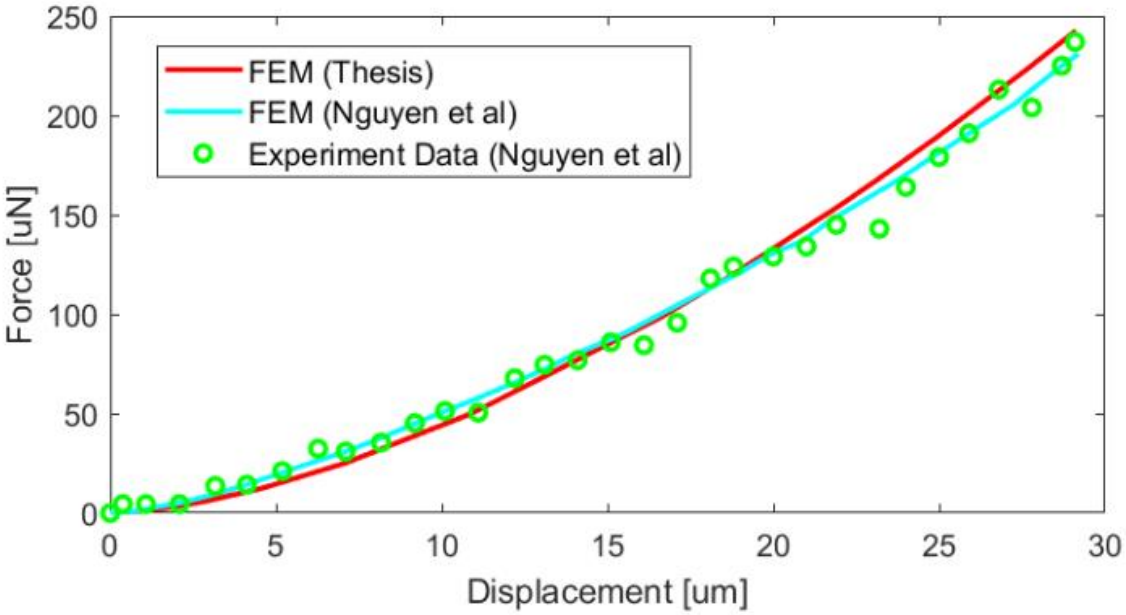

Figure 5.13 Comparison between force-indentation curve obtained from FEM of this thesis and the one extracted from Nguyen et al. [110].

Chapter 6 Conclusion and Future Work

Assessment and development of reliable and cost-effective systems for genome editing and cell transfection are increasingly gaining popularity in phenotype applications. In addition to transfection efficiency and cell functionality, another crucial step in cell transfection for phenotyping applications is the high-throughput of the system. There have been several methods, like viral vectors and electroporation and microinjection, but they are all restricted to their low-throughput and mitigation risk.

On the other hand, microfluidic-based deformation systems have shown significant performance in transfection of hundreds of million cells in a short time (fewer than 5 minutes), while preserving the functionality of cells. Although microfluidic-based deformation systems have shown good functionality in terms of high-throughput, there is still a vital requirement in the development of low-cost, and accurate devices by targeting the enhancement of cell viability and colony formation of transfected cells. Furthermore, limited information about the effect of key parameters, such as indentation velocity and depth, applied stress, and mechanical properties of cells, on cell transfection is currently available. The more information we attain about the dependency of cell transfection and viability on cell mechanical properties and the design parameters of microfluidic channels, the more efficient the fabricated microfluidic device will turn to be.

This research has focused on a cost-effective design and fabrication of a droplet-based microfluidic device to generate GelMA core-shell and solid-like microgels for future goal of cell encapsulation and to on-chip colony formation of transfected cells. To achieve this, first GelMA microgels, solid-like and core-shell, were fabricated using a droplet microfluidic system. Then, a computational study using ABAQUS software was performed on the indentation of different particles. Their mechanical properties and reliance on key parameters of indentation velocity and depth were extracted. Alginate was used in computation due to its similar properties and application with GelMA [43, 119], and its viscoelastic parameters, which was previously reported in other studies. Furthermore, the velocity contour of two microfluidic confinement channels with different confinement lengths were simulated using the CFD module of ABAQUS software.

Important results of this thesis are summarized as follows:

Three different techniques of photolithography, stereolithography, an cutter plotter were proposed and conducted for a droplet-based microfluidic device. The preference of using the cutter plotting technique in the fabrication of 3D microfluidic channels rather than the other techniques was pointed out. i.e. the fabrication of microchannels with variable thicknesses of 80 microns to 300 um, comparable to photolithography but cheaper and less complex. Moreover, the turbidity drawback of stereolithography technique was shown using SEM.

Using the above fabricated microfluidic chip, solid-like and core-shell GelMA microgels were fabricated. The adjustment of flow rate has an impact on the size of the generated microgels, i.e. Higher GelMA flow rate, greater size of microgels. The size distribution of the generated particles was plotted from the measurement of particles' diameter using an inverted microscope. The average diameter of 133.43±5 um was extracted from this curve. The spherical morphology and porosity of GelMA microgels were corroborated by SEM images.

Additionally, the mechanical properties of alginate microgel solid-like and core-shell, alginate contained single-cell, and single-cell were computationally extracted and their dependency on the indentation velocity and depth was also investigated. The results showed the maximum reaction force for alginate, alginate containing single-cell, core-shell, and single-cell, sorting from highest to lowest. This trend was observed in both strain rates (30% and 40%) regardless of the indentation speed. For all particles, the higher maximum force was observed for the higher strain rate and indentation speed. From stress-strain curves, the stiffness of particles was found. The stiffness of the alginate microgel containing cell almost remained the same as the alginate microgel. But, It was slightly higher for alginate containing single-cell. The lowest stiffness was for single-cell (9.774e-05 MPa) at the strain rate of 30%, while maintaining an indentation velocity of 0.5 mm/s. The stiffnesses of core-shell and alginate were also extracted as 7.877e-04 MPa, and 3.124e-03 MPa, respectively. The results show a lower stiffness for core-shell compared to the solid-like alginate microgel.

CFD results indicated higher flow rates for the microchannel with a larger confinement length. This result was used in the fabrication of our microfluidic-based confinement channel.

The results from the conducted computational study showed that regarding core-shell microgel lower penetration depth/larger constriction diameter should be selected. Besides, it helps us to have better insight into the mechanical properties of our specimens.

Summing up, core-shell GelMA microgel was the interest of this thesis for encapsulation of single cells, and finally, cell transfection due to its structure and higher cell viability. Owing to the core-shell structure, single-cell and cell media containing genome vectors can be encapsulated in the core, and then by applying a known deformation, these vectors can be delivered into single cells.

Possible opportunities for future researches are summarized as follows:

1. Experimental investigation of the dependency of indentation depth and reaction force on factors, such as cell viability and transfection rate might enable superior control over the efficient design of microfluidic-based deformation devices for cell transfection and intracellular delivery. Furthermore, a study on the effect of induced mechanical force on cellular viability and metabolic activities is essential as some concerns towards the destructive effects of the applied mechanical force on cells are raised.

2. A study towards the alteration of viability and proliferation of encapsulated cells (in GelMA microgels) by a shear flow can be another work which to the best of our knowledge has not been done yet.

3. A combination of microgels and encapsulated single cells in a cell transfection-based confinement channel needs a set of experiments in selecting the confinement depth based on the selected type of cells type. Owing to varied mechanical properties and size of cells, microfluidic-based confinement channels should be designed differently considering these variations. Using single cells in confinement channels, researchers have been able to report values of confinement depth for some cancer cells. However, changing the system to microgels and encapsulated cell, new experiments of calibration with the cells type are required.

4. This system lacked in-time monitoring devices, such as pressure or optical detectors , that allows the simultaneous location tracking of the particles. Tracking the particles in channels combining with simultaneous pressure measurement, can provide a location profile of each particle during the

confinement. This also can be used in real-time monitoring of particle pressure in different deformation stage while passing through the confinement channel.

5. Doing a nanoindentation test for GelMA microgels and change the simulation for GelMA material. As previously mentioned, GelMA was not used in our simulation as the viscoelastic properties of GelMA microgels have not been reported yet, therefore another hydrogel (alginate) was chosen. Characterization of GelMA microgels is a key parameter in cell-laden microfluidic microgels in tissue regeneration that aims to utilize the microgels as building blocks in tissue formation [120].

Appendix A: Nomenclature

Acronyms

PSD	Particle Size Distribution
CV	Coefficient of Variation
SEM	Scanning Electron Microscope
FT-IR	Fourier-Transform Infrared Spectroscopy
UV	Ultra Violet
CFD	Computational Fluid Dynamics
PVC	Polyvinyl Chloride
PSA	Pressure Sensitive Adhesive
PI	Photoinitiator
CM	Compressive Modulus
YM	Young's Modulus

Nomenclature

E	Elastic Modulus
G_0	instantaneous shear modulus
g_i	relaxation modulus
I_1	The first strain invariant
J^{el}	Determinant of deformation gradient
U	strain energy density function
D	Diffusion Coefficient
D	Particle Diameter
t	Time
ε	Strain
σ	Stress
η	Viscoelastic modulus
μ	Average diameter of the sample (Section 4.2), kinematic viscosity(Section 5.2)

κ	Bulk Modulus
υ	Poisson Ratio
σ	Standard deviation (Section 4.2)
τ	Relaxation time
R	Radius
h	Indentation depth
v	Fluid velocity vector
g	Gravitational constant
P	Fluid pressure
ρ	Fluid density

Appendix B: Simulation Results: Force vs. Time, Stress vs. Strain Plots

Reaction force-time curves of particles alginate microgel, core-shell alginate microgel, alginate microgel containing single-cell, single-cell were plotted at strain rate of 30% and 40% with constant approached velocity of 0.05 mm/s.

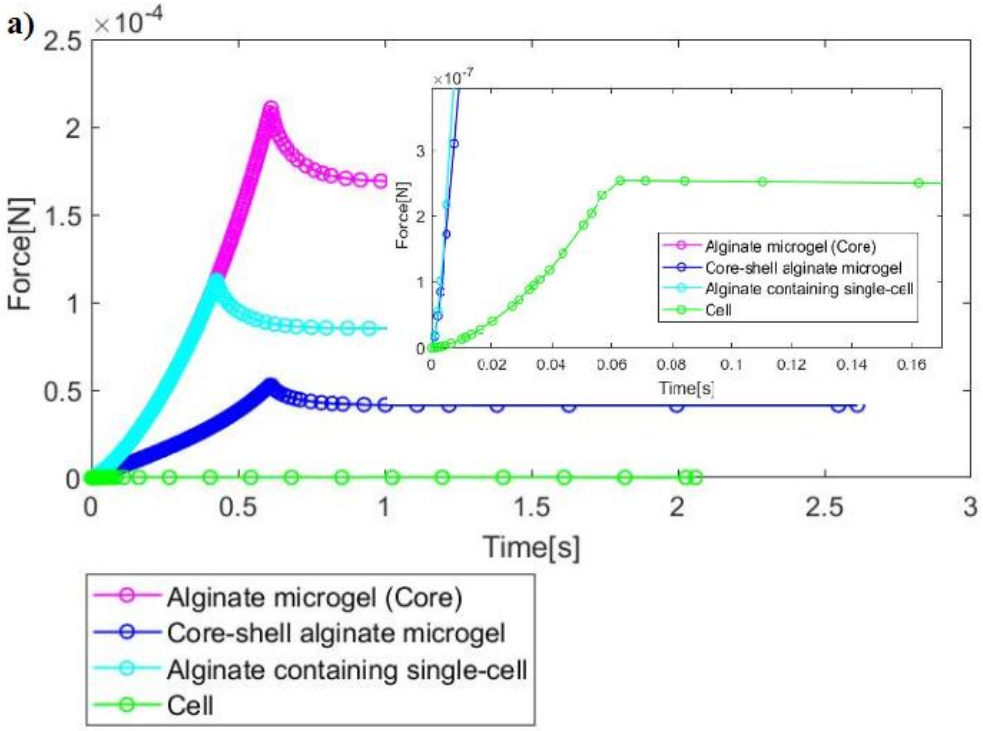

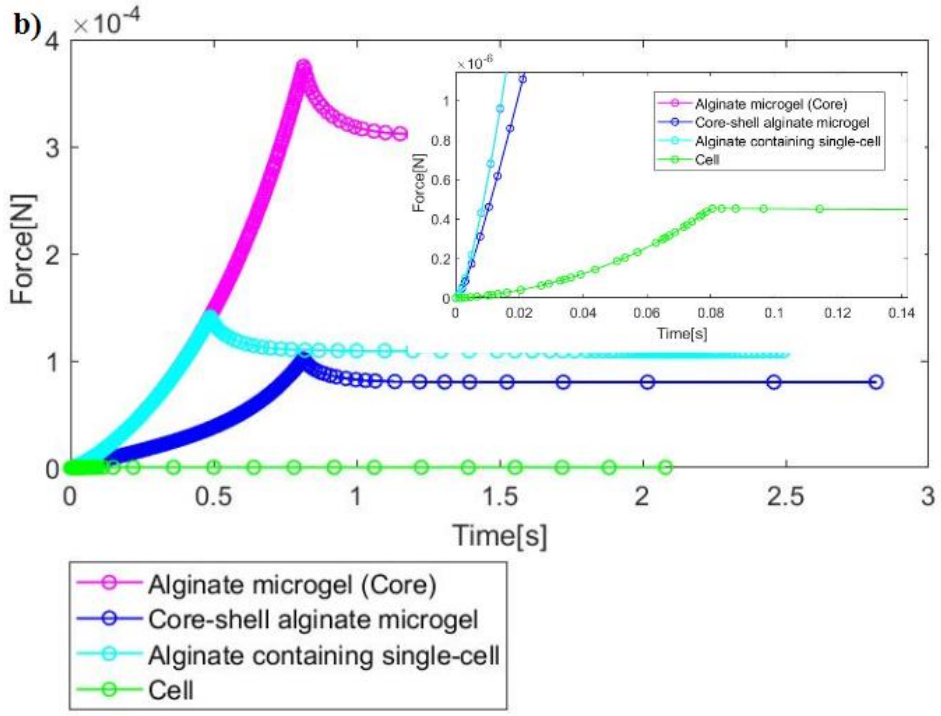

Figure Appendix B.1: Force-relaxation curves generated from FEM deeming the indentation velocity equal to 0.05 mm/s. a) At 30% strain. A maximum reaction force of approximately 2.2e-4 N was obtained for alginate and a minimum of 2.5e-7 N for single-cell. b) At 40% strain. A maximum reaction force of approximately 3.8e-4 N was obtained for alginate and a minimum of 0.5e-6 N for single-cell.

Stress-strain curves of alginate microgel and single-cell is shown in figure below. For the fix strain rate, as we increase the indentation velocity the stress generated on the particle would be increased. This is difference is so negligible in single-cell stress-strain curve.

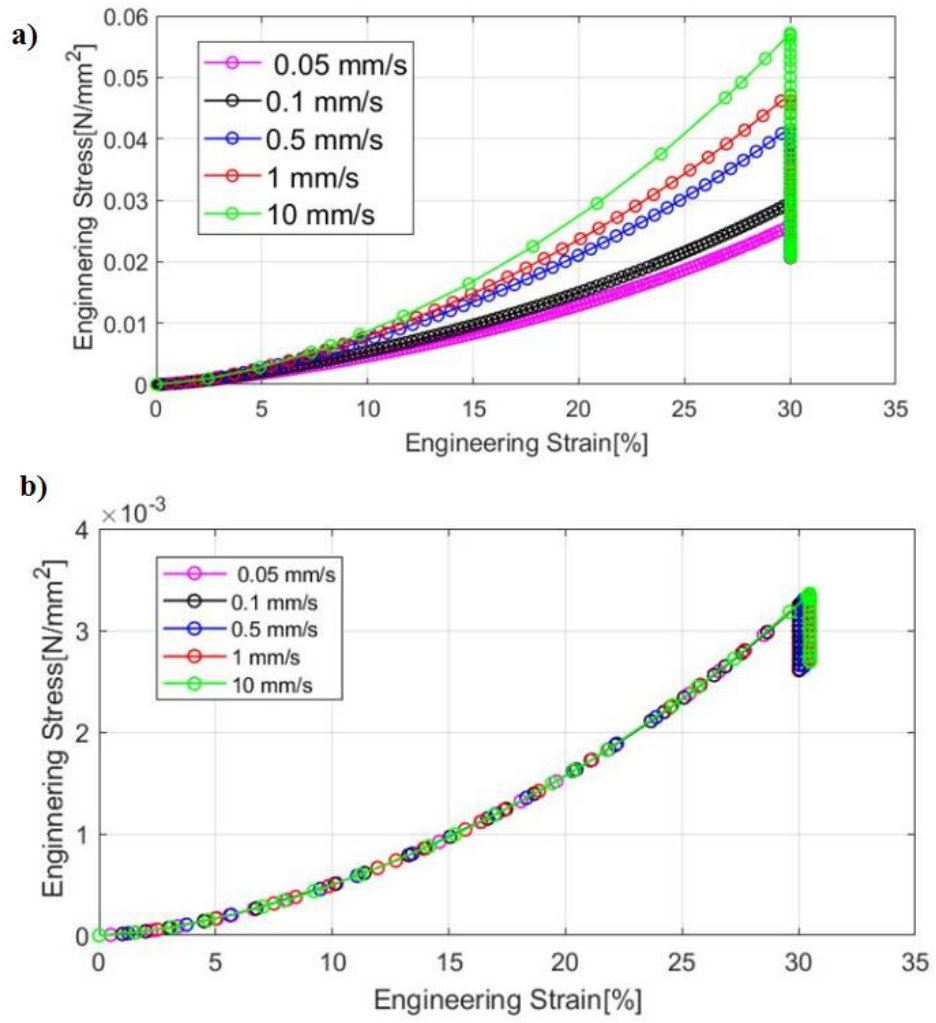

Figure Appendix B.2 Stress -strain curve at different indentation velocities for indentation depth of 30% strain. a) Stress vs. strain curve of alginate microgel. As it is conspicuous, the reaction stress increased with indentation speed from 0.5 to 10 mm/s under the same indentation depth. This is equally means, a higher indentation force is required to deform the samples for the same penetration depth. b) Stress-strain curve of single-cell. There is a negligible difference between stress-strain curve of cell at different velocities. It can be due to the small stiffness of cell.

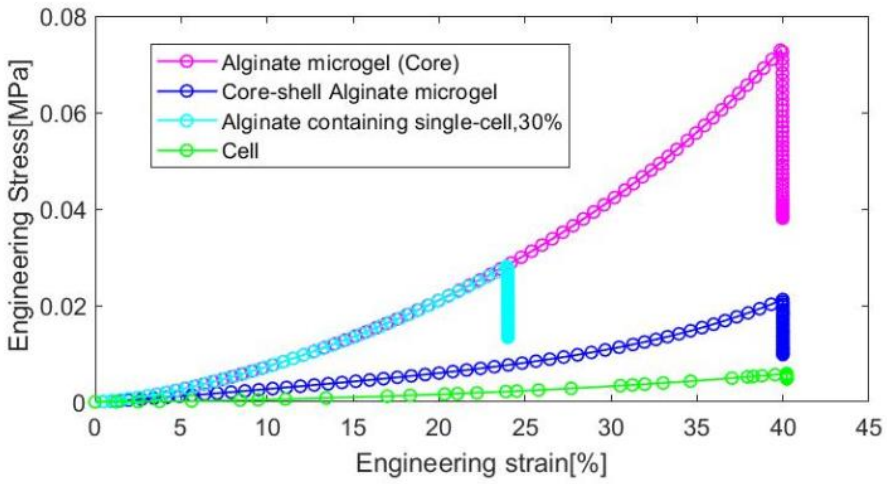

Figure Appendix.3: Stress-strain curves at constant indentation velocity of 0.5 mm/s , for the indentation depth of 40%. The slope of the curves in their linear region, would represent the Young's Modulus or the stiffness of each particle. Alginate microgel containing single-cell and alginate microgel has almost similar stiffness.

Appendix C: Mesh Convergence

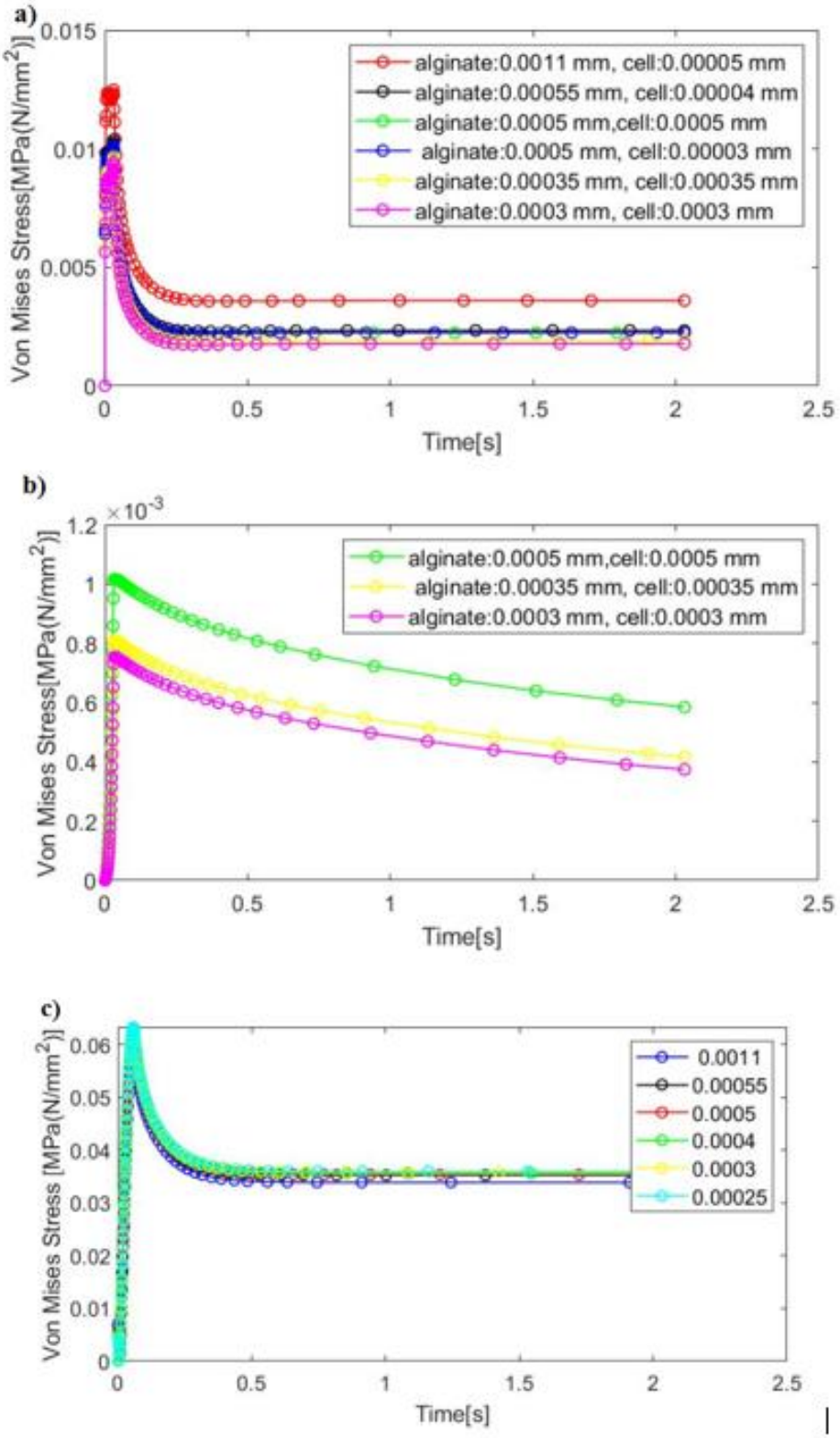

Figure Appendix C.1: Von Mises stress-time as a comparison parameter for mesh convergence validation. a) and b) are element size analysis of alginate microgel containing single-cell. Two element size analysis were conducted here, one for alginate particle and one for the encapsulated cell which are shown in a) and b) respectively. All the element sizes are in mm.

Appendix D: SEM

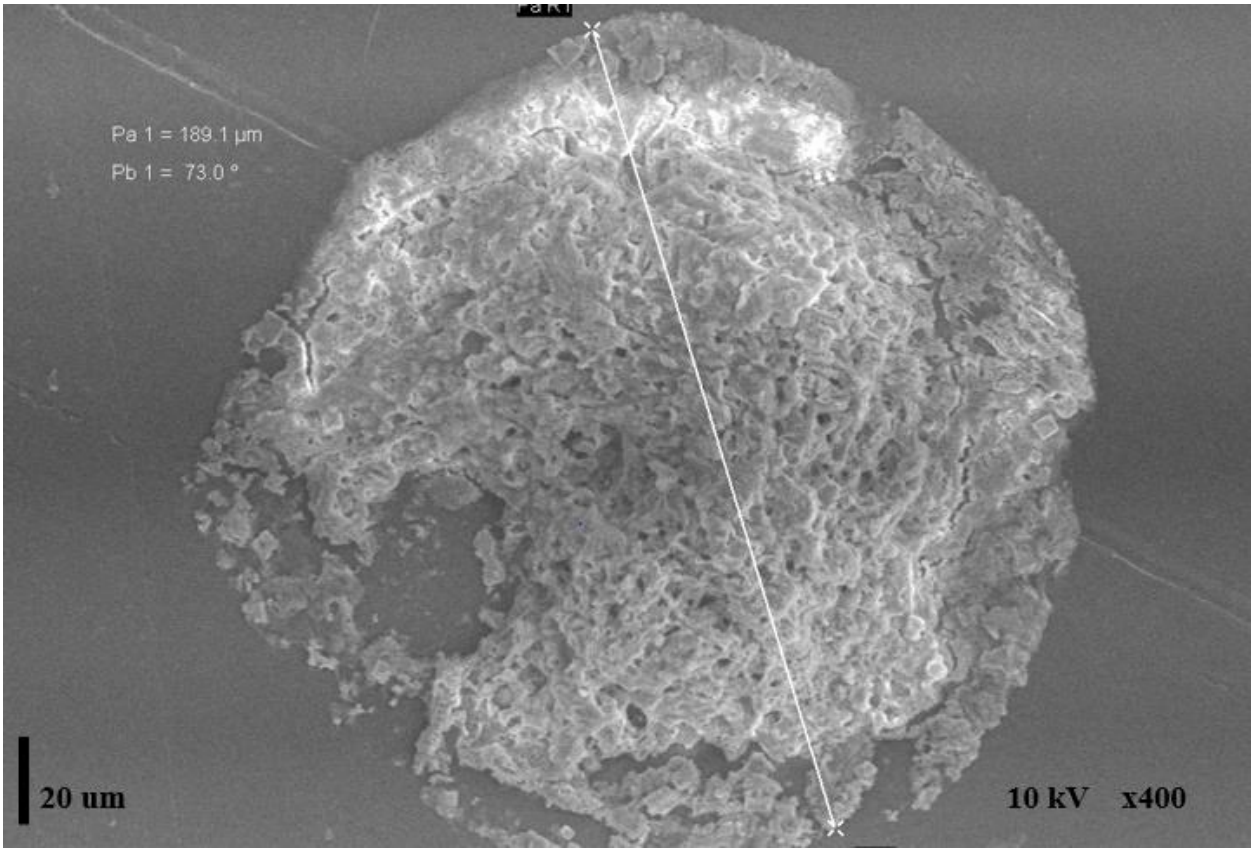

Figure Appendix D.1 Morphological characterization of GelMA microgel using SEM. The GelMA microgel was generated at the GelMA flow rate of 0.01 mL/hr with a constant oil flow rate of 2 mL/hr.

Bibliography

1. Thakore, P.I. and C.A. Gersbach, *Genome engineering for therapeutic applications*, in *Translating Gene Therapy to the Clinic*. 2015, Elsevier. p. 27-43.
2. Kim, T.K. and J.H. Eberwine, *Mammalian cell transfection: the present and the future.* Analytical and bioanalytical chemistry, 2010. **397**(8): p. 3173-3178.
3. Hernandez‐Garcia, A., et al., *Peptide–siRNA Supramolecular Particles for Neural Cell Transfection.* Advanced Science, 2019. **6**(3): p. 1801458.
4. Nguyen, D.N., et al., *Polymer-stabilized Cas9 nanoparticles and modified repair templates increase genome editing efficiency.* Nature biotechnology, 2020. **38**(1): p. 44-49.
5. Zhang, Y., et al., *Enhanced CRISPR-Cas9 correction of Duchenne muscular dystrophy in mice by a self-complementary AAV delivery system.* Science advances, 2020. **6**(8): p. eaay6812.
6. van Haasteren, J., et al., *The delivery challenge: fulfilling the promise of therapeutic genome editing.* Nature biotechnology, 2020: p. 1-11.
7. Vannucci, L., et al., *Viral vectors: a look back and ahead on gene transfer technology.* New Microbiol, 2013. **36**(1): p. 1-22.
8. Zaidi, S.S.-e.-A. and S. Mansoor, *Viral vectors for plant genome engineering.* Frontiers in plant science, 2017. **8**: p. 539.
9. Xu, X., et al., *Efficient homology-directed gene editing by CRISPR/Cas9 in human stem and primary cells using tube electroporation.* Scientific reports, 2018. **8**(1): p. 1-11.
10. Tan, M., et al., *Microinjection induces changes in the transcriptome of bovine oocytes.* Scientific Reports, 2020. **10**(1): p. 1-9.
11. Kelley, M.L., et al., *Versatility of chemically synthesized guide RNAs for CRISPR-Cas9 genome editing.* Journal of biotechnology, 2016. **233**: p. 74-83.
12. Kim, J., et al., *Microfluidic approaches for gene delivery and gene therapy.* Lab on a Chip, 2011. **11**(23): p. 3941-3948.
13. Jarrell, J.A., et al., *Intracellular delivery of mRNA to human primary T cells with microfluidic vortex shedding.* Scientific reports, 2019. **9**(1): p. 1-11.
14. Puigmartí-Luis, J., *Microfluidic platforms: a mainstream technology for the preparation of crystals.* Chemical Society Reviews, 2014. **43**(7): p. 2253-2271.
15. Sohrabi, S. and M.K. Moraveji, *Droplet microfluidics: fundamentals and its advanced applications.* RSC Advances, 2020. **10**(46): p. 27560-27574.
16. Frommhold, P.E., et al., *High-speed monodisperse droplet generation by ultrasonically controlled micro-jet breakup.* Experiments in fluids, 2014. **55**(4): p. 1716.
17. Li, S., et al., *Size-adjustable microdroplets generation based on microinjection.* Micromachines, 2017. **8**(3): p. 88.
18. Zhang, H., et al., *An ultra high-efficiency droplet microfluidics platform using automatically synchronized droplet pairing and merging.* Lab on a Chip, 2020. **20**(21): p. 3948-3959.
19. Shao, F., et al., *Microfluidic encapsulation of single cells by alginate microgels using a trigger-gellified strategy.* Frontiers in Bioengineering and Biotechnology, 2020. **8**.
20. Sesen, M. and G. Whyte, *image-Based Single cell Sorting Automation in Droplet Microfluidics.* Scientific Reports, 2020. **10**(1): p. 1-14.
21. Kung, C.-T., et al., *Microfluidic synthesis control technology and its application in drug delivery, bioimaging, biosensing, environmental analysis and cell analysis.* Chemical Engineering Journal, 2020: p. 125748.

22. Salehi, S.S., A. Shamloo, and S.K. Hannani, *Microfluidic technologies to engineer mesenchymal stem cell aggregates—applications and benefits.* Biophysical Reviews, 2020: p. 1-11.
23. Jankowski, P., et al., *A microfluidic platform for screening and optimization of organic reactions in droplets.* Journal of Flow Chemistry, 2020. **10**(2): p. 397-408.
24. James, M., et al., *Microfluidic Synthesis of Iron Oxide Nanoparticles.* Nanomaterials, 2020. **10**(11): p. 2113.
25. Ding, X., et al., *High-throughput nuclear delivery and rapid expression of DNA via mechanical and electrical cell-membrane disruption.* Nature biomedical engineering, 2017. **1**(3): p. 1-7.
26. Han, X., et al., *CRISPR-Cas9 delivery to hard-to-transfect cells via membrane deformation.* Science advances, 2015. **1**(7): p. e1500454.
27. Hosokawa, M., et al., *Massively parallel whole genome amplification for single-cell sequencing using droplet microfluidics.* Scientific reports, 2017. **7**(1): p. 1-11.
28. Jansen, K., et al., *Hydrogel-based cell therapies for kidney regeneration: current trends in biofabrication and in vivo repair.* Current pharmaceutical design, 2017. **23**(26): p. 3845-3857.
29. Liu, A., et al., *Microfluidic generation of transient cell volume exchange for convectively driven intracellular delivery of large macromolecules.* Materials Today, 2018. **21**(7): p. 703-712.
30. Tsukamoto, Y., et al., *Expression of DDX27 contributes to colony-forming ability of gastric cancer cells and correlates with poor prognosis in gastric cancer.* American journal of cancer research, 2015. **5**(10): p. 2998.
31. Tabatabaei, F., K. Moharamzadeh, and L. Tayebi, *Fibroblast encapsulation in gelatin methacryloyl (GelMA) versus collagen hydrogel as substrates for oral mucosa tissue engineering.* Journal of Oral Biology and Craniofacial Research, 2020. **10**(4): p. 573-577.
32. Cabot, J.M., et al., *Electrofluidic control of bioactive molecule delivery into soft tissue models based on gelatin methacryloyl hydrogels using threads and surgical sutures.* Scientific Reports, 2020. **10**(1): p. 1-10.
33. Cui, J., et al., *Multicellular co-culture in three-dimensional gelatin methacryloyl hydrogels for liver tissue engineering.* Molecules, 2019. **24**(9): p. 1762.
34. Topkaya, S.N., *Gelatin methacrylate (GelMA) mediated electrochemical DNA biosensor for DNA hybridization.* Biosensors and Bioelectronics, 2015. **64**: p. 456-461.
35. Sun, M., et al., *Synthesis and properties of gelatin methacryloyl (GelMA) hydrogels and their recent applications in load-bearing tissue.* Polymers, 2018. **10**(11): p. 1290.
36. Nichol, J.W., et al., *Cell-laden microengineered gelatin methacrylate hydrogels.* Biomaterials, 2010. **31**(21): p. 5536-5544.
37. Bertassoni, L.E., et al., *Direct-write bioprinting of cell-laden methacrylated gelatin hydrogels.* Biofabrication, 2014. **6**(2): p. 024105.
38. Li, X., et al., *3D culture of chondrocytes in gelatin hydrogels with different stiffness.* Polymers, 2016. **8**(8): p. 269.
39. Yin, J., et al., *3D bioprinting of low-concentration cell-laden gelatin methacrylate (GelMA) bioinks with a two-step cross-linking strategy.* ACS applied materials & interfaces, 2018. **10**(8): p. 6849-6857.
40. Zhao, X., et al., *Injectable stem cell‐laden photocrosslinkable microspheres fabricated using microfluidics for rapid generation of osteogenic tissue constructs.* Advanced Functional Materials, 2016. **26**(17): p. 2809-2819.
41. Jiang, W., et al., *Cell-laden microfluidic microgels for tissue regeneration.* Lab on a Chip, 2016. **16**(23): p. 4482-4506.
42. Bilal, M., et al., *Agarose-chitosan hydrogel-immobilized horseradish peroxidase with sustainable bio-catalytic and dye degradation properties.* International journal of biological macromolecules, 2019. **124**: p. 742-749.

43. Ashimova, A.N., et al., *Cell Encapsulation Within Alginate Microcapsules: Immunological Challenges and Outlook.* Frontiers in Bioengineering and Biotechnology, 2019. **7**: p. 380.
44. Shi, Y., et al., *High throughput generation and trapping of individual agarose microgel using microfluidic approach.* Microfluidics and nanofluidics, 2013. **15**(4): p. 467-474.
45. Kamperman, T., et al., *Single-cell microgels: technology, challenges, and applications.* Trends in biotechnology, 2018. **36**(8): p. 850-865.
46. Mohamed, M.G., et al., *An integrated microfluidic flow-focusing platform for on-chip fabrication and filtration of cell-laden microgels.* Lab on a Chip, 2019. **19**(9): p. 1621-1632.
47. Mashaghi, S., et al., *Droplet microfluidics: A tool for biology, chemistry and nanotechnology.* TrAC Trends in Analytical Chemistry, 2016. **82**: p. 118-125.
48. Rajawat, A. and S. Tripathi, *Disease diagnostics using hydrodynamic flow focusing in microfluidic devices: Beyond flow cytometry.* Biomedical Engineering Letters, 2020: p. 1-17.
49. Yaghmur, A., et al., *A hydrodynamic flow focusing microfluidic device for the continuous production of hexosomes based on docosahexaenoic acid monoglyceride.* Physical Chemistry Chemical Physics, 2019. **21**(24): p. 13005-13013.
50. Shivhare, P., et al., *Hydrodynamic focusing and interdistance control of particle-laden flow for microflow cytometry.* Microfluidics and Nanofluidics, 2016. **20**(6): p. 1-14.
51. Kleiber, A., et al., *3-Step flow focusing enables multidirectional imaging of bioparticles for imaging flow cytometry.* Lab on a Chip, 2020. **20**(9): p. 1676-1686.
52. Guermani, E., et al., *Engineering complex tissue-like microgel arrays for evaluating stem cell differentiation.* Scientific reports, 2016. **6**(1): p. 1-8.
53. Wang, H., et al., *One‐Step Generation of Core–Shell Gelatin Methacrylate (GelMA) Microgels Using a Droplet Microfluidic System.* Advanced Materials Technologies, 2019. **4**(6): p. 1800632.
54. Liu, L., et al., *High throughput gene expression profiling of yeast colonies with microgel-culture Drop-seq.* Lab on a Chip, 2019. **19**(10): p. 1838-1849.
55. Bah, M.G., H.M. Bilal, and J. Wang, *Fabrication and application of complex microcapsules: a review.* Soft Matter, 2020. **16**(3): p. 570-590.
56. Lei, W., et al., *Transport mechanism of deformable micro-gel particle through micropores with mechanical properties characterized by AFM.* Scientific reports, 2019. **9**(1): p. 1-12.
57. Karimzadeh, A., et al., *Assessment of nano-indentation method in mechanical characterization of heterogeneous nanocomposite materials using experimental and computational approaches.* Scientific reports, 2019. **9**(1): p. 1-14.
58. Luo, S., et al., *Cross-scale characterization of the elasticity of shales: Statistical nanoindentation and data analytics.* Journal of the Mechanics and Physics of Solids, 2020: p. 103945.
59. Ozcelik, A., et al., *Acoustic tweezers for the life sciences.* Nature methods, 2018. **15**(12): p. 1021-1028.
60. Dols-Perez, A., et al., *Artificial Cell Membranes Interfaced with Optical Tweezers: A Versatile Microfluidics Platform for Nanomanipulation and Mechanical Characterization.* ACS applied materials & interfaces, 2019. **11**(37): p. 33620-33627.
61. Ali, R., et al., *Enantioselective manipulation of single chiral nanoparticles using optical tweezers.* Nanoscale, 2020. **12**(8): p. 5031-5037.
62. de Aguiar, I.B., et al., *Microfluidic model systems used to emulate processes occurring during soft particle filtration.* Scientific reports, 2019. **9**(1): p. 1-9.
63. Davidson, P.M., et al., *High-throughput microfluidic micropipette aspiration device to probe time-scale dependent nuclear mechanics in intact cells.* Lab on a Chip, 2019. **19**(21): p. 3652-3663.
64. Daza, R., et al., *Comparison of cell mechanical measurements provided by atomic force microscopy (AFM) and micropipette aspiration (MPA).* Journal of the mechanical behavior of biomedical materials, 2019. **95**: p. 103-115.

65. Qian, L. and H. Zhao, *Nanoindentation of soft biological materials.* Micromachines, 2018. **9**(12): p. 654.
66. Bhushan, B., *Depth-sensing nanoindentation measurement techniques and applications.* Microsystem Technologies, 2017. **23**(5): p. 1595-1649.
67. Basoli, F., et al., *Biomechanical characterization at the cell scale: present and prospects.* Frontiers in physiology, 2018. **9**: p. 1449.
68. Gadelrab, K.R. and M. Chiesa, *Influence of nanoindenter tip radius on the estimation of the elastic modulus.* Deformation Mechanisms, Microstructure Evolution and Mechanical Properties of Nanoscale Materials, 2011: p. 53.
69. Ebenstein, D.M. and L.A. Pruitt, *Nanoindentation of biological materials.* Nano Today, 2006. **1**(3): p. 26-33.
70. Cha, C., et al., *Microfluidics-assisted fabrication of gelatin-silica core–shell microgels for injectable tissue constructs.* Biomacromolecules, 2014. **15**(1): p. 283-290.
71. Wang, L., et al., *Determination of viscohyperelastic properties of tubule epithelial cells by an approach combined with AFM nanoindentation and finite element analysis.* Micron, 2020. **129**: p. 102779.
72. Kamikawa, Y., K. Amezawa, and K. Terada, *Elastic–Plastic Deformation of a Solid Electrolyte Interface Formed by Reduction of Fluoroethylene Carbonate: A Nanoindentation and Finite Element Analysis Study.* The Journal of Physical Chemistry C, 2020.
73. Carniel, T.A. and E.A. Fancello, *Modeling the local viscoelastic behavior of living cells under nanoindentation tests.* Latin American Journal of Solids and Structures, 2017. **14**(5): p. 844-860.
74. Qiu, J. and F.-F. Li, *Identification of Viscoelastic Constitutive Parameters of a Cell Based on Fluid-Structure Coupled Finite Element Model and Experiment.* Mathematical Problems in Engineering, 2019. **2019**.
75. Sacco, R., et al., *A poroelastic mixture model of mechanobiological processes in biomass growth: theory and application to tissue engineering.* Meccanica, 2017. **52**(14): p. 3273-3297.
76. Yuan, D., et al., *A poroelastic model of a fibrous-porous tissue engineering Scaffold.* Scientific reports, 2018. **8**(1): p. 1-10.
77. Wang, L. and X. Liu, *Finite element simulation for the effect of loading rate on visco-hyperelastic characterisation of soft materials by spherical nanoindentation.* IET nanobiotechnology, 2019. **13**(6): p. 578-583.
78. Castilho, M., et al., *Mechanical behavior of a soft hydrogel reinforced with three-dimensional printed microfibre scaffolds.* Scientific reports, 2018. **8**(1): p. 1-10.
79. Wang, X., et al., *Identification of mechanical parameters of urea-formaldehyde microcapsules using finite-element method.* Composites Part B: Engineering, 2019. **158**: p. 249-258.
80. Esteki, M.H., et al., *A new framework for characterization of poroelastic materials using indentation.* Acta biomaterialia, 2020. **102**: p. 138-148.
81. Wang, L., et al., *Finite Element Modelling of Single Cell Based on Atomic Force Microscope Indentation Method.* Computational and Mathematical Methods in Medicine, 2019. **2019**.
82. Wang, L., et al., *Effect of AFM Nanoindentation Loading Rate on the Characterization of Mechanical Properties of Vascular Endothelial Cell.* Micromachines, 2020. **11**(6): p. 562.
83. Florea, C., et al., *A combined experimental atomic force microscopy-based nanoindentation and computational modeling approach to unravel the key contributors to the time-dependent mechanical behavior of single cells.* Biomechanics and modeling in mechanobiology, 2017. **16**(1): p. 297-311.
84. Zhang, Z., J. Xu, and C. Drapaca, *Particle squeezing in narrow confinements.* Microfluidics and Nanofluidics, 2018. **22**(10): p. 120.

85. Adamo, A., et al., *Microfluidics-based assessment of cell deformability.* Analytical chemistry, 2012. **84**(15): p. 6438-6443.
86. Coulter, W.H. *High speed automatic blood cell counter and cell size analyzer*. in *Proceedings of the National Electronics Conference*. 1956.
87. Hur, J., et al., *Microfluidic Cell Stretching for Highly Effective Gene Delivery into Hard-to-Transfect Primary Cells.* ACS nano, 2020.
88. Modaresi, S., et al., *Intracellular Delivery of Exogenous Macromolecules into Human Mesenchymal Stem Cells by Double Deformation of the Plasma Membrane.* Advanced Therapeutics, 2020. **3**(1): p. 1900130.
89. Lino, C.A., et al., *Delivering CRISPR: a review of the challenges and approaches.* Drug delivery, 2018. **25**(1): p. 1234-1257.
90. Zhao, Y., et al., *A review of automated microinjection of zebrafish embryos.* Micromachines, 2019. **10**(1): p. 7.
91. Demirer, G.S. and M.P. Landry, *Delivering genes to plants.* Chemical Engineering Progress, 2017. **113**(4): p. 40-45.
92. Gao, X., K.-S. Kim, and D. Liu, *Nonviral gene delivery: what we know and what is next.* The AAPS journal, 2007. **9**(1): p. E92-E104.
93. Xu, S., T.P. Pham, and S. Neupane, *Delivery methods for CRISPR/Cas9 gene editing in crustaceans.* Marine Life Science & Technology, 2020. **2**(1): p. 1-5.
94. DiTommaso, T., et al., *Cell engineering with microfluidic squeezing preserves functionality of primary immune cells in vivo.* Proceedings of the National Academy of Sciences, 2018. **115**(46): p. E10907-E10914.
95. Takahashi, G., et al., *GONAD: Genome-editing via Oviductal Nucleic Acids Delivery system: a novel microinjection independent genome engineering method in mice.* Scientific reports, 2015. **5**: p. 11406.
96. Sharei, A., et al., *A vector-free microfluidic platform for intracellular delivery.* Proceedings of the National Academy of Sciences, 2013. **110**(6): p. 2082-2087.
97. Woodruff, K.P., *Microfluidic platforms for high-throughput mammalian cell printing, transfection, and dosage-dependent studies*. 2017, EPFL.
98. Cognart, H.A., J.-L. Viovy, and C. Villard, *fluid shear stress coupled with narrow constrictions induce cell type-dependent morphological and molecular changes in SK-BR-3 and MDA-MB-231 cells.* Scientific reports, 2020. **10**(1): p. 1-14.
99. Deng, Y., et al., *Intracellular delivery of nanomaterials via an inertial microfluidic cell hydroporator.* Nano letters, 2018. **18**(4): p. 2705-2710.
100. Lee, J., et al., *Nonendocytic delivery of functional engineered nanoparticles into the cytoplasm of live cells using a novel, high-throughput microfluidic device.* Nano letters, 2012. **12**(12): p. 6322-6327.
101. Liu, A., et al., *Cell Mechanical and Physiological Behavior in the Regime of Rapid Mechanical Compressions that Lead to Cell Volume Change.* Small, 2020. **16**(2): p. 1903857.
102. Zargari, S., S. Falaki, and H. Veladi. *Design and finite element analysis of a MEMS based capacitive pressure sensor using CNT/PDMS nanocomposite electrodes*. in *2016 24th Iranian Conference on Electrical Engineering (ICEE)*. 2016. IEEE.
103. Sánchez Rodríguez, V.H., *On the improvement of the process of synthesis of gelatin methacryloyl (GelMA) hydrogels and development of a hybrid nanoparticle-GelMA-based bioink for tissue engineering.* REPOSITORIO NACIONAL CONACYT.
104. Zhou, X., et al., *3D bioprinting a cell-laden bone matrix for breast cancer metastasis study.* ACS Applied Materials & Interfaces, 2016. **8**(44): p. 30017-30026.

105. Cijun, S., D. Ji an, and W. Jiong, *A method of establishing generalized Maxwell model for viscoelastic material.* ACTA MECHANICA SINICA-CHINESE EDITION-, 2006. **38**(4): p. 565.
106. Saprunov, I., M. Gergesova, and I. Emri, *Prediction of viscoelastic material functions from constant stress-or strain-rate experiments.* Mechanics of Time-Dependent Materials, 2014. **18**(2): p. 349-372.
107. Chen, X., et al., *An inverse method for determining the spatially resolved properties of viscoelastic–viscoplastic three-dimensional printed materials.* Proceedings of the Royal Society A: Mathematical, Physical and Engineering Sciences, 2015. **471**(2183): p. 20150477.
108. Zhao, W., et al., *A methodology to analyse and simulate mechanical characteristics of poly (2‐hydroxyethyl methacrylate) hydrogel.* Polymer international, 2013. **62**(7): p. 1059-1067.
109. Wang, L., J. Dong, and C.J. Xian, *Strain amplification analysis of an osteocyte under static and cyclic loading: a finite element study.* BioMed Research International, 2015. **2015**.
110. Nguyen, V., et al., *Mechanical properties of single alginate microspheres determined by microcompression and finite element modelling.* Chemical engineering science, 2009. **64**(5): p. 821-829.
111. Hashmi, S.M. and E.R. Dufresne, *Mechanical properties of individual microgel particles through the deswelling transition.* Soft Matter, 2009. **5**(19): p. 3682-3688.
112. Marko, M.D., et al., *Tribological investigations of the load, temperature, and time dependence of wear in sliding contact.* Plos one, 2017. **12**(4): p. e0175198.
113. George, H.F. and F. Qureshi, *Newton's Law of Viscosity, Newtonian and Non-Newtonian Fluids*, in *Encyclopedia of Tribology*, Q.J. Wang and Y.-W. Chung, Editors. 2013, Springer US: Boston, MA. p. 2416-2420.
114. Neumann, T., *Determining the elastic modulus of biological samples using atomic force microscopy.* JPK Instruments Application Report, 2008: p. 1-9.
115. Mao, A.S., et al., *Deterministic encapsulation of single cells in thin tunable microgels for niche modelling and therapeutic delivery.* Nature materials, 2017. **16**(2): p. 236-243.
116. Krishnamoorthy, S., B. Noorani, and C. Xu, *Effects of encapsulated cells on the physical–mechanical properties and microstructure of gelatin methacrylate hydrogels.* International Journal of Molecular Sciences, 2019. **20**(20): p. 5061.
117. Ding, Y., G.-K. Xu, and G.-F. Wang, *On the determination of elastic moduli of cells by AFM based indentation.* Scientific reports, 2017. **7**: p. 45575.
118. Zhao, D., et al., *A flow-through cell electroporation device for rapidly and efficiently transfecting massive amounts of cells in vitro and ex vivo.* Scientific reports, 2016. **6**(1): p. 1-9.
119. Zhang, X., et al., *Marine biomaterial-based bioinks for generating 3D printed tissue constructs.* Marine drugs, 2018. **16**(12): p. 484.
120. Newsom, J.P., K.A. Payne, and M.D. Krebs, *Microgels: Modular, tunable constructs for tissue regeneration.* Acta biomaterialia, 2019. **88**: p. 32-41.